MECCA

Journal of Middle European Construction and Design of Cars

Number 01 2018, volume XVI. 165 Kč / 11€

1 TURBOCHARGING OF HIGH PERFORMANCE COMPRESSED NATURAL GAS SI ENGINE FOR LIGHT DUTY VEHICLE
Marcel Škarohlíd, Jiří Vávra

10 IMPLICATION OF CYCLE-TO-CYCLE VARIABILITY IN SI ENGINES
Karel Páv

18 IDENTIFICATION OF CYCLE-TO-CYCLE VARIABILITY SOURCES IN SI ICE BASED ON CFD MODELING
Oldřich Vítek, Vít Doleček, Zbyněk Syrovátka, Jan Macek

33 PHYSICAL 1D MODEL OF A HIGH-PRESSURE RATIO CENTRIFUGAL COMPRESSOR FOR TURBOCHARGERS
Jan Macek

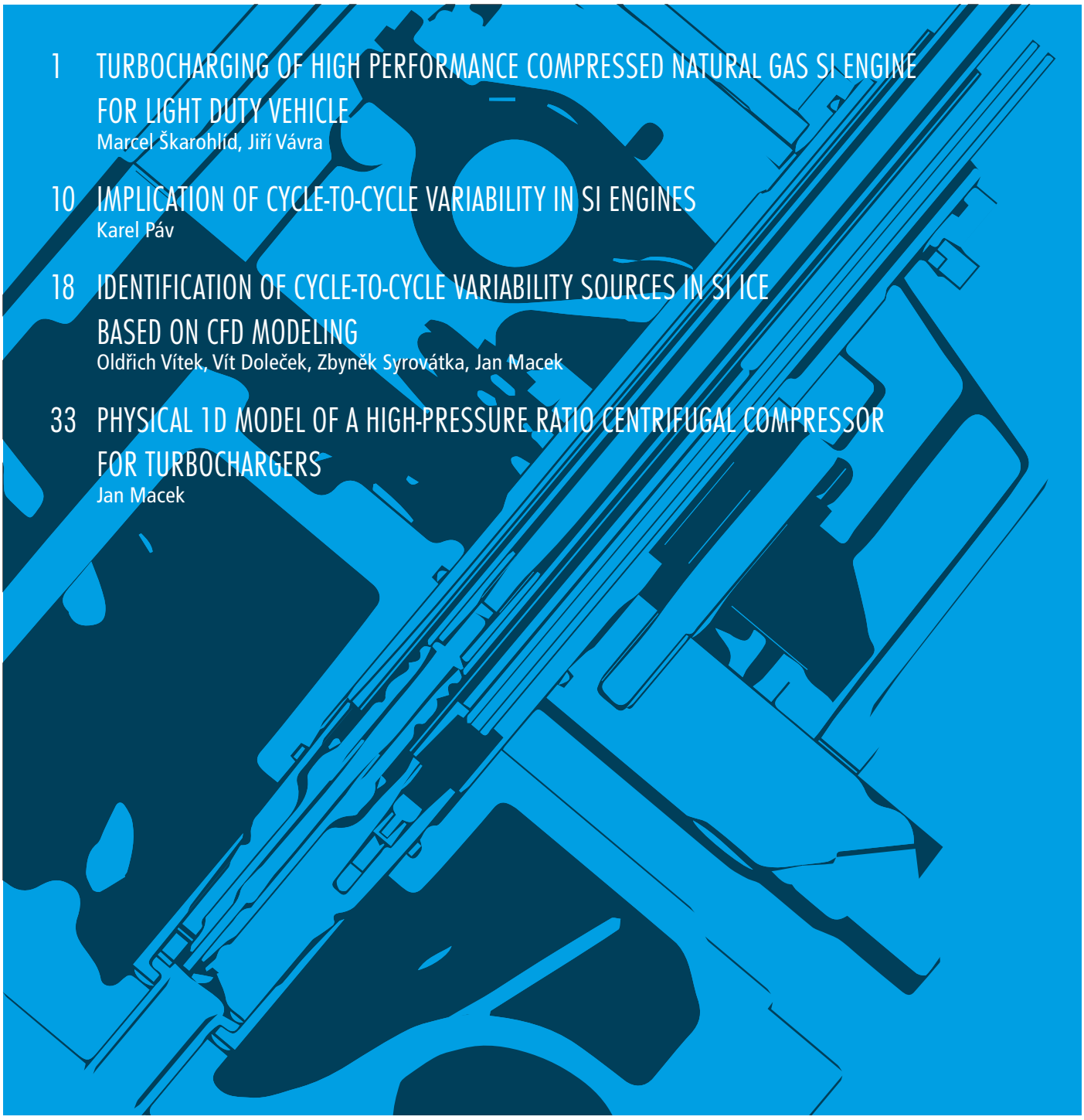

9 771214 082007

THIS ISSUE IS FOCUSED ON RESEARCH IN: INTERNAL COMBUSTION ENGINES

AIM

Published in the heart of Europe on Czech Technical University in Prague the journal reports about research in the field of internal combustion engines and all other components and aspects of vehicle engineering and vehicle design. The articles from the whole world are welcome.

THE FOLLOWING TOPICS ARE RELEVANT FOR THE JOURNAL MECCA:

- Engines and fuels
- Powertrains (hybrid vehicles, transmissions,...)
- Chassis
- Vehicle body
- Experimental testing
- Mechatronics
- Vehicle dynamics
- Safety
- Transport Systems
- Electronics in vehicles

PERIODICITY

Three times a year

REVIEW PROCESS

All articles are peer and blind reviewed. At least two reviewers per article.

LANGUAGE

English, bilingual abstract and legends (English/Czech or English/Slovak). Articles coming from non-English speaking coutries are submitted to English correction.

ABSTRACTING AND INDEXING

The journal is part of database of open access publications (DOAJ): https://doaj.org/toc/1804-9338
Publisher of the open access articles: De Gruyter.

This journal is published using financial support from the budget of the Centre of Vehicles for Sustainable Mobility, Faculty of Mechanical Engineering, Czech Technical University in Prague. A part of support comes from the project Josef Božek Competence Centre for Automotive Industry TE 0102 0020, funded by the Technological Agency of Czech Republic. These sources are gratefully acknowledged.

IMPRINT MECCA – VOLUME XVI, NUMBER 01, YEAR 2018, http://bozek.cvut.cz/mecca, gabriela.achtenova@fs.cvut.cz
Editor: České vysoké učení technické v Praze MECCA, Technická 4, 16607, Praha 6, Czech republic, **ISSN 1214-0821, ISSN 1804-9338 (Online), MK ČR E 13720**
Proofreading: Channel Crossings, Prague, Czech Republic **Advertising:** gabriela.achtenova@fs.cvut.cz or jan.macek@fs.cvut.cz **Production/Layout:** studio pixl-e (studio@pixle.cz)

DE GRUYTER OPEN

10.1515/mecdc-2018-0001

TURBOCHARGING OF HIGH PERFORMANCE COMPRESSED NATURAL GAS SI ENGINE FOR LIGHT DUTY VEHICLE

MARCEL ŠKAROHLÍD, JIŘÍ VÁVRA

Czech Technical University in Prague, Josef Božek Research Center, Technická 4, Prague 6, Czech Republic, 166 07

Email: marcel.skarohlid@fs.cvut.cz, jiri.vavra@fs.cvut.cz

ABSTRACT

Natural gas as an automotive fuel has many benefits in comparison with traditional fossil fuels. Favorable anti-knock properties of methane allow us to utilize higher boost levels and the engine power than that of gasoline engines. High level of intake boosting make possible to achieve loads, comparable to the state-of-the-art diesel of engines without soot and PM emission. Stoichiometric operation within the full range of the complete engine map enables the use of a relatively simple exhaust gas aftertreatment, based on a three-way catalyst.

The paper describes a chosen 1-D thermodynamic modelling studies, calibrated and validated by experimental data. The investigations were performed on a spark ignition, direct injection, four-cylinder engine with 1.6 L displacement. The engine was optimized for mono fuel operation with compressed natural gas.

Due to complexity of gaseous fuel infrastructure in vehicles, compared to the traditional fuels, it is desirable to keep the turbocharging system as simple as possible. Traditional variable geometry turbine systems were tested. Practical design constraints as peak cylinder pressure, turbine inlet temperature, compressor outlet temperature and others were met. Various strategies on how to achieve high load at low engine speed were investigated.

The authors propose a single stage turbocharger to cover the demand for a high torque at low engine speed and high power at full speed, with boost levels comparable to a dual stage turbocharging. It was concluded that the single stage turbocharging enables the engine to operate with maximum BME of 3 MPa between 1500 and 2750 rpm. Maximum engine speed had to be limited to a similar value that is usually applied in a diesel engine due to limited control range of turbocharging.

KEYWORDS: CNG ENGINE, MILLER CYCLE, VALVE TIMING, TURBOCHARGER

SHRNUTÍ

Zemní plyn jakožto automobilní palivo má mnoho výhod ve srovnání s tradičními fosilními palivy. Příznivé antidetonační vlastnosti metanu umožňují využít vyšší plnicí tlak a dosáhnout vyššího výkonu motoru než u benzínových motorů. Vysoká úroveň plnicího tlaku umožňuje dosáhnout zatížení, které je srovnatelné se vznětovými motory bez emisí sazí a pevných částic. Stechiometrická koncepce v celé pracovní oblasti motoru umožňuje použití relativně jednoduché následné úpravy výfukových plynů, založené na trojcestném katalyzátoru.

Článek popisuje vybrané studie termodynamického 1-D modelování, kalibrované a ověřené experimentálními daty. Výpočty byly provedeny na zážehovém čtyřválcovém motoru s přímým vstřikem paliva o objemu 1,6 l. Motor byl optimalizován pro provoz se stlačeným zemním plynem.

Vzhledem ke složitosti infrastruktury plynných paliv ve vozidle ve srovnání s tradičními palivy je žádoucí, aby systém přeplňování byl co nejjednodušší. Byly testovány tradiční turbíny s variabilní geometrií. Byly dodrženy praktická konstrukční omezení jako tlak ve válci, vstupní teplota výfukových plynů do turbíny, výstupní teplota stlačeného vzduchu z kompresoru a další. Byly zkoumány různé strategie, jak dosáhnout vysokého zatížení při nízkých otáčkách motoru.

Autoři navrhují jednostupňové turbodmychadlo, které pokryje poptávku po vysokém točivém momentu při nízkých otáčkách motoru a po vysokém výkonu ve vysokých otáčkách motoru, při úrovni plnicího tlaku srovnatelné s dvojstupňovým turbodmychadlem. Výsledkem je návrh jednostupňového turbodmychadla umožňujícího motoru pracovat s maximálním BMEP (středním efektivním tlakem) 3 MPa v rozsahu otáček 1500 a 2750 min^{-1}. Maximální otáčky motoru musely být sníženy na podobnou hodnotu jako u naftového motoru kvůli omezenému regulačnímu rozsahu turbodmychadla.

KLÍČOVÁ SLOVA: PLYNOVÝ CNG MOTOR, MILLERŮV CYKLUS, ČASOVÁNÍ VENTILŮ, TURBOKOMPRESOR

1. INTRODUCTION

Compressed natural gas as a fuel for spark ignition internal combustion engines, besides the advantages as a high resistance to knock, has favorable hydrogen to carbon ratio [1] and also the benefit of possibility to direct injection into the combustion chamber [2, 3, 4]. From the efficiency point of view, high resistance to knock allows the exploitation of high compression ratio and also the possibility to achieve high power density. For this, the DI concept, compared with conventional port fuel injection [5] significantly improves volumetric efficiency and reduces demands for turbocharging as an alternative to two stage turbocharging [6, 7]. Combination of the direct injection and a single stage turbocharger enables us to achieve high performance of gas SI engine. Previous studies show maximum achievable performance of the conventional ICE at the level of 3.5 MPa of brake mean effective pressure [8, 9, 10, 11], when uncompromising, unconstrained optimization of engine parameters (would be) implemented.

In comparison of natural gas direct injection to a Diesel direct injection and gasoline direct injection engines the particle matter emission issue can be eliminated. CO_2 emission index can be reduced by advantageous ratio of hydrogen to carbon in methane as a main component of natural gas. Full operational map stoichiometric engine operation enables to usage of a relatively simple aftertreatment system, based on a three-way catalyst.

Presented article describes selected studies from the thermodynamic modelling performed within the framework of subprojects WP04 and WP06 of Horizon 2020 EU project GasOn [12]. The subproject aims at the development of the VAN with the mono fuel SI turbocharged engine of cylinder displacement of 1.6 liter, with a direct injection of CNG and with a full map stoichiometric operation. Authors were responsible for the simulation support of the engine development. As a main tool a 1-D GT Suite [13] software was used. Target performance parameters are following:

Engine torque 180 Nm (BMEP 1.4 MPa) at 1000 rpm
Peak engine torque 380 Nm (BMEP 3 MPa) at 2000 rpm
Maximum power 125 kW (78 kW/l) at 5500 rpm.

The speed range for the maximum engine power was not a fixed value. According to the initial estimate the speed range of the peak power might lie within 3500 – 5500 rpm.

Large number of simulations have been carried out within the framework of this project. The main activity was the matching of the single stage turbocharger for fulfilling the demanded engine performance parameters, including the selection of the turbocharger control system using the variable turbine geometry (VTG) or the exhaust gas bypass of the turbine, so called waste gate (WG). In all investigated areas, the variable valve timing and two cam profile switching [14] were taken into account with optimization of combustion phasing and optimum rate of exhaust gas recirculation (EGR). The design of appropriate EGR loop was a part of this process. All of the simulations were performed with respect to the practical design and operational limits. The authors would like to point out several specific challenges and the approach on how to handle them.

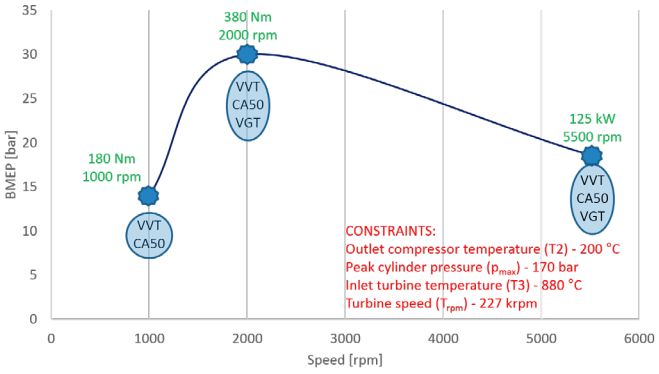

FIGURE 1: Main targets
OBRÁZEK 1: Hlavní cíle

2. ENGINE MODEL

For the task of turbocharger matching, valve lift and timing design an engine thermodynamic model was developed in a GT Power software. Model was created by merging of the two different models. Firstly, a model of a diesel four-cylinder engine with the similar geometry parameters (piston stroke, cylinder bore and intake and exhaust manifolds) and secondly, the model of a single cylinder engine with a direct injection of gaseous fuel into the cylinder [7], however with different cylinder bore.

Following features and components have been modified for natural gas engine performance simulations:

- Intake manifold was arranged to the final design of the GASON engine.
- Intercooler efficiency was adjusted by empirical equation provided by industrial partner.
- The valve lift profiles and a base valve timing was derived from the original Diesel engine model.
- Short duration cam profile, suggested for a full load at low engine RPM, was newly designed to fulfill the GASON project targets.
- Cylinder heat transfer was adjusted based on a sensitivity study and author's experience from the former R&D activity. Finally, unmodified Woschni correlation was used for a heat transfer coefficient determination.

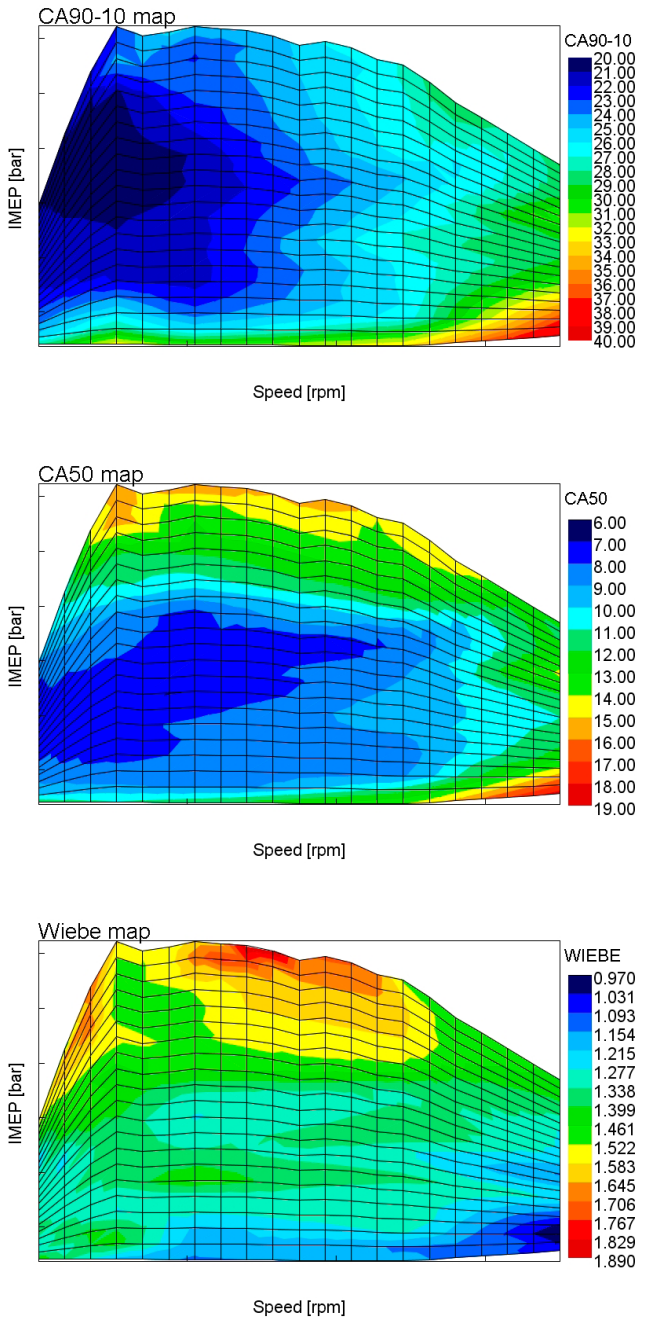

FIGURE 2: Maps of combustion parameters
OBRÁZEK 2: Mapy parametrů hoření

- Back pressure of a real exhaust gas aftertreatment system and muffler was emulated using a friction multiplier of individual components of the exhaust system.
- EGR cooler efficiency was adjusted based on empirical data obtained from the industrial partner.
- A simple GT Power direct natural gas injector model was designed according to measured injection mass in dependence of injection pulse width characteristic provided by industrial partner;
- Model of closed loop lambda=1 control was designed.
- Demanded power control strategy was prepared as a combination of
  – Closed loop turbocharger variable turbine geometry (VTG) control
  – Closed loop throttle valve control
- Variable valve timing (VVT) for minimum BSFC

Parameters of intake and exhaust ports were adopted from the model of the single cylinder engine and the data from the combustion models that were calibrated based on the results of a single cylinder engine combustion analysis [7, 15]. A GT Power EngCylCombSIWiebe model was selected for this task and the maps of the parameters, covering the full engine characteristics are displayed in Figure 2.
The top Figure shows a map of a combustion duration (CA90-10), the middle Figure shows a map of the combustion phasing expressed as an angle of a 50 percent burn mass (CA50) and at the bottom figure, a Wiebe exponent map is presented.
To ensure an appropriate fraction of EGR rate, the model was coupled with a low pressure cooled EGR system, including its control [16]. The model also comprises a switchable system for the control of the peak cylinder pressure by means of the variation of the spark advance control.
All the control systems were tuned in respect to the simulation stability. All simulations at this stage were performed in steady state conditions. The engine performance targets had to comply with practical constraints given by the engine and TC manufacturers:

- Compressor outlet temperature T2
- Turbine inlet temperature T3
- Turbocharger speed T_{RPMMAX}
- Peak cylinder pressure p_{MAX}
- Compressor surge limit according to the steady state compressor map

Due to lack of experimental data the knock occurrence was completely neglected in this study.

3. METHODOLOGY

Three sensitivity studies were selected for this article.

1. Comparison of real and unconstrained turbocharger
2. Usable engine speed range with the single stage turbocharger
3. Achievable low speed torque based on intake cam profile

All studies were performed for important points of the engine full load curve.

4. RESULTS

4.1 REAL VS. UNCONSTRAINED TURBOCHARGER

The main goal of this study was assessment of the possibility of using of Miller cycle [14] within the region of the maximum achievable torque of 380 Nm at 2000 rpm. The top left part of the Figure 3 shows the contours of the brake mean effective pressure (BMEP) in the coordinate system given by intake valve timing in case of the real turbocharger. The horizontal axis represents intake valve opening (IVO) and the vertical axis represents the intake valve closing (IVC). The constant valve lift is assumed, it means that by changing of the mentioned parameters the cam profile is shifted, stretched or narrowed along the crank angle coordinate. Original valve timing is marked in the figure. VTG rack position was chosen with respect to maintain demanded BMEP of 30 bar. It can be observed that retarding of the IVC (so called Millerization) has the limits, given by the parameters of selected turbine in a limit position of the VTG rack (with corresponding value of its efficiency). With further retardation of the IVC the BMEP drops under the demanded limit. The top right Figure displays the same situation when the so-called unconstrained TC is used. It means that for this case the relevant efficiencies were constant within the whole operation region with the values of compressor efficiency C_{eff} = 74 %, and turbine efficiency $T_{eff} \approx$ 70 %. By using the unconstrained turbocharger, the region with demanded BMEP is enlarged and the drop under the limit value does not occur until the very early closing of the intake valves.

Bottom part of the Figure 3 shows a brake specific fuel consumption (BSFC) dependency on intake valve timing for both turbocharger variants. In case of real turbocharger, the IVC retarding causes the increase in the BSFC and it is evident that it is beneficial to keep the original timing of the intake valves. In this case, the benefits of Millerization do not balance the shift of the compressor and turbine characteristics into the region with lower efficiency. Therefore, the resulting BSFC is worsened. On the other hand, in case of the unconstrained turbocharger, the reduction in BSFC is clearly visible, partly due to gradual Millerization and partly due to shift of IVO with retarded values, which for the constant valve timing means reduction of the valve overlap angle. Numerically, this BSFC reduction by means of Millerization can reach 1.5 %.

4.2 USABLE SPEED RANGE GIVEN BY A SINGLE STAGE TURBOCHARGING

The next study deals with a determination of the optimum engine speed for a maximum power output. Small turbine can help to achieve of target BMEP in low and medium engine

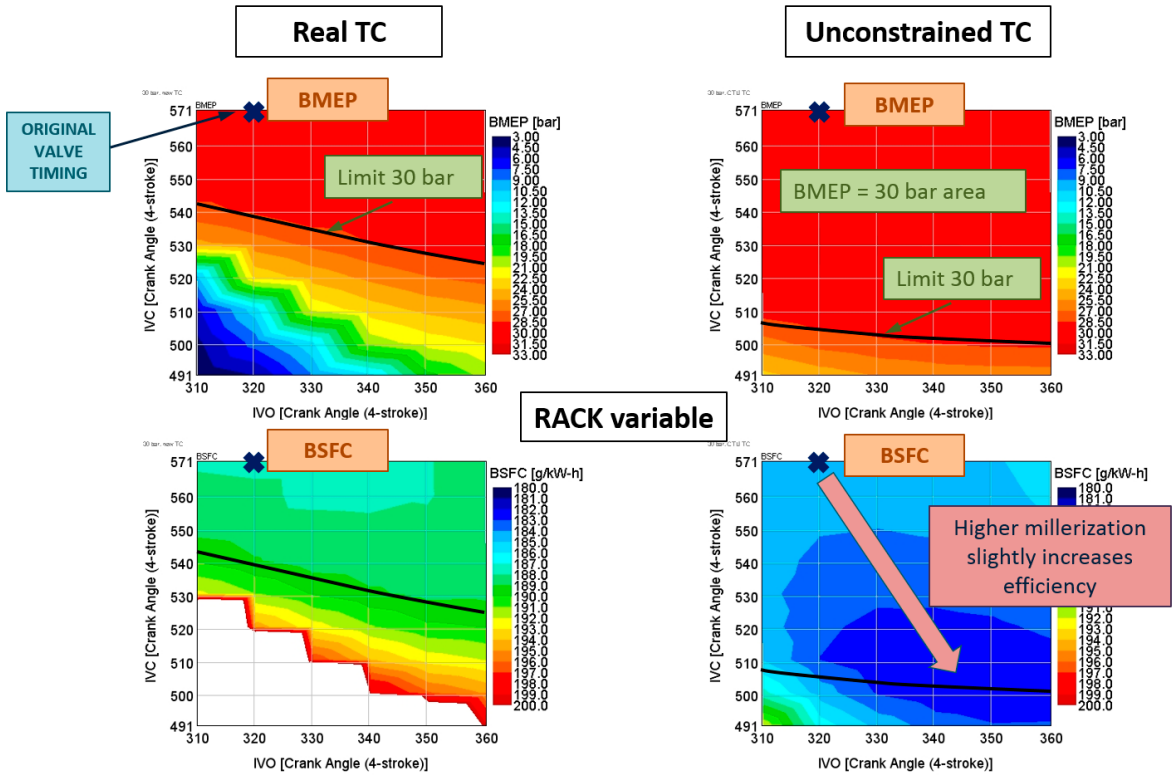

FIGURE 3: Comparison of turbochargers
OBRÁZEK 3: Porovnání turbodmychadel

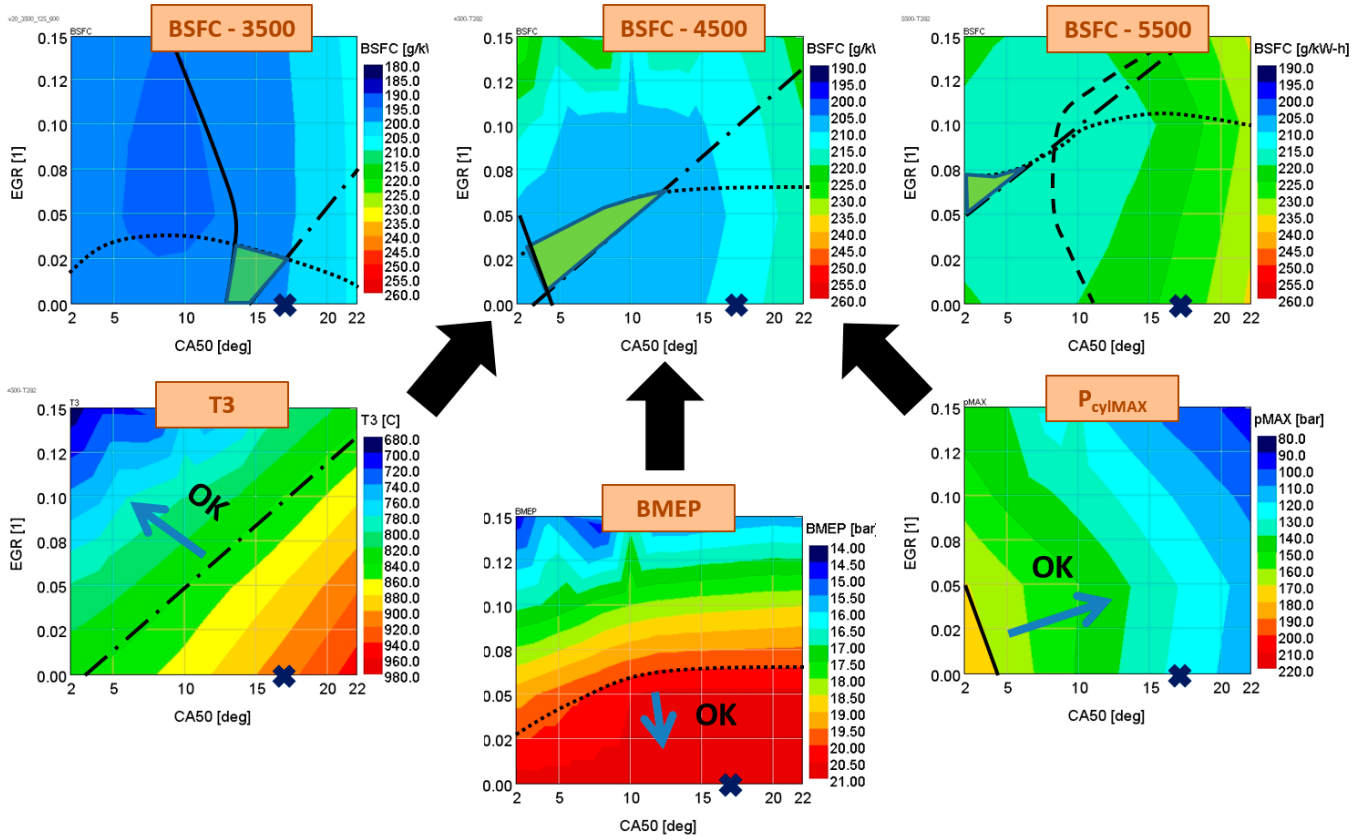

FIGURE 4: Full load speed comparison
OBRÁZEK 4: Porovnání v oblasti maximálního výkonu

speed. However, there is no mass flow reserve for a low pressure (LP) EGR. On the other hand, a larger turbine gives a sufficient flow reserve in the full power regime, but it cannot give a sufficient level of the boost level in low engine speed. Lowering the speed for the maximum power eliminates this compromise and the gas engine characteristics approaches the characteristics of a diesel engine.

The top part of the Figure 4 presents a dependency of the BSFC in the coordinates of the CA50 and ratio of the LP EGR for three engine speed values of 3500, 4500 and 5500 rpm at the power output of 125 kW. The black cross marks a base adjustment of the CA50 and LP EGR. The green region corresponds to area in which all the practical constraints are fulfilled. Bottom figures present in the specific case of 4500 rpm the example of the creation of the working regions. The middle Figure at the bottom of the Figure 4 the BMEP value is depicted by colored contours. The dotted black line limits the region of the complying with the criteria of the target BMEP and the grey arrow shows the direction inside the region. At the bottom right graph, the regions of maximum cycle pressure is displayed by the color contours. The black continuous line limits the region of the fulfilling the criteria with lower peak cylinder pressure than the limit one (p_{MAX}) and again the arrow shows the direction of the appropriate region. At the bottom left graph, the contours show the exhaust temperature upstream of the turbine T3. The dashed line limits the usable region with temperature lower than the limit one.

It is evident from the comparison of the top figure, that the reduction of the BSFC can be achieved by shifting of the speed of the maximum engine power output towards lower values. Reduction or a complete elimination of the need for the demanded LP EGR is another benefit of this shift. Therefore, the speed of 3500 rpm was selected as the maximum power speed.

4.3 LOW SPEED TORQUE CAM PROFILE DEPENDENCE

The last study is related to optimization of the intake cam profiles for the speed of 1000 rpm. This low speed proved to be the key to the TC matching, because of the difficulty with the achievement of the desired BMEP at the base intake cam profiles and valve timing. For practical engine operation the use of the two different intake cam profiles and the mechanism of their continuous phasing are assumed. The first profile is the one adopted from the single cylinder engine being marked as 169CAD. The seeking for an appropriate second profile was the subject of performed optimization. The profile was designed the way that a maximum lift and opening angle was

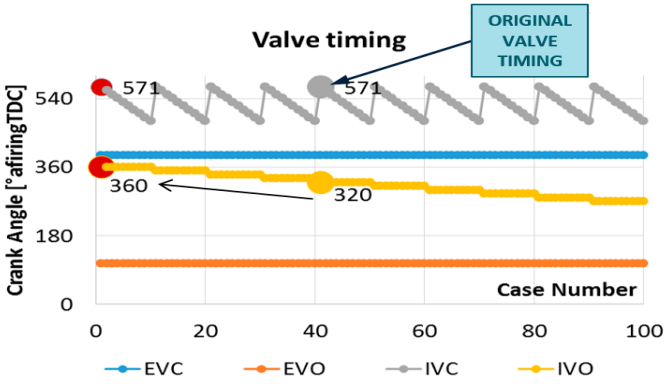

FIGURE 5: Valve timing sweep strategy
OBRÁZEK 5: Strategie vyhledávání časování ventilů

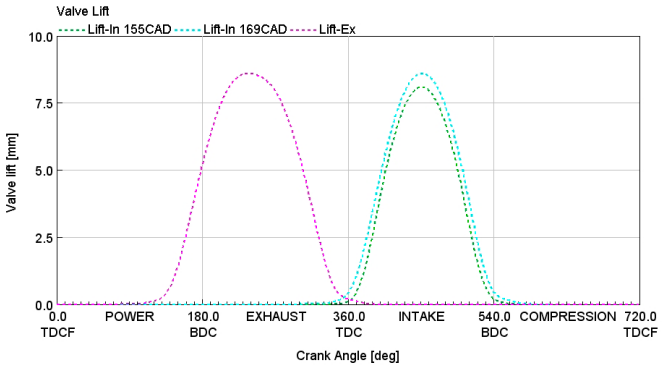

FIGURE 7: Valve profiles
OBRÁZEK 7: Profily ventilů

determined to maintain constant dynamical properties of the valve (the acceleration profile). Parametric study of the intake valve timing was carried out for each speed and TC variant. As a rule, the IVO was kept constant and the IVC was varied simultaneously with the maximum valve lift. Exhaust valve lift profile and timing was kept constant. This strategy is plotted in Figure 5.

One example of the result of this study is plotted in Figure 6. All results are displayed in the coordinate system with IVO as a function of IVC. The black cross marks again the base intake valve timing. The color contours in the top left Figure plots the achieved engine BMEP, the black continuous line represents the limit line of the BMEP. It is evident that the retarded IVO is necessary for achievement of the limit BMEP. This narrows the cam profile and also reduces the valve overlap. The top right Figure shows that BMEP reduces the engine BSFC accordingly, indeed, the increased BMEP causes an increase in temperature T3 and peak cylinder pressure p_{MAX}, which can be observed from the bottom graphs in Figure 6.

After the optimization the resulting variant of the intake cam profile marked as 155CAD was designed.

Both variants of cam profiles are displayed in Figure 7, the 169CAD with the blue dotted line and the 155CAD with a green dotted line. The violet curve describes a profile of the exhaust cam. Further pictures will use the same color coding and line types of the profiles.

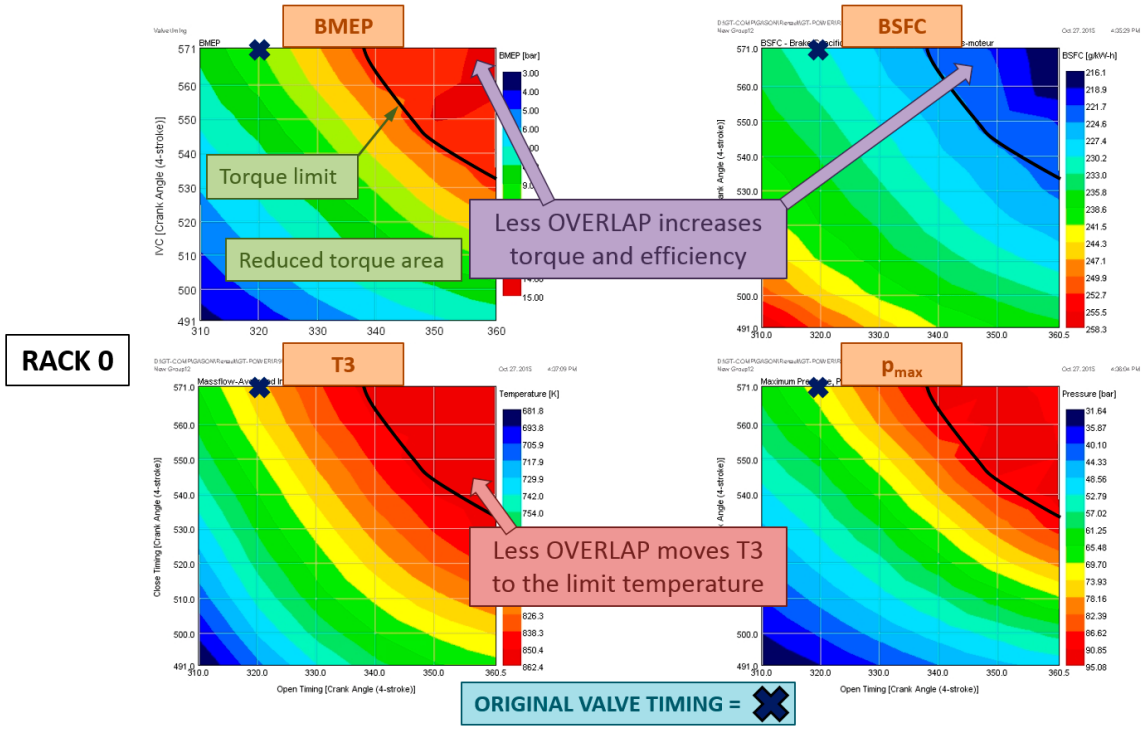

FIGURE 6: Results of valve timing sweep
OBRÁZEK 6: Výsledky vyhledávání časování ventilů

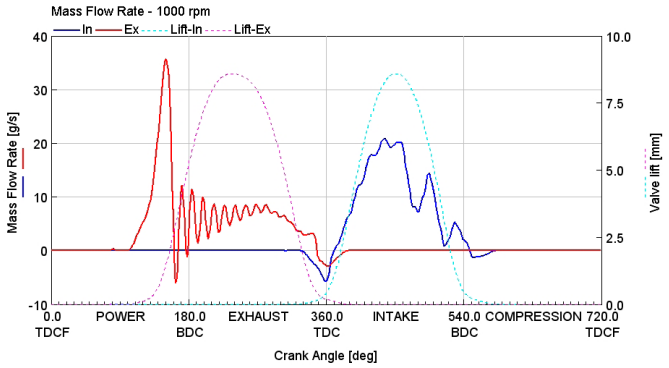

FIGURE 8: Mass flow rate through valves– 169CAD
OBRÁZEK 8: Hmotnostní tok ventily– 169CAD

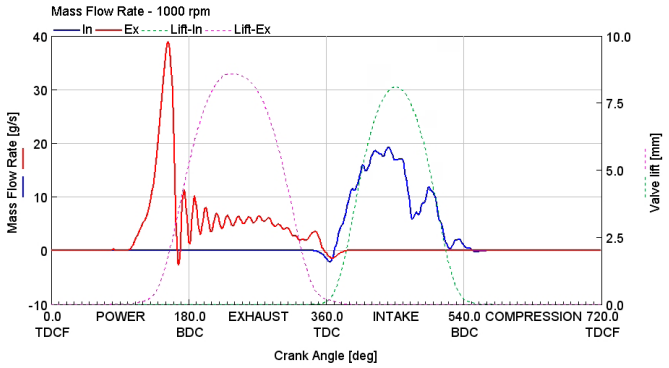

FIGURE 9: Mass flow rates through valves– 155CAD
OBRÁZEK 9: Hmotnostní toky ventily – 155CAD

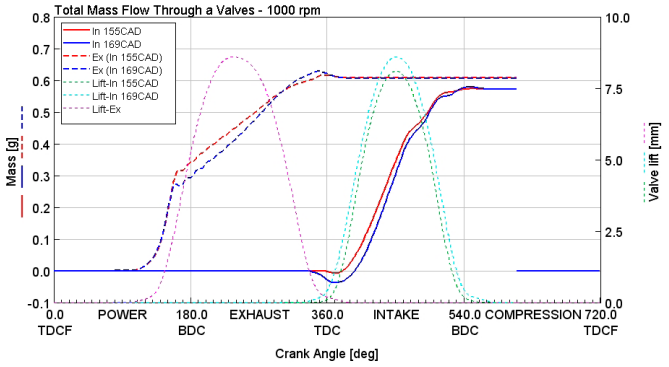

FIGURE 10: Total mass flow through valves
OBRÁZEK 10: Integrál hmotnostních toků pracovní látky proteklé sacími ventily

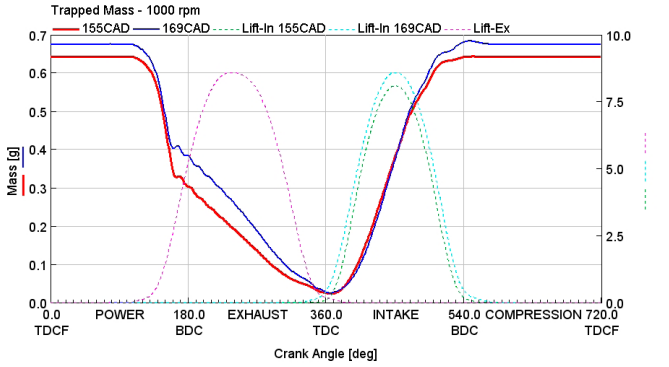

FIGURE 11: Total mass flow through valves
OBRÁZEK 11: Integrál hmotnostních toků pracovní látky proteklé sacími ventily

Figure 8 and Figure 9 show crank angle-based profiles of the instantaneous mass flow through the intake and exhaust valves. Blue line represents the intake air mass flow and the red line plots the instantaneous mass flow of the working substance through the exhaust valve. Dotted line represents the exhaust and intake valve lift profiles according to the color code defined in the previous paragraph.

By comparison of mass flow through the intake valves, it is evident that higher back flow of the cylinder charge occurs during the valve overlap period for the cam with the profile of 169CAD (Figure 8) over the 155CAD (Figure 9) cam profile.

The wider valve overlap for the case 169CAD also increases back flow through the exhaust valves. Figure 10 shows the total integral of the mass flows and confirms previous statements. The red continuous line represents total mass inflow through the intake valve for the 155CAD cam, blue continuous line plots the total mass inflow through the intake valve for the 169CAD case. The exhaust total outflows are plotted with the dashed curves. Dotted lines show all of the valve lift profiles. The difference between inflow and outflow is caused by the quantity of the fuel directly injected into the cylinder.

The higher back flow through the valves affects significantly the residual gas content in the cylinder.

Even though the total mass inflow through the intake valves for both cams after the closing of the intake valves is equal. Figure 11 shows a visible difference in the trapped cylinder charge mass after the intake valve closing. From the composition of the cylinder charge after the intake valve closing the model shows residual gas content for the 155CAD cam of 5.4 % compared to 10.2 % for the 169CAD cam. Higher residual gas content for the 169CAD cam causes the higher demand for the boost pressure to reach equal BMEP as the 155CAD cam. The sufficient boost pressure for the 155CAD cam is 1.63 bar while the 169CAD cam demands 1.82 bar. To achieve higher boost pressure with the same turbocharger, it is necessary to increase turbocharger speed and shift the VGT Rack position toward lower limit value that means to the region of the turbine map, where the mass flow and efficiency values are reduced. This increases the turbine inlet pressure from the value of 1.67 bar for the 155CAD cam to the level of 2.33 bar for the 169CAD cam. Increased turbine inlet pressure results in a higher backflow of the exhaust gas to the cylinder, which amplifies above mentioned phenomenon.

The main effect to reach target level of BMEP by using the narrower cam lies in the reduction of the angle of the valve overlap. This will result in a lower backflow of the air through the intake valves to the intake manifold and the backflow of the

exhaust gas to the cylinder from the exhaust manifold through the exhaust valves. The same amount of the fresh charge in the cylinder can be achieved with lower losses and hence with the lower boost pressure. The demand for the lower boost pressure at engine low speed is essential for the achievement of the demanded engine torque.

5. CONCLUSION

This article presents three selected sub-studies, which were performed during a complex development of the turbocharged CNG engine with high specific power output and with low brake specific fuel consumption.

Possibilities of using a Miller cycle were assessed in the first study. When the use of a real single stage turbocharger is considered, though with the cutting edge performance parameters, at the region of the engine maximum torque, with the gradual Millerization of the cycle the BMEP reduces and the fuel consumption increases as a result of prevailing losses given by the shift of the turbocharger working point towards the regions with lower efficiency. Theoretically, the full advantage of the Millerization can be taken by the use of turbochargers with flat efficiencies of the compressor and turbine within the whole working area.

The selection of the right speed range for maximum engine power is performed in the second study. Assuming the use of a single stage turbocharger for an engine with a high maximum specific torque and power, it is appropriate to adapt the speed range of the gas-fueled engine to the speed range corresponding to the current turbocharged diesel engines. By shifting the speed of maximum power to the lower values, it is possible to achieve the lower engine specific fuel consumption and completely eliminate required EGR.

The use of a single-stage turbocharger to achieve high maximum power at high speed and high torque at low speed on the other hand, may not occur without the change of the valve timing. The third study deals with the design of the valve timing parameters of the intake cam to achieve the high torque at low engine speed. The greatest effect of how the desired torque at low speed can be achieved is to reduce the valve overlap. This can be done by narrowing of the intake cams. By reducing the valve overlap, both the backflow of charge from the cylinder to the intake manifold and the backflow of the exhaust gas through the exhaust valves to the cylinder can be reduced. The reduction of the backflows will result in reduction of the required intake manifold pressure and allows seamless achievement of the desired torque.

ACKNOWLEDGEMENTS

This work has been realized with the support of the European Project GasOn, within the framework of the Horizon 2020 Research and Innovation Programme, under grant agreement No 652816.

This research has been made possible using the support of The Ministry of Education, Youth and Sports, program NPU I (LO), project LO1311: 'Development of Vehicle Centre of Sustainable Mobility'.

The authors would like to thank especially to the partners from IFP for providing with the experimental data from the single cylinder research engine and to all partners in WP04 and WP06 of Horizon 2020 EU project GasOn for valuable cooperation.

LIST OF NOTATIONS AND ABBREVIATIONS

BMEP	brake mean effective pressure
BSFC	brake specific fuel consumption
CA50	combustion anchor angle
CA90-10	combustion duration
C_{eff}	compressor efficiency
CNG	compressed natural gas
EGR	exhaust gas recirculation
EVC	exhaust valve closing
EVO	exhaust valve opening
IVC	intake valve closing
IVO	intake valve opening
LP	low pressure
P2	compressor outlet pressure
RACK	turbine rack position
p_{MAX}	maximum in-cylinder pressure
SI-BDUR	combustion duration
SI-THB50	combustion anchor angle
SI-WIEBE	Wiebe exponent
T2	compressor outlet temperature
T3	turbine inlet temperature
T_{eff}	turbine efficiency
T_{RPMMAX}	turbine maximum speed
VTG	variable turbine geometry
VVT	variable valve timing

REFERENCES

[1] Tilagone, R., Venturi, S., Monnier, G., Natural Gas – an environmentally friendly fuel for urban vehicles: the SMART demonstrator approach, Oil & Gas Science and Technology Vol. 61(1): 155-164, 2006, doi: 10.2516/ogst:2006010x

[2] Wayne, W., Clark, N., and Atkinson, C., A Parametric Study of Knock Control Strategies for a Bi-Fuel Engine, SAETechnical Paper 980895, 1998, doi: 10.4271/980895.

[3] J.F. Preuhs, G. Hofmann, J. Kirwan, Natural gas injection for Low CO2 spark Ignition engine, SAE SIA 2015.

[4] Ferrera, M., Highly Efficient Natural Gas Engines, SAE Technical Paper 2017-24-0059, 2017, doi:10.4271/2017-24-0059.

[5] Baratta, M., Misul, D., Xu, J., Fuerhapter, A. et al., Development of a High-Performance Natural Gas Engine with Direct Gas Injection and Variable Valve Actuation, SAEInt. J. Engines 10(5):2017, doi:10.4271/2017-24-0152.

[6] P. Hofmann, T. Hofherr, G. Hoffmann, J.F. Preuhs, Potential of CNG Direct Injection for Downsizing Engines, MTZ 07-081-2016.

[7] Douailler, F. Ravet, V. Delpech, D. Soleri, B. Reveille, R. Kumar, Direct Injection of CNG on High Compression Ratio Spark Ignition Engine: Numerical and Experimental Investigation, SAE International 2011-01-0923.

[8] Vitek, O. and Macek, J., Thermodynamic Potential of Electrical Turbocharging for the Case of Small Passenger Car ICE under Steady Operation, SAE Technical Paper 2017-01-0526, 2017, doi:10.4271/2017-01-0526.

[9] Bogomolov, S., Dolecek, V., Macek, J., Mikulec, A. et al., Combining Thermodynamics and Design Optimization for Finding ICE Downsizing Limits, SAE Technical Paper 2014-01-1098, 2014, doi:10.4271/2014-01-1098.

[10] Martin, S., Beidl, C., and Mueller, R., Responsiveness of a 30 Bar BMEP 3-Cylinder Engine: Opportunities and Limits of Turbocharged Downsizing, SAE Technical Paper 2014-01-1646, 2014, doi:10.4271/2014-01-1646.

[11] Turner, J., Popplewell, A., Patel, R., Johnson, T. et al., Ultra Boost for Economy: Extending the Limits of Extreme Engine Downsizing, SAE Int. J. Engines 7(1):2014, doi:10.4271/2014-01-1185.

[12] GASON Project Official Website. [Cit. 2018-12-30] Available on: http://www.gason.eu

[13] GT-POWER – GT-Suite Version 7.4, Gamma Technologies Inc., USA, 2000

[14] Luisi, S., Doria, V., Stroppiana, A., Millo, F. et al., Experimental Investigation on Early and Late Intake Valve Closures for Knock Mitigation through Miller Cycle in a Down-sized Turbocharged Engine, SAE Technical Paper 2015-01-0760, 2015, doi:10.4271/2015-01-0760.

[15] Rouleau, L., Serrano D., Lecointe B., CNG direct injection spark-ignition engine with high turbulence and high compression ratio: numerical and experimental investigations [online]. 2018 [cit. 2018-12-30]. Available on: http://www.gason.eu/documents/get_doc/714

[16] Škarohlíd M. Advanced engine control possibilities to react on fuel features. MECCA 02 2011, pp. 28-44. ISSN 1214-0821

DE GRUYTER OPEN

10.1515/mecdc-2018-0002

IMPLICATION OF CYCLE-TO-CYCLE VARIABILITY IN SI ENGINES

KAREL PÁV
Technická univerzita v Liberci, Katedra vozidel a motorů, Studentská 2, Liberec 461 17, Czech Republic
Email: karel.pav@tul.cz

ABSTRACT

The paper deals with utilization of an adaptive combustion model in order to simulate cycle-to-cycle combustion variability of SI engines. The used empirical adaptive combustion model consists of two parts: the first part for ignition delay prediction and the second part for in-cylinder combustion process description. There is proved mutual independence of these two phases and shown their characteristics in terms of cycle-to-cycle variability. The practical utilization of the cycle-to-cycle variability simulation is demonstrated by computational analysis of various variability levels at different engine operational points in order to assess its impact on engine fuel consumption. The calculation results are generalized for SI gasoline engines independent of both engine load and combustion rate as well.

KEYWORDS: SI ENGINE, CYCLE-TO-CYCLE VARIABILITY, ADAPTIVE COMBUSTION MODEL, SPARK TIMING, IGNITION DELAY, VARIABILITY FACTOR, FUEL CONSUMPTION.

SHRNUTÍ

Tento příspěvek se zabývá použitím adaptivního modelu hoření za účelem simulace mezicyklové variability hoření ve válci zážehového spalovacího motoru. Použitý numerický adaptivní model hoření sestává ze dvou částí: první část pro predikci průtahu zážehu a druhá část pro popis vlastního spalovacího procesu ve válci motoru. Je zde ukázána vzájemná nezávislost těchto dvou částí a jejich vlastnosti s ohledem na mezicyklovou variabilitu. Praktické využití simulace mezicyklové variability je demonstrováno na výpočtové analýze různých úrovní variability v různých pracovních bodech motoru s cílem ohodnotit dopad mezicyklové variability na spotřebu paliva. Výsledky výpočtů jsou zobecněny pro zážehové benzínové motory a lze je využít nezávisle jak na zatížení motoru, tak i na rychlosti hoření.

KLÍČOVÁ SLOVA: ZÁŽEHOVÝ MOTOR, MEZICYKLOVÁ VARIABILITA, ADAPTIVNÍ MODEL HOŘENÍ, PŘEDSTIH ZÁŽEHU, PRŮTAH ZÁŽEHU, FAKTOR VARIABILITY, SPOTŘEBA PALIVA.

1. INTRODUCTION

The cycle-to-cycle combustion variability is a well-known phenomenon among engineers dealing with engine development. The dispersion in combustion process is generally caused by three factors: the variation in turbulent gas motion in a cylinder during combustion; the variation in the amounts of fuel, air, and burned gas present in a given cylinder during each cycle; variations in mixture composition within the cylinder near the spark plug – due to variations in mixing between air, fuel, recirculated exhaust gas and residual gas [3]. The strongest impact on resulting cycle-to-cycle combustion variability has the onset of the combustion process (flame kernel development) which is particularly essential in case of standard SI engines. The pre-flame period is negatively affected by non-homogeneous mixture in vicinity of the spark plug and too weak or too intensive charge movement [1], [4], [9]. The further flame propagation is strongly influenced by the combustion chamber topology and the in-cylinder turbulence intensity, while the most dominant factor in terms of cycle-to-cycle variation is the turbulence intensity which varies substantially among individual cycles [10].

Various measures of the cycle-to-cycle combustion variability are widely used. They can be defined in terms of variations in the cylinder pressure between different cycles or in terms of variations in the parameters of the burning process. The most used quantities of pressure-related parameters are the maximum cylinder pressure, the crank angle at which this maximum pressure occurs, the maximum rate of pressure rise and the indicated mean effective pressure (IMEP). The burn-rate-related parameters are the maximum heat-release rate or mass burning rate, the crank angle at 50% of mass burned

fraction, the flame development angle and the rapid burning angle [3]. The indicated mean effective pressure is very sensitive to measurement accuracy, especially when non water-cooled sensors with high cyclic temperature drift are used [7].

The main task of this paper is to investigate cycle-to-cycle variability in terms of combustion process differences, i.e. without turbulence and other effects on changes in mass of charge trapped in the cylinder. The investigation of cylinder-to-cylinder variation sakes is also not a scope of this paper. Therefore, the most convenient measure for the cycle-to-cycle variability assessment is the standard deviation (SDEV) in crank angle at 50% of mass burned fraction $MBF50\%$ which reflects the phasing of combustion process and is nearly independent of charging variations

$$SDEV\,(MBF50\%) = \sqrt{\frac{\sum \left(MBF50\% - \overline{MBF50\%}\right)^2}{n-1}} \qquad (1)$$

Coefficient of variation (COV) can be used as an alternative measure of the maximum cylinder pressure $PMAX$ in form:

$$COV\,(PMAX) = \frac{100}{PMAX}\sqrt{\frac{\sum \left(PMAX - \overline{PMAX}\right)^2}{n-1}} \qquad (2)$$

The frequently applied limit value for smooth engine run is $COV(PMAX) < 15\%$. However, this parameter has to be used carefully, especially when the spark timing is not set to its optimum. Typical values of coefficient of variation of maximum cylinder pressure and standard deviation in crank angle at 50% of mass burned fraction at optimum ignition timing are shown in Figure 1. All displayed engine operational points in these maps are used for further computational analysis of the potential for a fuel consumption reduction in this paper. At very low engine load at $IMEP < 1$ bar (not displayed in Figure 1) the cycle-to-cycle variability is usually increasing due to lower compression pressure and temperature and higher content of residual gas in the cylinder.

The relationship between two above mentioned measures in Figure 2 is shown. The correlation between these two quantities is for maximum brake torque (MBT) spark timing very close. Engine

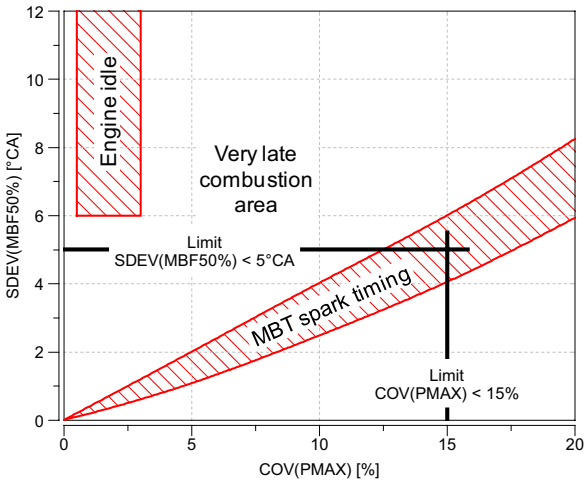

FIGURE 2: Relationship between coefficient of variation of maximum cylinder pressure and standard deviation in crank angle at 50% of mass burned fraction.

OBRÁZEK 2: Vzájemná korelace mezi variačním koeficientem maximálního tlaku a směrodatnou odchylkou úhlu natočení klikového hřídele při 50% vyhoření náplně válce.

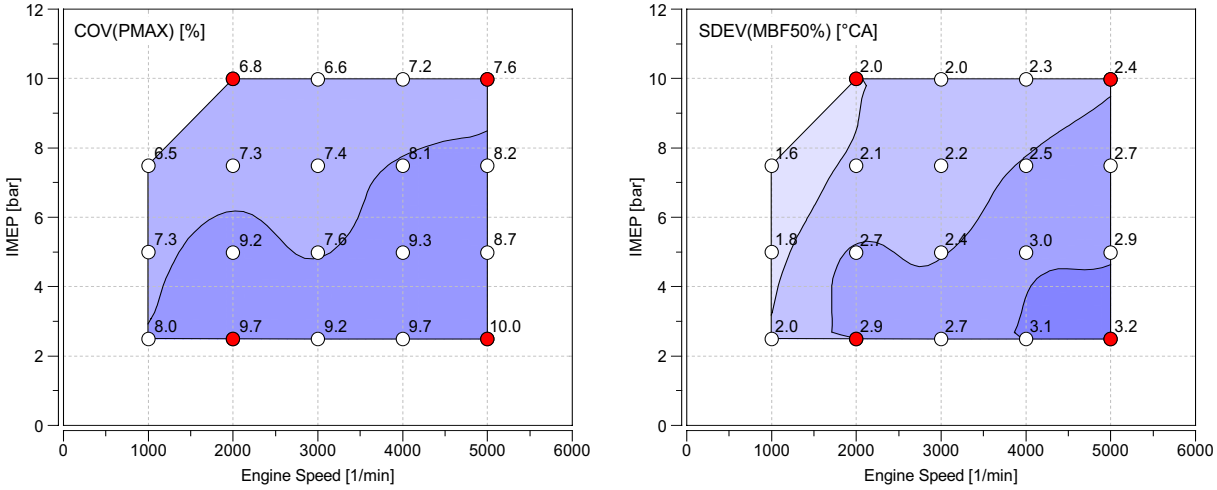

FIGURE 1: Typical values of coefficient of variation of maximum cylinder pressure and standard deviation in crank angle at 50% of mass burned fraction. An example for naturally aspirated four-cylinder SI gasoline engine of swept volume 1.6 dm³. Red colored points mark the engine operational points where a deeper computational analysis has been carried out.

OBRÁZEK 1: Typické hodnoty variačního koeficientu maximálního tlaku a směrodatné odchylky úhlu natočení klikového hřídele při 50% vyhoření náplně válce. Příklad pro nepřeplňovaný čtyřválcový zážehový benzínový motor o zdvihovém objemu 1,6 dm³. Červené body označují režimy motoru, při kterých byla provedena detailnější výpočtová analýza.

operational points with exceptional spark timing lie outside this region, typically engine idle, as has been mentioned above.

2. DESCRIPTION OF ADAPTIVE COMBUSTION MODEL

For the simulation of different conditions during combustion process the empirical adaptive combustion model has been developed [4]. This model offers very simple implementation of variability control because it consists of two independent parts. The first part predicts the ignition delay Dj_{ign} which is defined as a crank angle difference between spark ignition and very first sign of the heat release, as graphically shown in Figure 3. The second part is the flame propagation process. These two parts have been proven as an independent processes [5].
The crank angle duration of the ignition delay is mathematically

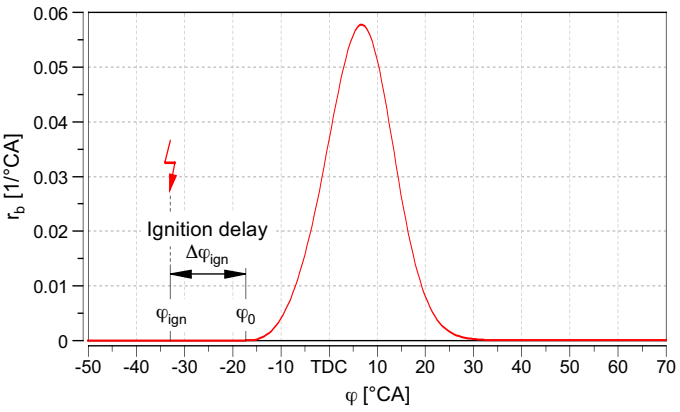

FIGURE 3: Normalized burn rate r_b, definition of the ignition delay Dj_{ign}.
OBRÁZEK 3: Jednotková rychlost hoření r_b, definice průtahu zážehu Dj_{ign}.

given by improved empirical formula originally coming from [4], [5]. The investigation of more SI engines allowed to achieved new form

$$\Delta\varphi_{ign} = A_{ign}\, A_{ign,v} 5\times10^{4}\, n^{0.7}\, p_{ign}^{-0.2}\, T_{ign}^{-2} \left[0.2 + \left(\lambda_{mix} - 0.8\right)^2\right] \times \times \left(1 + x_{r,st}\right)^5 \qquad (3)$$

$$[°CA, 1, 1, 1/\mathrm{min}, \mathrm{bar}, \mathrm{K}, 1, 1]$$

The formula improvement consists in change of multiplier and single exponents based on regression analysis of extended experiments. Besides calibration factor A_{ign} there is also multiplier $A_{ign,v}$ which is used for generation of the cycle-to-cycle variability. The ignition delay depends on the engine speed n, in-cylinder pressure p_{ign} and mean in-cylinder temperature T_{ign} at the moment of the spark ignition. Relative air/fuel ratio in unburned mixture λ_{mix} is given by relative air/fuel ratio λ and by residual mass fraction x_r in the cylinder

$$\lambda_{mix} = \lambda + x_r \frac{\lambda - 1}{1 - x_r} \quad \forall \quad \lambda > 1$$
$$\lambda_{mix} = \lambda \quad \forall \quad \lambda \le 1 \qquad (4)$$

Mass fraction of stoichiometric residual gases $x_{r,st}$ is given by formula

$$x_{r,st} = x_r \frac{1 + L_{st}}{1 + \lambda L_{st}} \quad \forall \quad \lambda > 1$$
$$x_{r,st} = x_r \quad \forall \quad \lambda \le 1 \qquad (5)$$

where L_{st} denotes stoichiometric wet air/fuel ratio.
The main combustion phase is described by the change of mass fraction of burned gas x_b during combustion. Improved empirical formula covering wider range of SI engines has form

$$\frac{dx_b}{d\varphi} = A_b A_{b,v} 15\times10^{-5}\, n^{-0.5}\, p^{0.3}\, T^{0.4} \left(\frac{V_c}{V}\right)^{1.5} \times \times \left[0.8 - \left(\lambda_{mix} - 0.83\right)^2\right]^{4.4} \left(1 - x_{r,st}\right)^{4.4} x_{mix}^{1.1} \left(\varphi - \varphi_0\right)^{2.5} \qquad (6)$$

$$[1/°CA, 1, 1, 1/\mathrm{min}, \mathrm{bar}, \mathrm{K}, \mathrm{m}^3, 1, 1, 1, °CA]$$

where p, T and V denotes instantaneous in-cylinder pressure, mean in-cylinder temperature and cylinder volume respectively. V_c is the compression volume at piston top dead center (TDC) and x_{mix} is the instantaneous unburned mixture mass fraction in the cylinder. The multiplier $A_{b,v}$ which extends the calibration factor A_b is used for the cycle-to-cycle variability simulation. The meaning of the angles j and j0 follows from Figure 3. The change of the mass of burned fuel m_{fuel} is then

$$\frac{dm_{fuel}}{d\varphi} = \frac{m_c}{1 + \lambda L_{st}} \frac{dx_b}{d\varphi} \qquad (7)$$

where m_c is the total cylinder mass.

2.1 DETERMINATION OF CALIBRATION AND VARIABILITY FACTORS

For the determination of calibration and variability factors, it is necessary to evaluate sufficient volume of measured data – at least the sequence of 200 cycles. Indicated pressure traces have to undergo thermodynamic analysis in terms of getting mean in-cylinder temperature and normalized burn rate r_b which is crucial parameter. The determination of the single cycle-based factor for the ignition delay comes from rearrangement of equation (3)

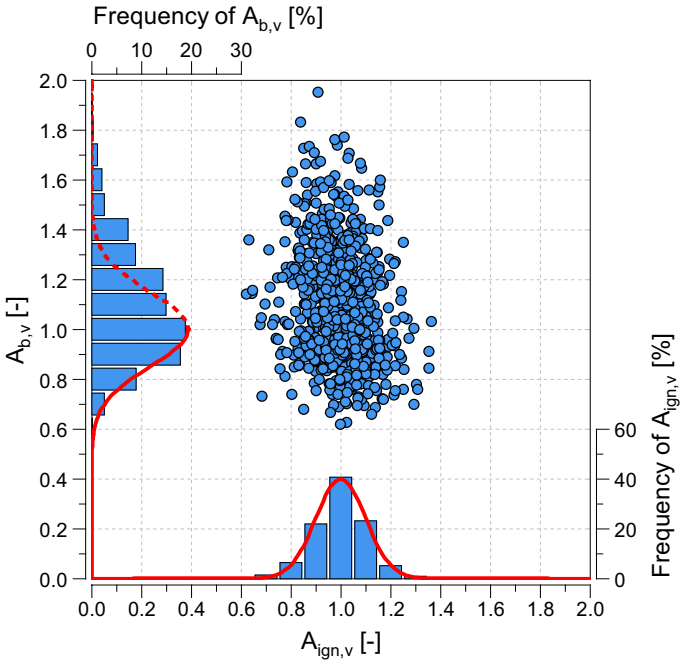

FIGURE 4: Typical distribution of variability factors for ignition delay $A_{ign,v}$ and main combustion phase $A_{b,v}$ over 870 successive cycles. Traces of the normal distribution, dashed line represents a range where the normal distribution doesn't coincide with measurement.
OBRÁZEK 4: Typické rozdělení faktorů pro variabilitu průtahu zážehu $A_{ign,v}$ a variabilitu vlastního procesu hoření $A_{b,v}$ během 870 po sobě následujících pracovních cyklů. Křivky reprezentující normální rozdělení, čárkovaná čára představuje oblast, kdy se normální rozdělení neshoduje s měřením.

$$A_{ign}\,A_{ign,v} = \\ = \frac{\Delta\varphi_{ign}}{5\times10^{4}\,n^{0.7}\,p_{ign}^{-0.2}\,T_{ign}^{-2}\left[0.2+\left(\lambda_{mix}-0.8\right)^{2}\right]\left(1+x_{r,st}\right)^{5}} \tag{8}$$

where Dj_{ign} is the measured ignition delay for each single cycle. The product $A_{ign}A_{ign,v}$ consists of the main calibration factor A_{ign} which is constant for the sequence of all cycles and of the variability factor $A_{ign,v}$ which deviates from value 1 in the current cycle

$$A_{ign} = \text{median}\left(A_{ign}A_{ign,v}\right) \\ A_{ign,v} = \frac{A_{ign}A_{ign,v}}{\text{median}\left(A_{ign}A_{ign,v}\right)} \tag{9}$$

A similar procedure has to be done for the main combustion phase. For the determination of the single cycle-based factor $A_b\,A_{b,v}$ used in equation (6), the most important region at the rate of burning curve (see Figure 3) is the vicinity of its maximum. Therefore, this factor can be determined based on measured in-cylinder conditions at 50% of mass burned fraction. Thus, from equation (6) can be derived

$$A_b\,A_{b,v} = \frac{r_{b,50\%}}{15\times10^{-5}\,n^{-0.5}\,p_{50\%}^{0.3}\,T_{50\%}^{0.4}\left(\frac{V_c}{V_{50\%}}\right)^{1.5}\left[0.8-\left(\lambda_{mix}-0.83\right)^{2}\right]^{4.4}\left(1-x_{r,st}\right)^{4.4}\left(1-x_r\right)^{0.1}0{,}5^{1.1}\left(\varphi_{50\%}-\varphi_0\right)^{2.5}} \tag{10}$$

Similarly to the previous case, the calibration factor A_b is constant over the sequence of all cycles and variability factor $A_{b,v}$ deviates from value 1 according to the current cycle

$$A_b = \text{mode}\left(A_bA_{b,v}\right) \doteq \text{median}\left(A_bA_{b,v}\right) \\ A_{b,v} = \frac{A_bA_{b,v}}{\text{mode}\left(A_bA_{b,v}\right)} \doteq \frac{A_bA_{b,v}}{\text{median}\left(A_bA_{b,v}\right)} \tag{11}$$

Here, the mode function should be used for an accurate evaluation because of asymmetrical frequency distribution of the factor $A_b\,A_{b,v}$. The mode of a set of data values is the value that appears most often. Since the mode determination can cause some difficulties, the median has been used instead for an approximation. Typical distribution of both mentioned variability factors is shown in Figure 4. It is obvious that factors $A_{ign,v}$ and $A_{b,v}$ are mutually almost independent, although a cross-correlation between ignition delay and combustion rate can be observed [8], [11]. While the frequency distribution of $A_{ign,v}$ is quite symmetrical and corresponds to normal distribution, the distribution of $A_{b,v}$ is asymmetrically outspread to its higher values.

A decision whether a distribution is symmetrical or not is possible by means of the adjusted Fisher-Pearson standardized moment coefficient also called skewness [2]. The magnitude of skewness describes how symmetrical a distribution is about its mean. A positive value indicates a leaning to the right of mean and a negative value indicates a leaning to the left. The skewness is defined as

$$SKEW\left(x\right) = \frac{n}{\left(n-1\right)\left(n-2\right)}\sum\left(\frac{x-\bar{x}}{SDEV\left(x\right)}\right)^{3} \tag{12}$$

From the thermodynamic analysis of a measured in-cylinder pressure can be observed that quantities like indicated mean effective pressure, maximum heat-release rate, maximum cylinder pressure or the crank angle at 50% of mass burned fraction follow almost normal distribution because their skewness for 200 cycles is within the 90 percent range ±0.28 [2]. Sequences of calculated variability factors according to equations (9) and (11) with both measured and by means of simulation restored chosen quantities are depicted in Figure 5.

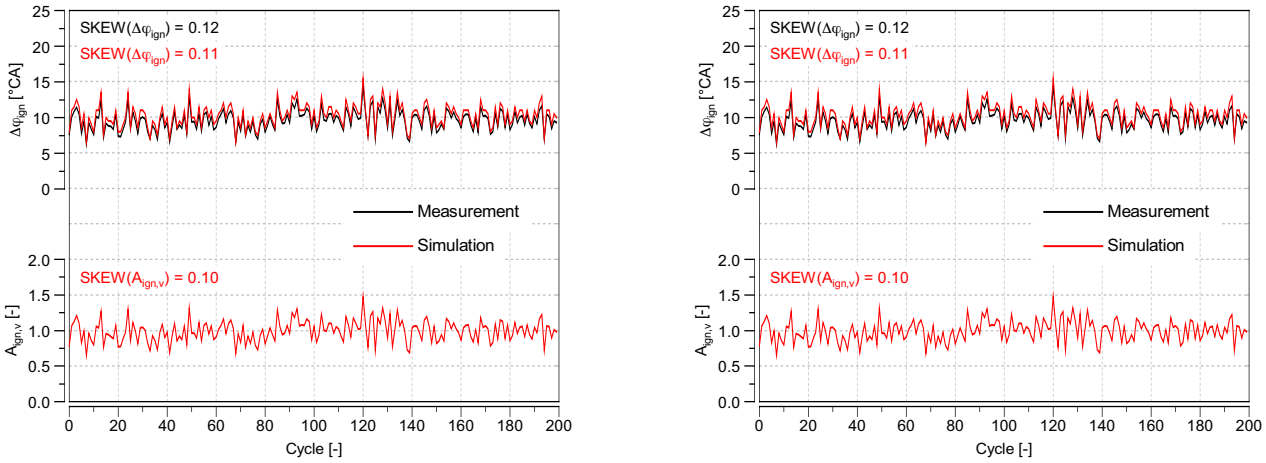

FIGURE 5: Sequence of measured and simulated ignition delay for 200 successive cycles, used variability factors for ignition delay $A_{ign,v}$ and main combustion phase $A_{b,v}$, values of maximum cylinder pressure and crank angle at 50% of mass burned fraction. Engine speed 3000 min-1, $IMEP$ = 5 bar.

OBRÁZEK 5: Sekvence naměřených a simulovaných průtahů zážehu pro 200 po sobě následujících cyklů, použité hodnoty faktorů pro variabilitu průtahu zážehu $A_{ign,v}$ a variabilitu vlastního procesu hoření $A_{b,v}$, maximální spalovací tlaky a úhel natočení klikového hřídele při 50% vyhoření náplně válce. Otáčky motoru 3000 min-1, $IMEP$ = 5 bar.

For purely simulation purposes, some artificial patterns of variability factors are desirable. As the distribution of the variability factor for ignition delay $A_{ign,v}$ is symmetrical, one can write it in symbolic form

$$A_{ign,v} = 1^{+\sigma}_{-\sigma} \tag{13}$$

where s represents a random positive number, which deviates from zero and follows normal distribution with its median in 0. Due to the asymmetrical frequency distribution of the main combustion variability factor $A_{b,v}$ the more detail analysis had to be carried out in computational tool [6] assuming calculation with the median in equation (11). In order to achieve almost normal frequency distribution of the maximum cylinder pressure and other above-mentioned quantities the variation of the combustion variability factor has to follow relation

$$A_{b,v} = 1^{+\frac{\sigma}{1-\sigma}}_{-\sigma} \tag{14}$$

where s represents a random positive number, which deviates from zero and follows normal distribution with its median in 0, s value in equation (14) is independent of that used in equation (13). Note that the number of values lower and higher than 1 is equal, thereby the frequency distribution of the function (14) doesn't exactly coincide with the distribution in Figure 4 but the use of this relation for simulation purposes is quite sufficient.

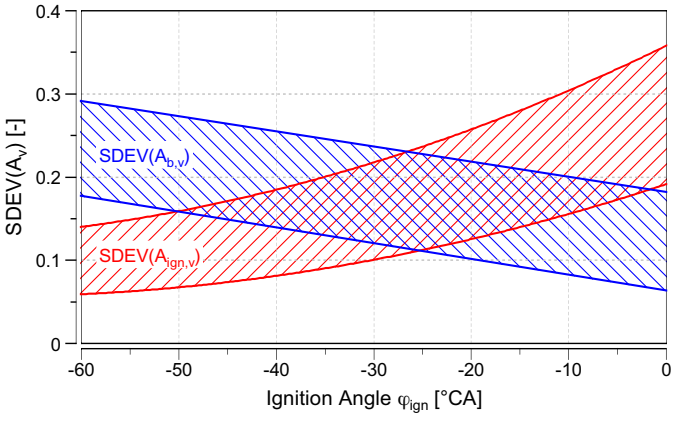

FIGURE 6: Typical values of standard deviation in variability factors $A_{ign,v}$ and $A_{b,v}$ as a function of ignition angle, bands of occurrence.

OBRÁZEK 6: Typické hodnoty směrodatných odchylek faktorů pro variabilitu průtahu zážehu $A_{ign,v}$ a variabilitu vlastního procesu hoření $A_{b,v}$ v závislosti na předstihu zážehu, pásma výskytu.

2.2 MAGNITUDE OF VARIABILITY FACTORS

As a measure of the cycle-to-cycle variability level can be considered the standard deviation in variability factors $A_{ign,v}$ and $A_{b,v}$ whose sequence centric values correspond to the median of value 1, see equations (9) and (11). This approach allows separate assessment of preflame and main combustion phase. The calculation for ignition delay is simple but the standard deviation in combustion variability factor $A_{b,v}$ has to be evaluated for values lower or equal to 1 only due to its asymmetrical distribution

$$SDEV\left(A_{ign,v}\right) = \sqrt{\frac{\Sigma\left(A_{ign,v} - 1\right)^2}{n - 1}}$$

$$SDEV\left(A_{b,v}\right) = \sqrt{\frac{\Sigma\left(A_{b,v} - 1\right)^2}{n - 1}} \quad \forall \quad A_{b,v} \le 1 \tag{15}$$

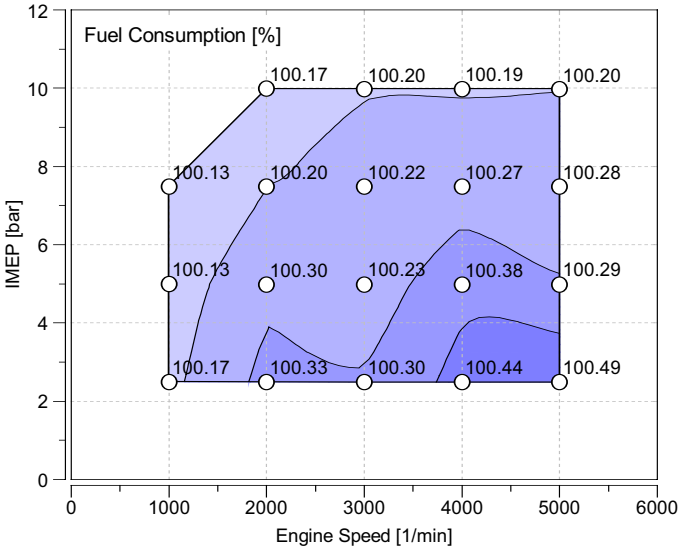

FIGURE 7: Calculated fuel consumption increase due to the cycle-to-cycle variability levels related to Figure 1.
OBRÁZEK 7: Vypočtené navýšení spotřeby paliva vlivem mezicyklové variability dané parametry dle Obrázku 1.

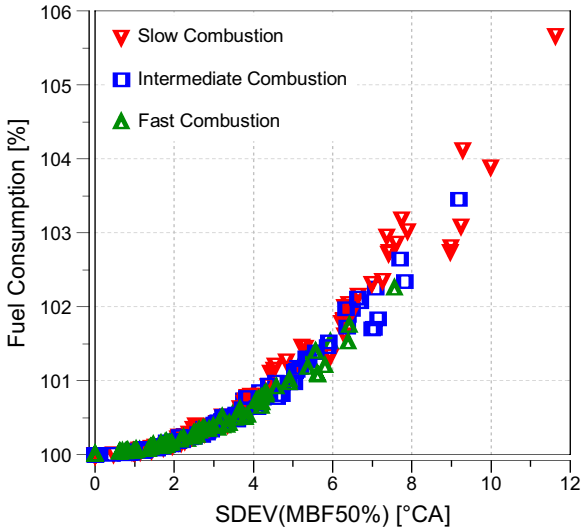

FIGURE 8: Fuel consumption as a function of standard deviation in crank angle at 50% of mass burned fraction, calculation results for red colored engine operational points from Figure 1 considering different combustion rates at optimum spark timing.
OBRÁZEK 8: Spotřeba paliva v závislosti na směrodatné odchylce úhlu natočení klikového hřídele při 50% vyhoření náplně válce, výsledky výpočtů pro červeně označené body v Obrázku 1 s uvažováním různých rychlostí hoření při optimálním předstihu zážehu.

Typical values of standard deviation in variability factors as a function of ignition angle which has been found as a strong influencing parameter are shown in Figure 6. Other parameters like an engine speed, mean indicated pressure, combustion duration, etc. don't show so close correlation. In general, advancing the spark increases the magnitude of ignition delay and also its standard deviation. The shortest ignition delay can be observed at ignition angles around TDC when both in-cylinder pressure and temperature reach the highest values – see the relation in equation (3). The variability factor $A_{ign,v}$ induces relative changes in ignition delay, therefore $SDEV(A_{ign,v})$ is increasing with decreasing of mean value of the ignition delay itself. If the ignition delay is close to zero the changes in the variability factor $A_{ign,v}$ have no impact on the cycle-to-cycle variability level at all.

3. SIMULATION OF CYCLE-TO-CYCLE VARIABILITY

The practical use of the cycle-to-cycle variability simulation is demonstrated on investigation of fuel saving potential by variability level reduction. The reference conditions have been given by cycle-to-cycle variability levels of the SI gasoline engine from Figure 1. All measured engine operational points have undergone thermodynamic analysis in order to get calibration and variability factors using equations (8) – (11). The calibration factors and sequences of variability factors have been then used for fuel consumption calculation at optimum ignition timing for all engine operational points. This calculation has been carried out in modified calculation software [6] for 200 successive cycles. Afterwards, the variability level had been suppressed to zero ($A_{ign,v} = 1$, $A_{b,v} = 1$) and calculated hypothetical fuel consumption at optimum ignition timing was compared with previous results. The outcome of this computational analysis is presented in Figure 7. Displayed values represent fuel consumption increase due to the cycle-to-cycle variability levels related to Figure 1. One can see the maximum fuel consumption saving of magnitude 0.49%. However, this value is not even entirely achievable in practice due to the ultimate minimum variability level.

3.1 GENERALIZATION OF RESULTS

The main goal of the results generalization was to assess a wide range of engine operational points including different combustion processes. A detailed simulation analysis has been carried out at four engine operational points – red colored points in Figure 1. In order to evaluate entire scale of combustion rates it was necessary to generate artificial sequences of the variability factors of different variability levels as an input for the calculation. The standard deviations in variability factors calculated according to (15) have been chosen in range of á0, 0.4ñ with step 0.1. Thereby, the calculation input was formed by the grid of 5x5 variability factor patterns. The artificial generation of the variability factors with respect of relations (13) and (14) has been done in LabVIEW 2010 environment by using function *Discrete Random*. Additionally, in order to consider the influence

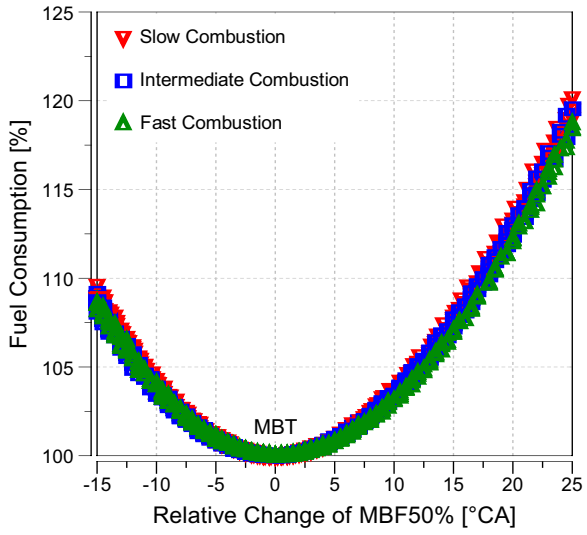

FIGURE 9: Fuel consumption as a function of relative change of crank angle at 50% of mass burned fraction.
OBRÁZEK 9: Spotřeba paliva v závislosti na relativní změně úhlu natočení klikového hřídele při 50% vyhoření náplně válce.

of different combustion rates the calculation was carried out for three different calibration factors A_b = 0.5, 1 and 2 which represent slow, intermediate and fast combustion respectively. The calibration factor for ignition delay was invariable A_{ign} = 1. The simulation of 75 events at each of four engine operational points was performed in modified calculation software [6] for 200 successive cycles. The calculation results are summarized in graphical form in Figure 8. The relative fuel consumption 100% is assigned to uniform combustion without any cycle-to-cycle variability implication. From the practical point of view it doesn't matter how the resulting variability level has been achieved – by variation of the ignition delay or of the main combustion phase. Therefore, the impact of the cycle-to-cycle variability on fuel consumption can be simply expressed as a function of standard deviation in crank angle at 50% of mass burned fraction which is easy detectable parameter. One can see that the influence of the combustion rate is marginal. Assuming optimum spark timing and usual values of $SDEV(MBF50\%)$ = 3°CA a theoretical potential for fuel consumption improvement in terms of cycle-to-cycle variability reduction can be estimated to 0.4% only. This value corresponds to the results in Figure 7.

Above mentioned marginal influence of the combustion rate can be explained by following computational analysis at four red colored engine operational points depicted in Figure 1. The engine fuel consumption in steady state mode was calculated with various spark timing for three different combustion rates. The results after recalculation to relative change of the crank angle at 50% of mass burned fraction are shown in Figure 9. The minimum fuel consumption corresponds to maximum brake torque spark timing (MBT), as expected. A leaning of the angle $MBF50\%$ either to lower or higher values leads to fuel consumption increase almost independent of the engine load or combustion rate magnitude like that in Figure 8. Therefore, the chart in Figure 8 can be considered as generally valid for SI gasoline engines with optimum spark timing. If the ignition timing is far from its optimum, the cycle-to-cycle variability level doesn't influence engine fuel consumption so much, because the relationship between relative change of the angle $MBF50\%$ and fuel consumption is nearly linear as shown in Figure 9. The location of the mean value of the angle $MBF50\%$ affects the fuel consumption almost an order of magnitude greater than a cycle-to-cycle variability. If a knocking is considered the situation is more complex. Under knocking conditions, the spark advance has to be retarded, i.e. the angle $MBF50\%$ is shifted from MBT point to higher values, which leads to significantly higher fuel consumption. Since the knock event is related to stochastic nature of combustion the reduction of cycle-to-cycle variability suppresses a knock occurrence and thus allows advancing combustion [8].

4. CONCLUSION

The cycle-to-cycle variability is often discussed topic related to overall engine efficiency and thereby a subject for optimization. The simulation of the cycle-to-cycle variability is possible by using empirical adaptive combustion model extended by variability factors. Individual patterns of variability factors for ignition delay and main combustion phase, which are independent of each other, can be either measured or artificially generated according to required variability level. This approach leads to very good agreement with real engine behavior.

Although it is technically possible to reduce cycle-to-cycle variability the carried-out sensitivity analysis without knock limitation at optimum spark timing shows that achievable engine fuel consumption reduction is up to 0.4% only. On the other hand, with an increasing variability the engine efficiency deterioration is more progressive, thus should be avoided. The right spark timing regarding the mean value of the crank angle at 50% of mass burned fraction has much stronger effect on engine fuel consumption than a cycle-to-cycle variability.

REFERENCES

[1] BEROUN S., PÁV K. (2013). Vybrané statě z vozidlových spalovacích motorů, Liberec, ISBN 978-80-7372-957-8

[2] DOANE D. P., SEWARD L. E. (2011). Measuring Skewness: A Forgotten Statistic?, In: Journal of Statistics Education, Volume 19, Number 2

[3] HEYWOOD J. B. (1988). Internal Combustion Engines Fundamentals, McGraw-Hill, ISBN 0-07-028637-X

[4] PÁV K. (2016). Adaptivní model hoření homogenní směsi ve válci zážehového spalovacího motoru, Habilitation Thesis, Liberec

[5] PÁV K. (2016). Adaptive Combustion Model for SI Engines, In: XLVII. International Scientific Conference of Czech and Slovak University Departments and Institutions Dealing with the Research of Combustion Engines, Brno, pp. 149–156, ISBN 978-80-214-5379-1

[6] PÁV K. (2017). Simulace pracovního oběhu 4T, Calculation Software – Microsoft Excel

[7] PISCHINGER R. (2002). Engine Indicating, User Handbook, AVL Graz

[8] POETSCH C., SCHUEMIE H., OFNER H., TATSCHL R., VITEK O. (2013). A Computational Study on the Impact of Cycle-to-Cycle Combustion Fluctuations on Fuel Consumption and Knock in Steady-State and Drivecycle Operation, SAE Technical Paper 2013-24-0030, doi:10.4271/2013-24-0030

[9] SCHNEIDER A., HETTINGER A., SCHÜNEMANN E. (2016). Optical Investigations of Flame Kernel Formation in an SI Engine with Diluted Mixture, In: 12th International Symposium on Combustion Diagnostics, Baden-Baden, pp. 61-79, ISBN 978-3-9816971-2-4

[10] TATSCHL R., BOGENSPERGER M., PAVLOVIC Z., PRIESCHING P., SCHUEMIE H., VITEK O., MACEK, J. (2013). LES Simulation of Flame Propagation in a Direct-Injection SI-Engine to Identify the Causes of Cycle-to-Cycle Combustion Variations, SAE Technical Paper 2013-01-1084, doi:10.4271/2013-01-1084

[11] VITEK O., MACEK J., POETSCH C., TATSCHL R. (2013). Modeling Cycle-to-Cycle Variations in 0-D/1-D Simulation by Means of Combustion Model Parameter Perturbations based on Statistics of Cycle-Resolved Data, SAE Technical Paper 2013-01-1314, doi:10.4271/2013-01-1314

DE GRUYTER OPEN

10.1515/mecdc-2018-0003

IDENTIFICATION OF CYCLE-TO-CYCLE VARIABILITY SOURCES IN SI ICE BASED ON CFD MODELING

OLDŘICH VÍTEK, VÍT DOLEČEK, ZBYNĚK SYROVÁTKA, JAN MACEK

Czech Technical University in Prague, Department of Automotive, Combustion Engine and Railway Engineering
Technická 4, CZ-16607 Prague 6, Czech Republic, Tel.: +420224352507, Fax: +420224352500
Email: oldrich.vitek@fs.cvut.cz, v.dolecek@fs.cvut.cz, zbynek.syrovatka@fs.cvut.cz, jan.macek@fs.cvut.cz

ABSTRACT

The presented paper deals with modelling of cycle-to-cycle variations (CCV) in SI ICEs by means of 3-D CFD LES approach. The main goals are the following: to identify the most important sources of CCV and to compare 2 different ignition systems: classical spark ignition and turbulent flame jet. Calibrated 3-D CFD LES models of these engines are applied to perform time-demanding multi-cycle calculations of selected engine operating points. The simulation data are analyzed including comparison with experimental data and main conclusions are drawn. The turbulence, which is generated during intake stroke, is identified as the main CCV source while early flame kernel development (strongly influenced by local turbulence) is also important.

KEYWORDS: LARGE EDDY SIMULATION (LES), CFD, SI ICE, CYCLE-TO-CYCLE VARIATION (CCV), MULTI-CYCLE CALCULATIONS

SHRNUTÍ

Tento článek se zabývá modelováním mezicyklové variability v zážehových spalovacích motorech pomocí 3-D CFD LES přístupu. Hlavní cíle práce jsou následující: identifikace hlavních zdrojů mezicyklové variability a porovnání 2 různých systémů pro zapálení směsi: klasický zážeh pomocí svíčky a turbulentní hořící paprsek. Kalibrované 3-D CFD LES modely těchto motorů jsou použity pro časově náročné simulace mnoha po sobě následujících cyklů pro vybrané pracovní body těchto motorů. Data ze simulací jsou analyzována včetně srovnání s experimenty a jsou formulovány hlavní závěry. Turbulence, která je primárně generována během sacího zdvihu, je identifikována jako hlavní zdroj mezicyklové variability, zatímco co úvodní fáze vývinu jádra plemene (silně ovlivněna lokální turbulencí) je taky důležitá.

KLÍČOVÁ SLOVA: SIMULACE VELKÝCH VÍRŮ (LES), CFD, ZÁŽEHOVÝ SPALOVACÍ MOTOR, MEZICYKLOVÁ VARIABILITA, SIMULACE MNOHA PO SOBĚ JDOUCÍCH CYKLŮ

1. INTRODUCTION

The operation of SI-engines is characterized by a non-repeatability of the instantaneous combustion rate of the individual engine cycles at nominally identical engine operating parameters. This phenomenon, usually referred to as cycle-to-cycle variations (CCV), strongly limits the SI-engine thermal efficiency by determining the maximum possible compression ratio and spark advance for knock-free combustion. Due to the presence of CCV, both the maximum compression ratio and spark advance is limited by the fastest burning cycle that is most prone to the onset of knock in the end-gas ahead of the flame. Hence, minimizing the cyclic dispersion of the in-cylinder combustion process for a given engine configuration offers the potential to increase engine compression ratio and to adopt the thermodynamically most efficient spark advance and consequently to reduce the specific fuel consumption for a given power output.

A major prerequisite for the development of strategies for minimizing cycle-to-cycle combustion variations is a detailed understanding of the causes leading to the cyclic dispersion of the combustion process from one cycle to the other. Conventional cylinder pressure indication clearly provides information on the appearance of cycle-to-cycle combustion variations and also enables a quantification of the in-cylinder pressure evolution variations from one cycle to the other. However, in order to identify the origins of the cycle-to-cycle combustion variations, a detailed cycle-resolved insight into the locally governing in-cylinder flow, mixture formation and flame propagation processes including their complex mutual interactions is

required. Experimental studies allow identifying cycle-to-cycle variations for a given engine, but they are only applicable once the engine is available in hardware, i.e. in a phase of the engine development process in which modifications of the initial design are difficult to realize due to cost and time constraints.

In the above context and in view of the more and more stringent legislative demands on fuel consumption and hence CO2 emissions, it becomes increasingly desirable to be able to predict and control individual engine cycles, and thus to address the occurrence and the impact of CCV on fuel consumption. Moreover, the ability to predict CCV in the early engine design phase is essential to exploit the full potential of promising new SI-engine technologies, such as e.g. direct-injection, downsizing, charging, etc. under real operation.

Based on above-mentioned, the main target of the presented work is to identify the main sources of cyclic variation of SI ICE operation. The other one is to compare 2 different engine cases in terms of ignition device: classical spark ignition ICE and scavenged pre-chamber gas ICE (based on [19], this engine configuration can be considered as turbulent flame jet with respect to mixture ignition process). The main tool to achieve these goals is to apply LES CFD simulation approach, which has proved to be a very efficient one when dealing with CCV phenomena in SI ICE – c.f. [1, 2, 3, 4, 5, 6, 9, 13].

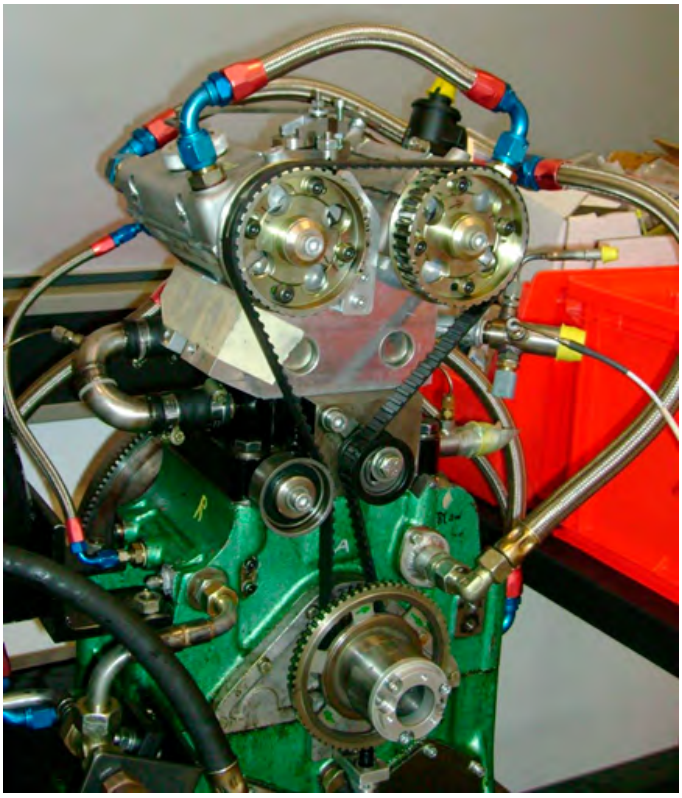

FIGURE 1: Target engine A – AVL Single Cylinder Research Engine (SI version).
OBRÁZEK 1: Cílový motor A – zkušební jednoválec od AVL (zážehová varianta).

2. MATHEMATICAL MODEL

For the simulation of the gas flow, spray mixture formation and flame propagation processes in the SI-engine analyzed in the present work, the 3D-CFD code AVL FIRE is adopted [22]. The 3-D CFD SW solves the general conservation equations of mass, momentum and enthalpy plus additional transport equations for turbulence related quantities and for conservation of chemical species. Depending on the physical and chemical sub-models employed, additional scalar quantities, such as e.g. mixture fraction, reaction progress variable, flame surface density, etc. are solved as well.

The adopted solution method is based on a fully conservative finite volume approach. All dependent variables, such as momentum, pressure, density, turbulence kinetic energy, dissipation rate, and the scalar quantities are evaluated at the cell centres of the general, unstructured computational grids. A second-order midpoint rule is used for integral approximation and a second order linear approximation for any value at the cell-face. Convection is solved by adopting higher order differencing schemes. In order to offer full flexibility in terms of the structure and topology of the employed computational meshes, the solver allows for each computational cell to consist of an arbitrary number of cell faces. Connectivity and interpolation practices for gradients and cell-face values are set up to accommodate such 'polyhedral' calculation volumes. The rate of change (accumulation term) is discretized by using an Euler implicit scheme. The overall solution procedure is iterative and is based on the Semi-Implicit Method for Pressure-Linked Equations algorithm (SIMPLE) or Pressure-Implicit with Splitting of Operators (PISO, c.f. [8]), applicable to turbulent flows at all speeds. For solving the large sets of linear equation systems evolving from the discretization of the governing equations, an efficient preconditioned conjugate gradient method is employed. More details can be found in [5, 6] and documentation of AVL FIRE [22].

Dealing with numerical setup, the following settings were applied. PISO algorithm was selected as time integration method while 2nd order schemes were used for convective term approximations. Time step was set to 0.1 degCA.

Regarding turbulence modelling, Large Eddy Simulation (LES) was adopted. It is based on the filtered instantaneous Navier-Stokes equations. Filtering operation actually represents scale separation in space, where large scales are directly resolved, and the influence of small scales is taken into account by the sub-grid scale (SGS) model. Smagorinsky SGS model [9, 10] was applied for the Engine A while coherent structure version of LES approach [9, 11, 12] was selected for the case of the Engine B.

Concerning combustion models, the LES version of ECFM-3Z was activated due to positive experience with this model from the past – c.f. [5, 6]. Premixed turbulent SI-engine combustion is modeled in the present case by using the LES variant of the Extended Coherent Flame Model (CFM) [13] which is based on solving a transport equation for the flame surface density (FSD), suitably linked with the gas-phase thermochemistry. It should be stressed that this model is turbulence driven, hence it cannot capture local chemical effects (e.g., flame quenching due to low temperature or turbulence-related effects) – this leads to a statement that all fuel is (usually) burnt when using this model (provided there is enough oxygen). Dealing with applied chemistry, the turbulence driven combustion models are usually linked with simplified chemistry approaches based on equilibrium. This was also the case for the presented CFD calculations. The only considered pollutant was NOx, however its formation was based on standard approach [14], which is to solve certain equations of chemical kinetics.

The spray model adopted in the present study is based on the Lagrangian Discrete Droplet Method (DDM) [15]. In the DDM the continuous gaseous phase is described by the standard Eulerian conservation equations, whereas the transport of the dispersed phase is calculated by tracking the trajectories of representative droplet parcels. A parcel consists of a number of droplets, with all the droplets having identical physical properties and behaving equally when they move, break up, hit a wall or evaporate. The calculation of the parcel movement is done with a sub-cycling procedure between the gas phase time steps taking into account the forces exerted on the parcels by the gas phase as well as the related heat and mass transfer. The coupling between the liquid and the gaseous phases is achieved by source term exchange for mass, momentum, energy and turbulence. For the LES application, turbulent dispersion effects are assumed to be fully covered by the interaction of the droplets with the resolved LES flow field scales – hence, this term is deactivated when LES approach is applied.

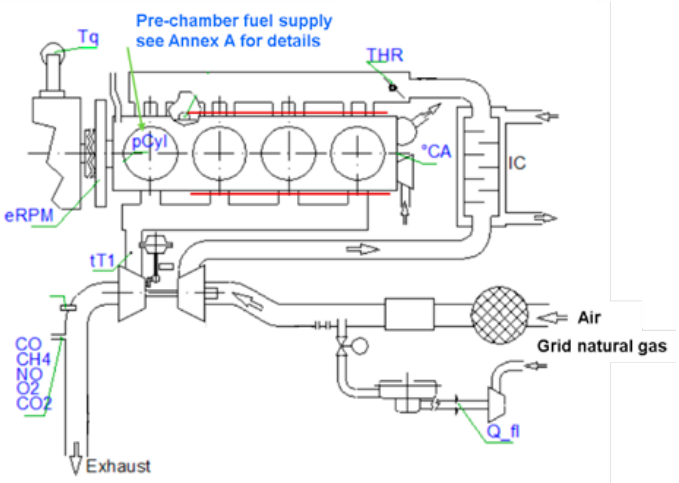

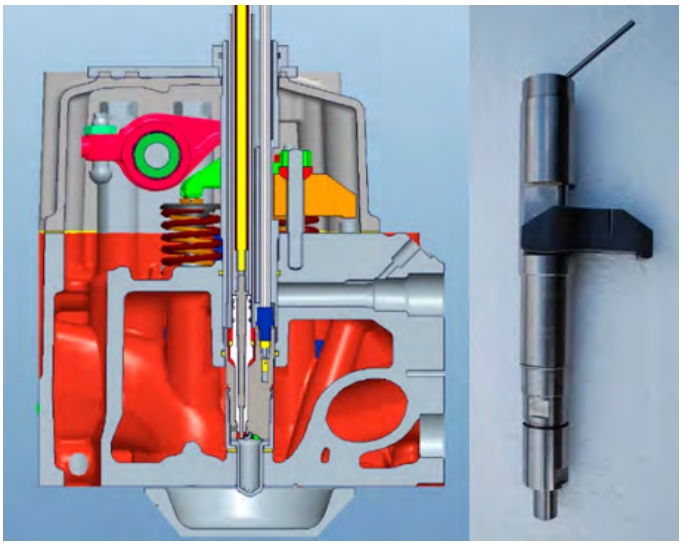

FIGURE 2: Target engine B – research engine with scavenged pre-chamber (CNG SI version).
OBRÁZEK 2: Cílový motor B – zkušební motor s vyplachovanou komůrkou (plynová zážehová varianta).

TABLE 1: Main engine parameters – version A and version B.
TABULKA 1: Hlavní parametry motoru – verze A a verze B.

Engine Parameter	Unit	Engine A	Engine B
Bore	[mm]	86	102
Stroke	[mm]	86	120
Compression Ratio	[1]	11.5	12
Charging		Naturally Aspirated	Turbocharged
Fuel		Gasoline (ON 95)	Methane
Fuel Injection		DI	PFI + pre-chamber
Number of Intake Valves		2 (phasing)	2
Number of Exhaust Valves		2 (phasing)	2

TABLE 2: Main mesh parameters for both engine version (A and B).
TABULKA 2: Hlavní parametry sítě pro obě verze motoru (A a B).

Parameter	Unit	Engine A	Engine B
Typical Mesh Size	[mm]	<1.0	<0.6
Min. Amount of Mesh Cells	[1]	1.7M	7.5M
Max. Amount of Mesh Cells	[1]	3.3M	13M
Max. Angle Interval of Single Mesh Set	[degCA]	5	10

The CFD models are based on 2 existing engine geometries (c.f. Table 1, Figure 1 and 2). 3-D CAD data of engine cylinder head, piston and liner (for both engine variants) were provided by engine manufacturers. All the necessary geometry information was available, hence the meshing procedure could be started. The meshing itself was made by means of hybrid meshing tool of AVL FIRE. Typical mesh cell size was set to 1.0 mm (the Engine A) and 0.6 mm (the Engine B) – this is based on experience from the previous work [5, 6] with LES approach to SI ICE modeling. The important parameters of applied meshes are summarized in Table 2.

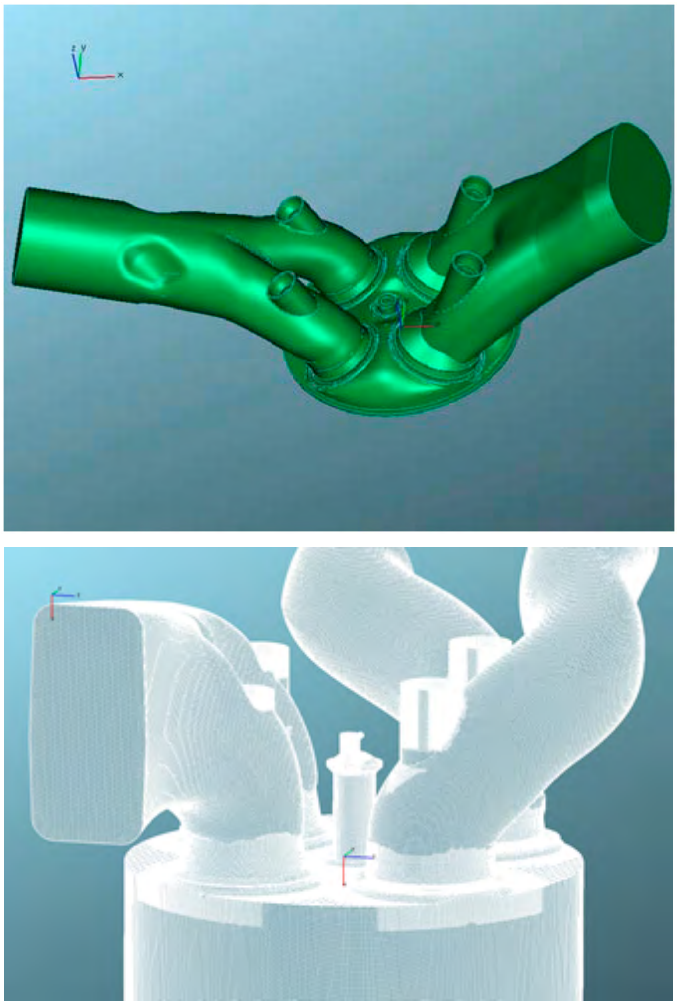

FIGURE 3: 3-D CAD geometries of considered engine cases (Table 1 and 2) – the Engine A (upper subfigure) and the Engine B (lower subfigure).
OBRÁZEK 3: 3-D CAD geometrie uvažovaných motorů (tabulky 1 a 2) – varianta A (horní obrázek) a variant B (dolní obrázek).

Concerning boundary and initial conditions, they were transferred from the calibrated 0-D/1-D models of the engines created in SW tools [23, 24]. To be more precise, 0-D/1-D tool [23] and 3-D CFD [22] tool were directly linked to perform fully coupled co-simulation for the case of the Engine A (c.f. Table 1) – hence, boundary conditions were provided directly by 0-D/1-D tool. For the case of the Engine B, surface temperatures were based on simplified predictive FEM model, inlet/outlet boundary pressure/temperature was imposed as function of crank angle. The same applies to fuel mass-flow rate to the pre-chamber, which represents mixture enrichment via dedicated fuel supply system. Initial values of all required thermodynamic parameters (including composition) were directly transferred from the 0-D/1-D model.

3. COMPUTED CASES

As it is mentioned above, 2 engine cases were considered (Table 1). The Engine A represents research single-cylinder DI SI ICE while the Engine B corresponds to experimental CNG SI ICE with scavenged pre-chamber. Moreover, the Engine B was heavily modified from its original version, which represents a light-duty CI ICE – hence, it is dominated by swirling in-cylinder motion while there is a significant bowl in the piston (c.f. Figure 3, lower subfigure). On the other hand, the Engine A is dominated by tumbling in-cylinder flow (c.f. Figure 3, upper subfigure). Moreover, the Engine A is equipped with direct fuel injection system – the injector is located just below intake ports ('side-mounted' configuration) and it is pointing in the same direction as a tumbling motion (created by appropriate direction of intake ports), hence supporting the in-cylinder tumble. The injection starts at early intake stroke and it takes approx. 40 degCA for considered low-IMEP cases (c.f. Table 3). The range of operating conditions related to data presented in the paper of both considered engines are summarized in Table 3. As the focus is put on CCV effects, relatively low load cases were selected to avoid knock occurrence.

TABLE 3: Considered operating conditions for both engine version (A and B).
TABULKA 3: Uvažované pracovní podmínky pro obě verze motoru (A a B).

Parameter	Unit	Engine A	Engine B
Engine Speed	[rpm]	2000 – 3000	1800
IMEP	[bar]	2.0 – 3.0	5 – 9
Air Excess	[1]	1.0 – 1.3	1.0 – 1.9
Residual Gas Content	[%]	10 – 30	< 10

Regarding the Engine A, the following operating conditions were considered: motored regimes (at different engine speeds) and combustion regimes (2 operating points at low IMEP level). Many consecutive cycles (at least 30) were calculated to obtain statistical convergence of important output parameters. More detailed information about the Engine A can be found in [5, 6, 7].

Dealing with the Engine B, 3 different operating points were considered – these differ in air excess (un-throttled operation) ranging between 1.0 and 1.9 while engine speed was kept constant. Due to much more time demanding calculations (c.f. mesh parameters in Table 2), only 5 consecutive engine cycles were calculated. However, this should provide a good estimate of statistical moments of the 1st order (e.g., average values of scalar properties) – this observation is based on results from EU FP7 project LESSCCV, c.f. [7, 5]. More detailed information about the Engine B can be found in [16, 17].

There is additional significant difference between those selected engine cases – the Engine A represents a modern automotive SI DI ICE dominated by tumble while using classical ignition device (spark plug). On the other hand, the Engine B corresponds to gas SI ICE dominated by swirl, which is equipped with scavenged pre-chamber to be able to ignite very lean mixtures (hence, a turbulent flame jet ignition device is applied). The combustion process of the Engine A is a classical turbulent deflagration flame which has approximately spherical shape. Even though the combustion process in the Engine B is also a turbulent deflagration flame, its shape is dominated by turbulent flame jet shape, hence it is (in terms of its shape and time evolution) similar to combustion in CI (diesel) ICE.

4. MODEL CALIBRATION

Every calibration process requires reference data. In this case, these data were represented by experimental data typically measured at ICE test beds. This mainly includes in-cylinder pressure. Typically, more than 100 consecutive cycles (for each operating point) were measured and processed, hence both average cycle data and all individual cycle data were available. When calibrating 0-D/1-D models created in the tools [23, 24], much more information was needed. However, when calibrating 3-D CFD models, in-cylinder pressure traces were sufficient. If any additional information was needed, it was transferred from the calibrated 0-D/1-D models (representing the 'system level' thermodynamic models) of the target engines.

Every model needs a calibration to match experimental data – this also applies to 3-D CFD modelling as well. However, the amount of model constants to be tuned is limited as these kinds of models are supposed to have high predictive ability, hence less tuning is necessary. In the above-mentioned case of LES ECFM-3Z model, there are 2 constants to be tuned: stretch factor and initial flame surfaces density (c.f. [22] for more details). The latter one (initial flame surface density) has relatively low influence and it is also related to initial parameters of flame kernel to be imposed to start the flame propagation process. On the other hand, the influence of stretch factor is very strong as it is shown in Figure 4. This parameter directly influences the speed in which the flame propagates, hence the higher the value, the faster the combustion process. In the presented cases (the Engine A and the Engine B – c.f. Table 1 and 2), the value of stretch factor was adjusted to match experimental data (pressure traces) for a selected operating conditions (e.g., engine speed and load). After that, it was fixed and kept constant for any other operating conditions of the selected engine case. Hence, the value is supposed to be engine specific. The value of initial flame surface density was estimated using recommended values from manual documentation of [22]. There is still one parameter to be adjusted, namely the phasing of combustion. As the way to initiate the flame propagation process is a bit artificial (prescribing flame kernel of certain size for certain time), the time does not correspond to a real ignition event. The empirical experience shows that flame initialization has to be timed few degrees of crank angle before the real ignition event. This timing adjustment has to be done for every engine operating point. On the other hand, both the stretch factor and the initial flame surface density are constant regardless of engine speed and/or load.

The quality of calibration process can be observed in Figure 9 for the Engine A and Figure 11 for the Engine B. Especially in the case of the Engine B the prediction is very good terms of combustion duration and CCV effects. In the case of the Engine A, there is good correspondence in terms of combustion duration, however CCV effects are a bit under-predicted. It should be stressed that even though both engine cases correspond to SI ICE concept, there is a fundamental difference between these engines in terms of flame topology. In the case of the Engine A, it is a classical SI ICE spherical flame (c.f. Figure 7). On the other hand, the Engine B is equipped with scavenged pre-chamber (it is a turbulent flame jet in terms of ignition device definition), which leads to very different flame

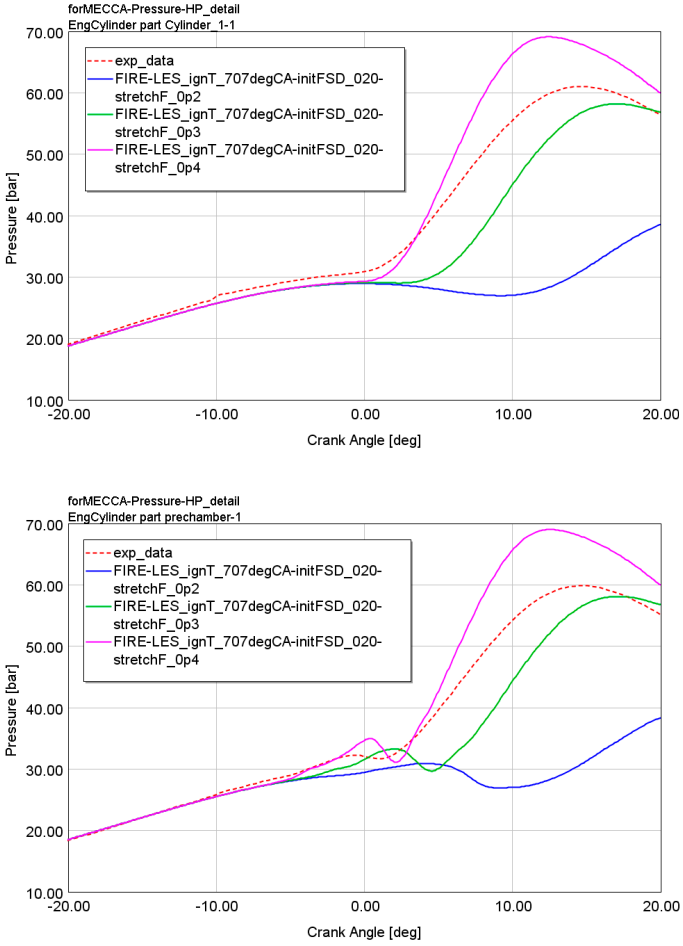

FIGURE 4: Tuning of combustion model (the Engine B – c.f. Table 1 and 2) – the influence of the stretch factor (LES ECFM-3Z model; blue curve represents the value of stretch factor of 0.2, green one of 0.3 and purple one of 0.4) – in-cylinder pressure is plotted in upper subfigure while pre-chamber pressure is shown in lower subfigure.
OBRÁZEK 4: Kalibrace modelu spalování (motor verze B – více v tabulkách 1 a 2) – vliv parametru „stretch factor" (LES ECFM-3Z; modrá křivka odpovídá hodnotě „strech factor" 0.2, zelená 0.3 a fialová 0.4) – horní obrázek zobrazuje tlak ve válci, zatímco dolní obrázek ukazuje tlak v komůrce.

structure – it is similar to diesel engines when observing the shape of burnt/unburnt zone (c.f. Figure 14). However, it is deflagration flame in both engine cases.

5. DISCUSSION OF RESULTS

As it is mentioned above, the main focus of the paper is to study CCV effects by means of detailed 3-D CFD LES simulation approach. Two different engine cases were selected – the first one corresponds to a classical automotive direct injection SI ICE while the second one represents a scavenged pre-chamber concept applied to gas SI ICE. Many CFD data were obtained within past years dealing with these engine cases. The most relevant results in terms of CCV are presented in this section.

Strongly turbulent in-cylinder flow structure is shown in Figure 5 – the turbulence is generated during intake stroke while it decays during compression stroke. There are many parameters influencing this complex process – engine speed or intake valve timing are among the most important ones. These are well-known facts – c.f. [19]. Early flame kernel development is a critical phase of combustion process influencing subsequent phase of classical deflagration flame development. Even motored regimes show relatively strong CCV effects, which also applies to spark plug location – c.f. Figure 6. While average velocity strongly decreases during compression stroke, fluctuation component of velocity vector has relatively high peak just before TDC – this peak is positioned just in the typical window of ignition event. Hence, early flame kernel development is strongly influenced by that phenomenon, which subsequently influences both flame shape and its propagation – this is clearly seen in Figure 7. It seems that there is a correlation between resolved fluctuation kinetic energy (RFKE – the definition is presented in [21]; simply speaking, it is a difference between average total kinetic energy and kinetic energy based on average velocity vector – hence it represents the average value of kinetic energy of fluctuation velocity vector; however, this property consists of 2 major parts – turbulence and cycle-to-cycle variations; for low CCV cases, the latter one is usually neglected) peak at spark plug location (near TDC) and level of CCV – if the peak is significantly higher, early flame kernel development shows higher level of CCV which leads to high CCV of the whole combustion phase. Additional information about the term RFKE is presented in detail in paper [5] including its pattern for different cases.

Data presented in Figure 6, which represents motored operation of ICE, clearly indicate that main phenomenon behind CCV is the turbulent nature of the flow itself. The strong variability of velocity vector is mainly the outcome of intake stroke when strong tumble vortex is created. This large-scale structure is deformed (compressed) during the compression stroke. This leads to increase of its angular velocity, which in turn increases all dissipative processes. Hence, strong turbulence is created. As intake stroke (i.e., tumble vortex formation) already features relatively high level of CCV – c.f. Figure 8, it can be expected that this trend is preserved during compression stroke. Due to non-linear effects related to strong tumble dissipation near TDC, there is a peak of velocity vector fluctuation component (Figure 6). As there is little difference between motored operation of ICE and combustion one in terms of both intake stroke and compression one, the above mentioned statements are generally valid. These effects are further magnified when combustion process is started – c.f. Figure 7. This is mainly related to the nature of turbulent deflagration flame – more details can be found in [19, 20].

Results concerning combustion operation are shown in Figure 7, 9 and 10 for the Engine A and in Figure 11 and 14 for the

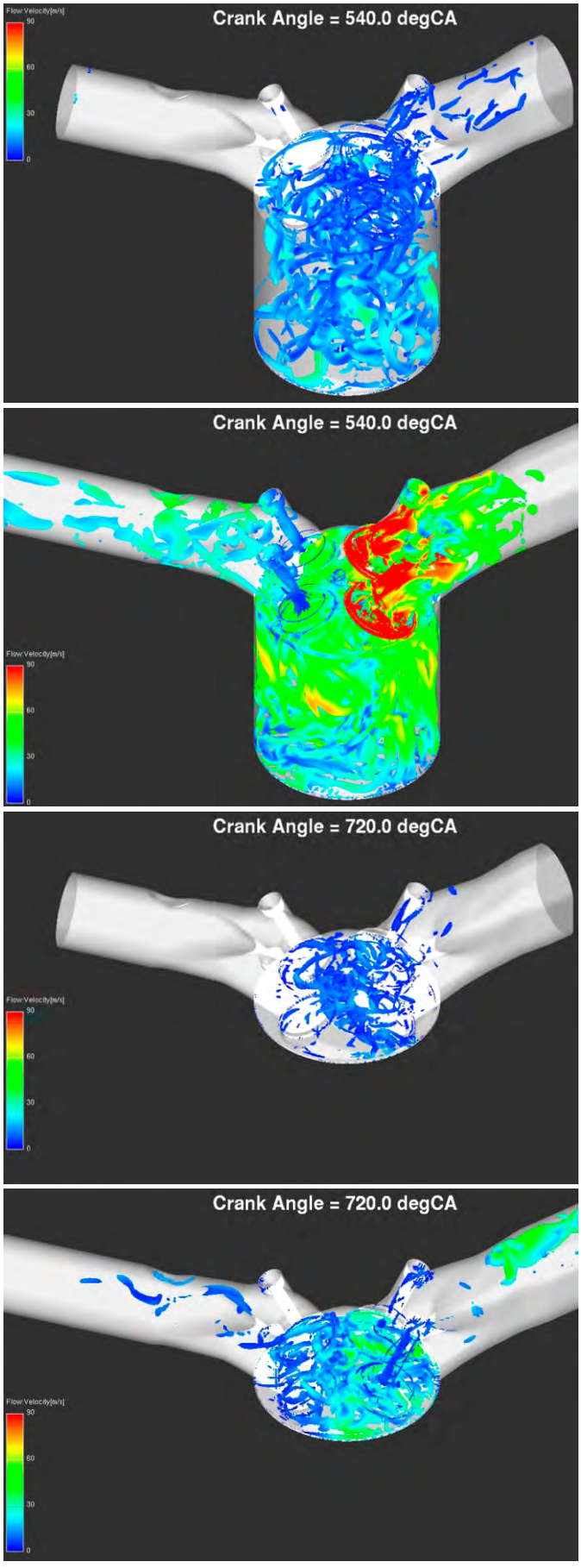

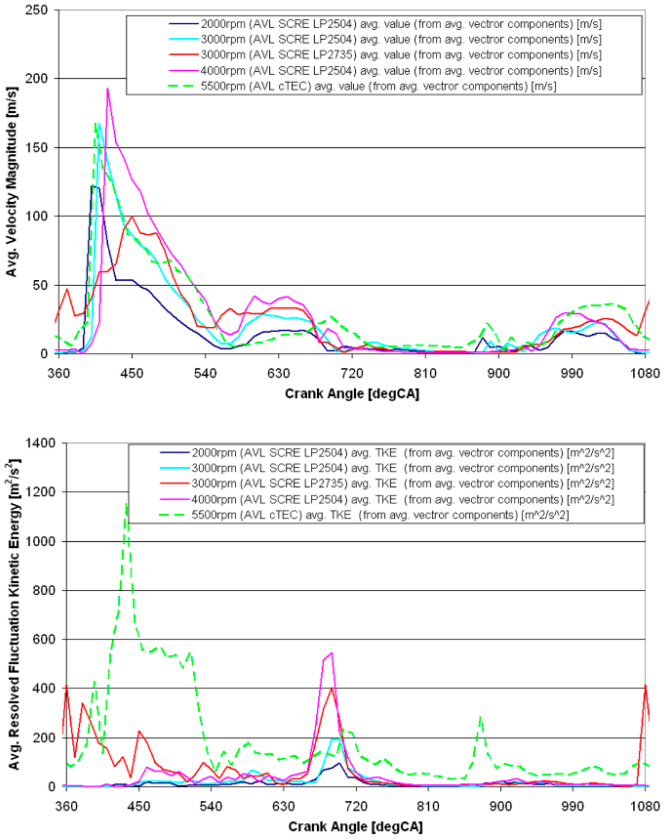

↑ **FIGURE 6:** Comparison of selected properties at spark plug location for different engine operating conditions (low CCV case, label 'LP2504' at 2000 rpm, is plotted in dark blue color; high CCV case, label 'LP2735' at 3000 rpm, is plotted in red color; more details can be found in [5, 6]) for motored regimes (engine speed is mentioned in figure legend; no throttling was applied) of the Engine A case (c.f. Table 1 and 2) – left subfigure represents magnitude of average velocity vector (based on more than 20 consecutive cycles) while right subfigure corresponds to resolved fluctuation kinetic energy.

OBRÁZEK 6: Porovnání vybraných veličin v místě svíčky pro různé pracovní body (bod s nízkou mezicyklovou variabilitou, označení „LP2504" při 2000 otáčkách, je zobrazen tmavě modrou barvou; bod s vysokou má barvu červenou, označení „LP2735" při 3000 otáčkách; více informací lze nalézt v [5, 6]) pro protáčené režimy motoru (otáčky motoru jsou zmíněny v legendě; bez škrcení) varianty A (více v tabulkách 1 a 2) – levý obrázek reprezentuje střední velikost vektoru rychlosti (založeno na minimálně 20 po sobě jdoucích cyklech), zatímco pravý obrázek odpovídá výpočtem zachycené kinetické energii fluktuací.

← **FIGURE 5:** Comparison of low CCV engine operating conditions (left column) and high CCV ones (right column) at different crank train positions (top row: BTD, bottom row: TDC) for the Engine A case (c.f. Table 1 and 2) – iso-surface of constant Q-invariant; the property mapped on the iso-surface is velocity vector magnitude (red color corresponds to 90 m/s; blue one represents 0 m/s).

OBRÁZEK 5: Porovnání pracovního bodu s nízkou mezicyklovou variabilitou (levý sloupec) a vysokou (pravý sloupec) v různých polohách klikového mechanismu (horní řádek: dolní úvrať, dolní řádek: horní úvrať) pro motor varianty A (více v tabulkách 1 a 2) – izoplocha konstantní hodnoty Q-invatriantu; barva odpovídá hodnotě velikosti vektoru rychlosti (červená barva odpovídá 90 m/s, modrá 0 m/s).

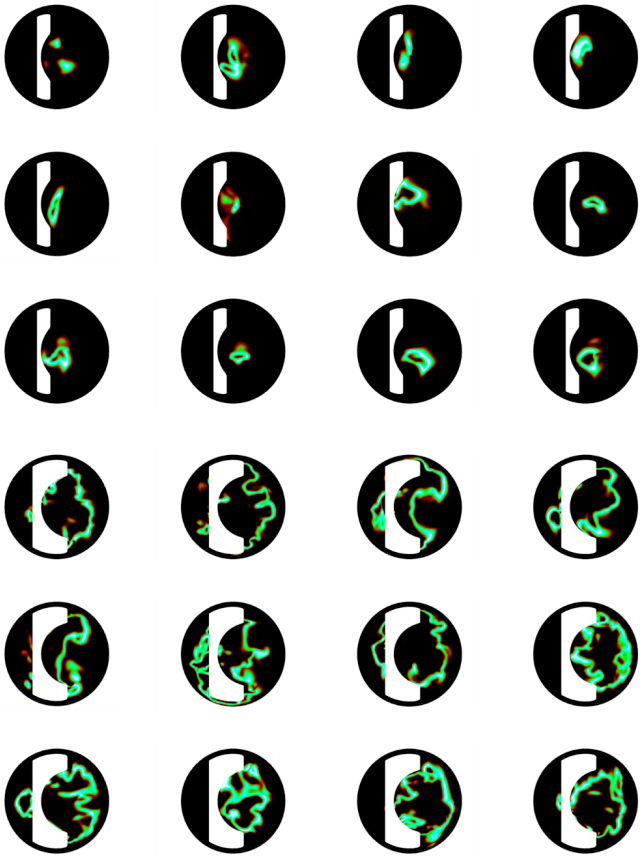

FIGURE 7: Flame front position (12 consecutive cycles are shown) for high CCV operating conditions at different combustion phases for the case of the Engine A (c.f. Table 1 and 2), top view – top subfigure (consisting of 12 sub-subfigures) corresponds to early combustion phase while bottom one (again consisting of 12 sub-subfigures) represents main combustion phase (rapid burning phase); green color represents burning zone.
OBRÁZEK 7: Poloha fronty plamene (zobrazeno je 12 po sobě následujících cyklů) pro pracovní bod s vysokou mezicyklovou variabilitou během různých fází hoření pro motor varianty A (více v tabulkách 1 a 2), pohled shora – horní obrázek (skládající se z 12 dalších obrázků) odpovídá úvodní fázi spalování, zatímco dolní (opět skládající se z 12 dalších obrázků) reprezentuje hlavní fázi hoření; zelená barva odpovídá hořící zóně.

Engine B. Regarding the pressure traces of the Engine A case (Figure 9), the influence of very early combustion phase (flame kernel development) can be quantified. The left subfigure of Figure 9 corresponds to setting when flame initialization was kept constant – hence, only turbulence effects are responsible for CCV of pressure traces. It can be seen that scatter of pressure traces is relatively low when compared with experimental data. The right subfigure represents setting when certain level of flame initialization variation was imposed (the value of initial flame surface density was randomly varied within certain interval, which was estimated by experts from AVL). It can be observed that CCV of pressure traces was increased and there is a better correspondence between prediction and experimental data. Hence, it confirms that there is a significant influence of early flame kernel development on combustion process and that early flame kernel development features CCV effects as well – it is assumed that this is a consequence of local thermodynamic properties at spark plug, which vary strongly (c.f. Figure 6). These results are in-line with conclusions from [18], which are based on statistical analysis of experimental data and simulations based on 0-D/1-D approach.

Figure 10 shows CCV effects of ROHR (left subfigure) and global (in-cylinder average) air excess (right subfigure). Engine is operated in slightly lean conditions for this case. Significant variation of both ROHR and global air excess can be observed. Strong air excess variations are mainly due to high valve overlap, hence there is high internal EGR which varies a lot among cycles – that is why air excess is also varied strongly. It can be shown that in-cylinder flow during intake stroke (in terms of total fresh mixture in-flow) is almost constant for all the cycles, hence it is not the main source of air excess CCV. More information can be found in [5, 6].

On the other hand, combustion in the Engine B is different – based on [19], its ignition system can be labelled as turbulent flame jet, which can be clearly seen in Figure 14. Even though it is SI engine dominated by deflagration flame propagation, the flame topology is different when compared with classical spherical flame of SI ICE (compare Figure 7 with Figure 14). Regarding CCV effects, the prediction matches experimental data well – c.f. Figure 11 – without a need to impose variation of early flame kernel development phase. There are multiple reasons behind that statement. First, the mesh is significantly finer (c.f. Table 2), hence resolved turbulence is finer as well, which leads to lower requirement for additional modelling. Second, the combustion is mainly dominated by turbulent flame jet during early phase of in-cylinder combustion process – the jet is relatively strong, which leads to fast in-cylinder combustion. Third, the turbulent flame jet is primarily driven by pressure difference between pre-chamber and cylinder, which is relatively similar when comparing different engine cycles – it seems that this phenomenon leads to dampening of CCV effects taking place in pre-chamber. Based on all these facts, early flame kernel development phase (taking place in pre-chamber) seems to have a lower influence on CCV. Cyclic variation is mainly dominated by turbulent flame jet development – this also includes its timing, which is slightly different among the cycles due to different pre-chamber combustion duration (c.f. Figure 12 and Figure 13).

Combustion progress in a cylinder of the Engine B is shown in Figure 12. Unlike in the case of the Engine A (c.f. Figure 9), its shape seems to be similar for all calculated cycles while the main difference is combustion timing. Initial phase of in-cylinder combustion is primarily influenced by turbulent flame jet, the timing of which corresponds to combustion progress in a pre-chamber – in other words: in-cylinder combustion starts only

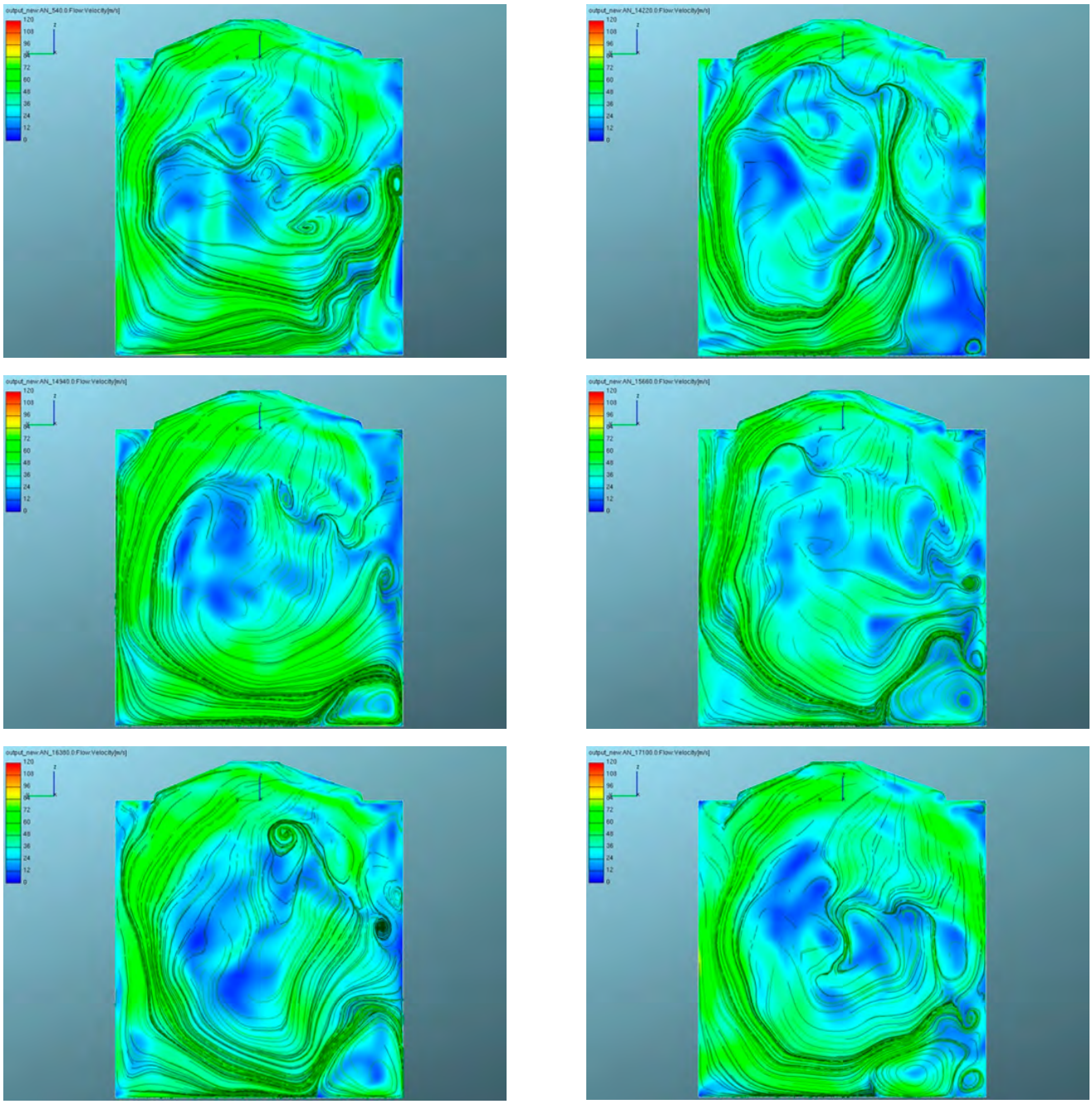

FIGURE 8: Tumble vortex structure at the end of intake stroke for the case of the Engine A (c.f. Table 1 and 2) – velocity vector magnitude is plotted (blue color represent the value of 0 m/s, red one corresponds to 120 m/s), black color curves represent streamlines; six consecutive engine cycles are shown.
OBRÁZEK 8: Struktura příčného víru (tumble) na konci sacího zdvihu pro motor varianty A (více v tabulkách 1 a 2) – je zobrazena velikost vektoru rychlosti (modrá barva reprezentuje 0 m/s, červená 120 m/s), černé křivky jsou proudnice; je zobrazeno 6 po sobě následujících cyklů.

when turbulent flame jet is initiated due to flame front reaching connecting channels between a pre-chamber and a cylinder. The early phase of in-cylinder combustion seems to be nearly identical in terms of rate of heat release (c.f. Figure 12) – up to approx. 30% of burnt fuel, the slope of ROHR curve (left subfigure in Figure 12) is almost the same for all calculated cycles. This suggests that early in-cylinder flame development, which is mainly dominated by turbulent flame jet, is little dependent on instantaneous local thermodynamic status in both pre-chamber and cylinder. Hence, any local differences due to CCV effects (when comparing different cycles) are suppressed. Any visible CCV effects (in terms of ROHR) are developed only at later phases of combustion process as turbulence needs some time to develop local differences, which lead to different rate of heat release.

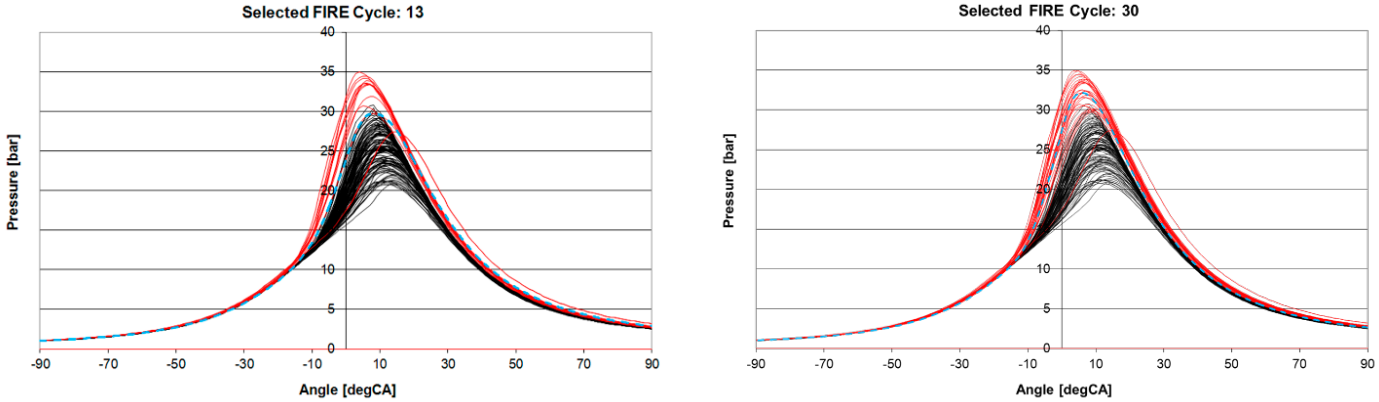

FIGURE 9: Comparison of individual cycle pressure traces between simulation (red color) and experimental data (black color) for high CCV operating conditions for the case of the Engine A (c.f. Table 1 and 2) – left subfigure corresponds to constant setting of ignition model while right subfigure represents a random variation of ignition model setting (initial value of Flame Surface Density of LES ECFM-3Z model).
OBRÁZEK 9: Porovnání tlaků ve válci pro jednotlivé cykly mezi simulací (červená barva) a experimentálními daty (černá barva) pro pracovní bod s vysokou mezicyklovou variabilitou pro motor varianty A (více v tabulkách 1 a 2) – levý obrázek odpovídá konstantnímu nastavení modelu pro zážeh, zatímco pravý obrázek reprezentuje náhodné variace modelu zážehu (počáteční hodnota pro FSD modelu LES ECFM-3Z).

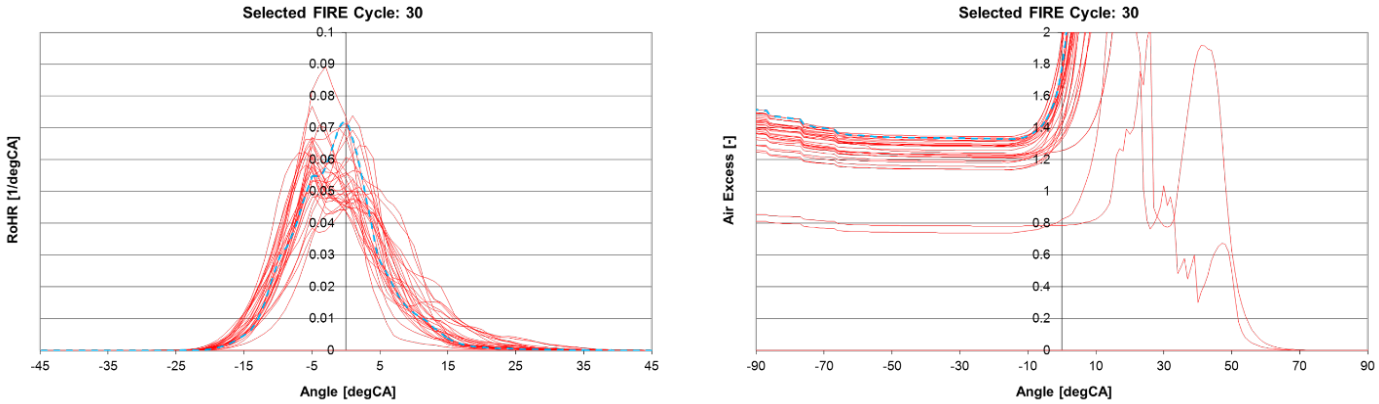

FIGURE 10: Comparison of individual cycle data from simulation for high CCV operating conditions for the case of the Engine A (c.f. Table 1 and 2) – left subfigure corresponds to normalized rate of heat release (ROHR) while right subfigure represents instantaneous mean in-cylinder air excess.
OBRÁZEK 10: Porovnání dat ze simulací pro jednotlivé cykly pro pracovní bod s vysokou mezicyklovou variabilitou pro motor varianty A (více v tabulkách 1 a 2) – levý obrázek odpovídá normalizované rychlosti vývinu tepla, zatímco pravý obrázek reprezentuje okamžitý střední přebytek vzduchu.

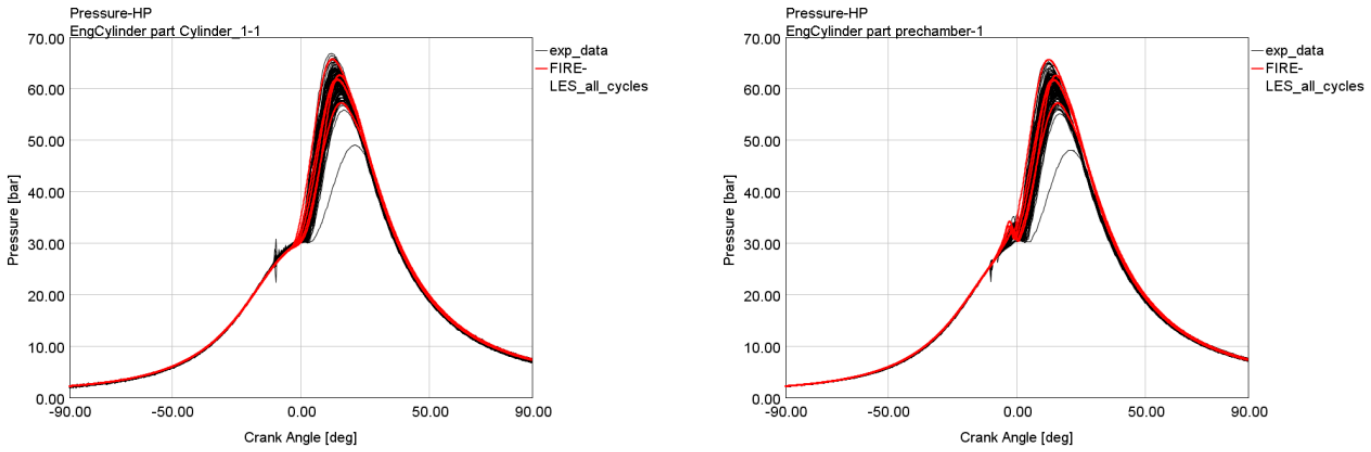

FIGURE 11: Comparison of individual cycle pressure traces between simulation (red color) and experimental data (black color) for the stoichiometric operation for the case of the Engine B (c.f. Table 1 and 2) – left subfigure corresponds to in-cylinder pressure while right subfigure represents pressure in pre-chamber.
OBRÁZEK 11: Porovnání tlaků ve válci/komůrce pro jednotlivé cykly mezi simulací (červená barva) a experimentálními daty (černá barva) pro pracovní bod se stechiometrickou směsí pro motor varianty B (více v tabulkách 1 a 2) – levý obrázek odpovídá tlaku ve válci, zatímco pravý obrázek reprezentuje tlak v komůrce.

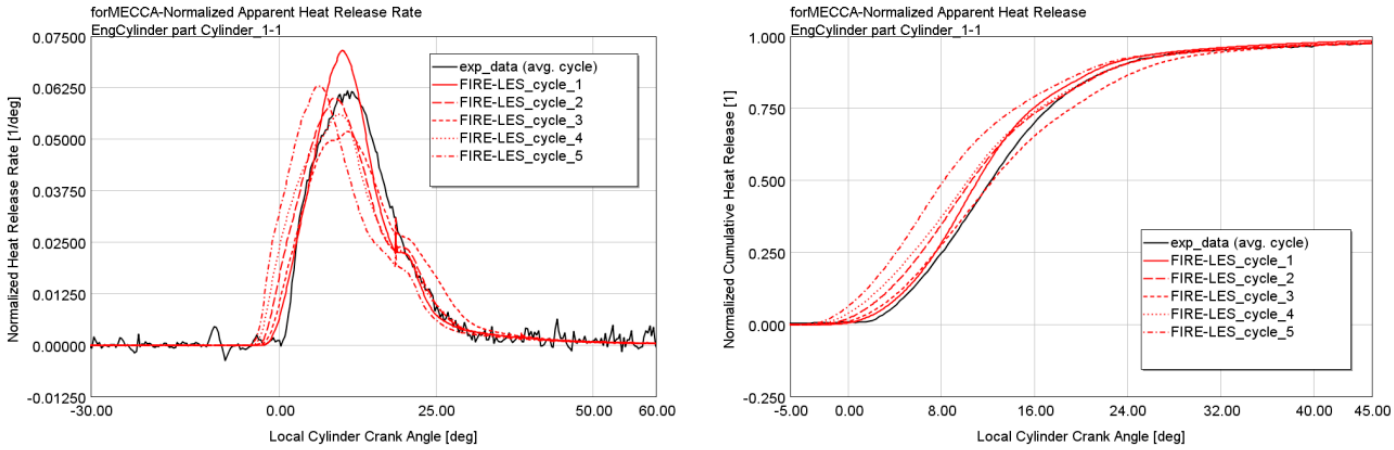

FIGURE 12: Comparison of individual cycle simulation data related to combustion (red color) and experimental data (black color; average cycle) for the stoichiometric operation for the case of the Engine B (c.f. Table 1 and 2) – left subfigure corresponds to normalized in-cylinder rate of heat release (ROHR) while right subfigure represents normalized in-cylinder heat release.

OBRÁZEK 12: Porovnání dat ze simulací pro jednotlivé cykly (červená barva) a experimentálních dat (černá barva; průměrný cyklus) pro pracovní bod se stechiometrickou směsí pro motor varianty B (více v tabulkách 1 a 2) – levý obrázek odpovídá normalizované rychlosti vývinu tepla ve válci, zatímco pravý obrázek reprezentuje normalizovaný vývin tepla ve válci.

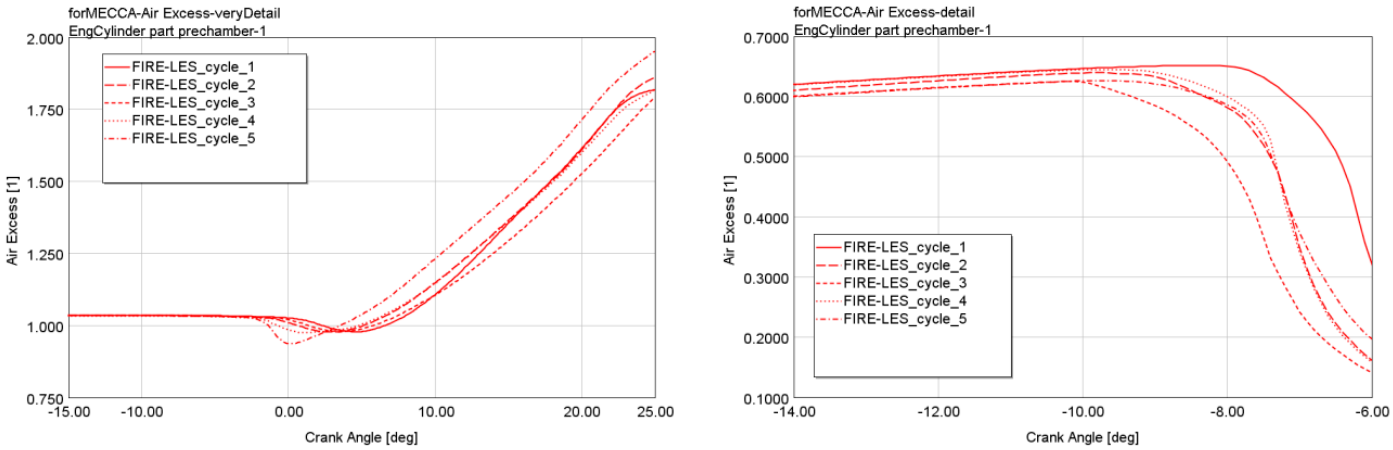

FIGURE 13: Comparison of individual cycle simulation data related to combustion (red color) for the stoichiometric operation for the case of the Engine B (c.f. Table 1 and 2) – left subfigure corresponds to mean in-cylinder air excess while right subfigure represents mean pre-chamber air excess (spark timing is set to -11 degCA).

OBRÁZEK 13: Porovnání dat ze simulací pro jednotlivé cykly (červená barva) pro pracovní bod se stechiometrickou směsí pro motor varianty B (více v tabulkách 1 a 2) – levý obrázek odpovídá prostorově střednímu přebytku vzduchu ve válci motoru, zatímco pravý obrázek reprezentuje střední přebytek vzduchu v komůrce (přeskok jiskry nastává při -11° pootočení klikového mechanismu).

The above mentioned phenomena are confirmed in Figure 13 – global mean air excess is shown for different cycles. There is relatively low CCV of pre-chamber mean air excess (right subfigure of Figure 13). However, visible start of pre-chamber combustion process (detected by strong decrease of mean air excess in Figure 13) varies within 3 degCA. It seems that pre-chamber flame front progress is similar for all calculated cycles, hence it reaches connecting channels at different crank angle positions (when comparing different engine cycles). Start of in-cylinder combustion is related to small decrease of mean in-cylinder air excess due to the fact that relatively high amount

FIGURE 14: Flame development in time domain for the case of the Engine B (c.f. Table 1 and 2) – fuel mass fraction is plotted (blue color represents burnt zone); top left subfigure corresponds to 716 degCA, all other sub-figures represent increase by 2 degCA (red color corresponds to 0.1 CH4 mass fraction; blue one represents 0).

OBRÁZEK 14: Postup plamene v čase pro motor varianty B (více v tabulkách 1 a 2) – je zobrazen hmotnostní podíl paliva (modrá barva reprezentuje spálenou zónu); levý horní obrázek odpovídá 716° natočení klikového hřídele, každý další obrázek reprezentuje nárůst o 2° (červená barva odpovídá 0.1 hmotnostního podílu CH4, modrá 0).

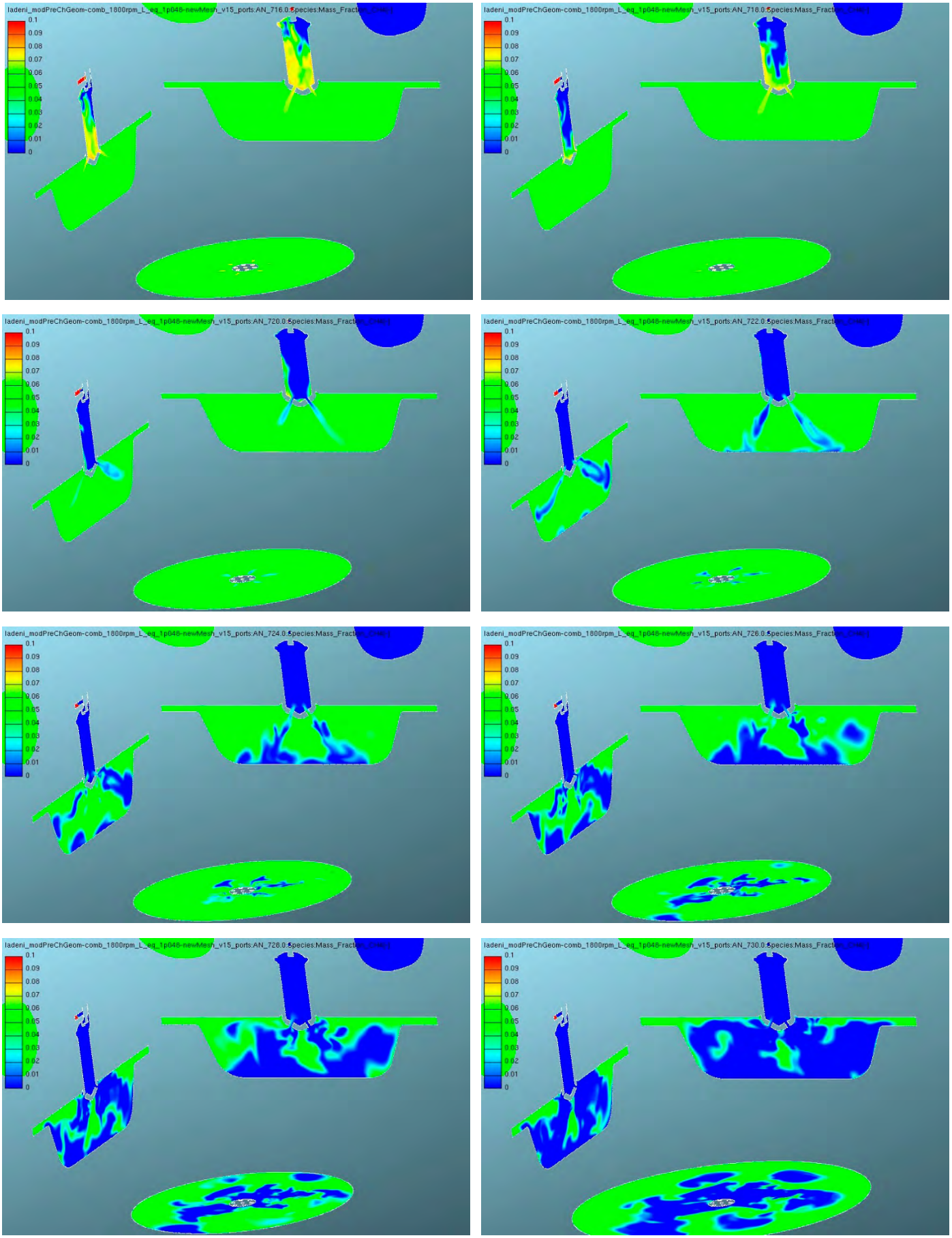
0.1
0.09
0.08
0.07
0.06
0.05
0.04
0.03
0.02
0.01
0

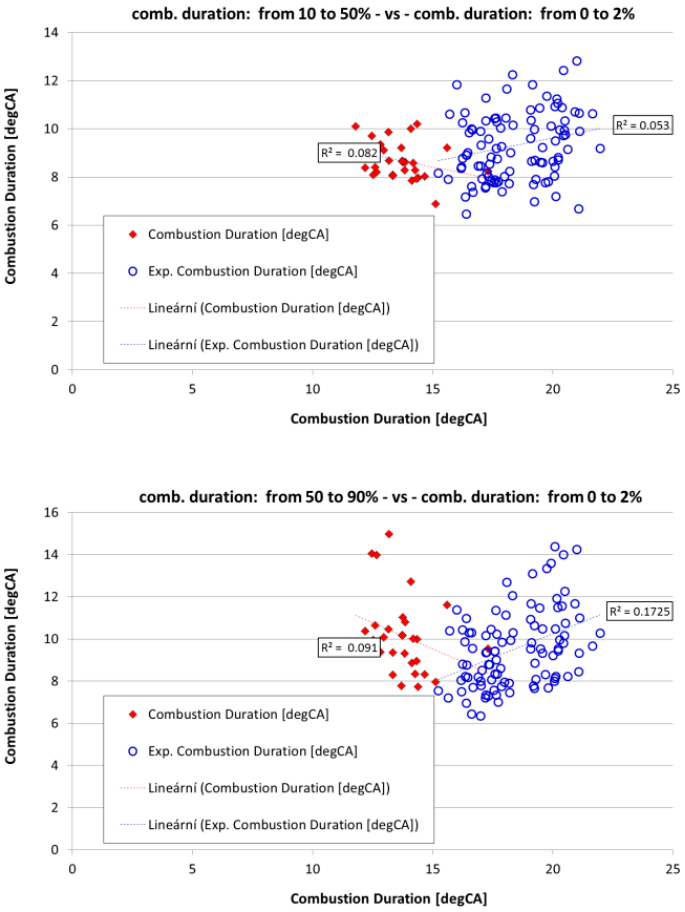

FIGURE 15: Comparison of individual cycle data between simulation (red color) and experimental data (blue color) for high CCV operating conditions for the case of the Engine A (c.f. Table 1 and 2) – left subfigure corresponds to correlation between early combustion phase duration (from 0 to 2% of burnt fuel) and first part of rapid combustion phase (from 10 to 50% of burnt fuel) while right subfigure represents correlation between early combustion phase duration and second part of rapid combustion phase (from 50 to 90% of burnt fuel).
OBRÁZEK 15: Porovnání dat pro jednotlivé cykly mezi simulací (červená barva) a experimentálními daty (modrá barva) pro pracovní bod s vysokou mezicyklovou variabilitou pro motor varianty A (více v tabulkách 1 a 2) – levý obrázek odpovídá korelaci mezi úvodní fází spalování (od 0 do 2% spáleného paliva) a první částí hlavní fáze spalování (od 10 do 50% spáleného paliva), zatímco pravý obrázek reprezentuje korelaci mezi úvodní fází spalování a druhou částí hlavní fáze spalování (od 50 do 90% spáleného paliva).

of pre-chamber mixtures is pushed out of pre-chamber by increased pressure in a pre-chamber – this decreases mean air excess in a cylinder as pre-chamber mixture is rich. After that, combustion progress is similar for all considered cycles, hence confirming the data from Figure 12. This analysis suggests that pre-chamber combustion system is less sensitive to CCV effects – this is a consequence of turbulent flame jet phase which seems to dampen/suppress influence of local thermodynamic CCV.
Details of combustion process in the Engine B are shown in Figure 14. Combustion in pre-chamber is similar to combustion in classical SI engine, however mixture homogeneity CCV is higher – this is mainly related to swirling motion in pre-chamber coupled with small connecting channels. This phase is relatively slow. Once the flame reaches connecting channels (between pre-chamber and cylinder), there is relatively high pressure drop (i.e., pre-chamber pressure is clearly higher than in-cylinder pressure), which leads to high flame jet velocities (reaching values up to 200 m/s). Hence, flame jet reaches outer boundaries (e.g., piston top crown) very fast – this typically takes 2 degCA. After that, a complicated turbulent flame structure is being developed as a consequence of swirling in-cylinder motion and interaction among 12 turbulent flame jets. All that leads to fast combustion – in the case shown in Figure 14, it takes cca 10 degCA to burn all the mixture in the piston bowl. The qualitatively same effects are observed even for cases of very lean mixture combustion. Hence, it confirms that turbulence is dominating the initial phase of combustion (i.e., up to the point of 30% of burnt fuel).
Comparison of selected integral data between LES prediction and measurement is shown in Figure 15. It corresponds to different combustion phase durations. As it is clear from this figure, LES simulation is capable of reasonably good prediction – this concerns both qualitative trends (the shape of data set) and quantitative data (CCV). Other important information (based on Figure 15) is that there is very weak correlation among shown parameters, hence supporting (to a certain extent) the idea presented in some literature sources that CCV is a random process. Similar diagrams can be shown for other important cycle-specific ICE parameters (e.g., internal EGR, air excess, IMEP, max. in-cylinder pressure).
Based on above mentioned and Figure 15, it is clear that it is very difficult to predict future development within a single engine cycle while using statistical approach – the reason behind that is that correlations are very weak. This leads to conclusion that previous cycle history has to have even lower influence on combustion development during the subsequent cycle. This conclusion is clearly confirmed in [18] where experimental data are analyzed.

6. CONCLUSION

The presented paper deals with identification of main sources of cycle-to-cycle variations (CCV) in SI ICE. The main approach to achieve this target is based on 3-D CFD simulations while using LES. Two different engine cases were studied – the first one corresponds to modern automotive DI SI ICE dominated by tumble in-cylinder vortex, the second one represents gas SI ICE equipped with scavenged pre-chamber while in-cylinder flow is dominated by swirl.

In-cylinder turbulence was identified as the main source of CCV – this is in-line with well-established knowledge of SI ICE operation. The detailed 3-D CFD LES simulations confirm that the turbulence, which is created mainly during intake stroke while being strongly dissipated during compression stroke, is responsible for significant local differences of important thermodynamic properties (from CCV point of view). These are magnified by deflagration flame front propagation, the nature of which is strongly dependent on local turbulence. This also confirms the fact that the history of previous cycle(s) has almost no influence on combustion process of the current cycle. Moreover, combustion progress integral data correlations are very weak, hence it is very difficult to statistically estimate future development even if certain information from current cycle is known. This may support (to a certain extent) the idea presented in some literature sources that CCV is a random process – sometimes the following term is used to describe complex in-cylinder phenomena: 'organized chaos'.

Other important CCV source is the very beginning of combustion process – the early flame kernel development phase. This is difficult to predict in CFD without special detailed complex sub-models taking into account electro-magnetic phenomena and chemical ones as well. The prove of its importance was achieved indirectly – sensitivity studies were carried out to show that certain CCV level (of early flame kernel development process) has to be imposed to achieve experimentally observed CCV of pressure traces. These conclusions are also confirmed by the work presented in [18]. This CCV source is less important than turbulence, however its non-linear interaction with local turbulence leads to strong CCV effects.

Two different ignition systems were compared: the classical spark ignition one and turbulent flame jet one. Analysis of the data suggests that the latter one is less prone to magnify any CCV caused by ignition event. The main reason behind that statement is the fact that turbulent flame jet, which ignites the mixture in main cylinder of ICE, is primarily dependent on pressure difference (between pre-chamber and cylinder). Hence any local differences due to turbulence in pre-chamber have less influence on flame development in the main cylinder. Additional observation is that the flame structure of pre-chamber SI ICE is very different to a classic spherical flame front of a typical SI ICE – its topology is similar to diesel combustion in CI ICE. Moreover, the combustion is very fast in a main cylinder even when very lean mixture is used.

The 3-D CFD approach based on LES has proved to be an efficient and reliable tool when dealing with CCV effects – this was shown within EU FP7 project LESSCCV and it was confirmed by work presented in this paper as well. It can predict qualitative trends correctly while quality of quantitative predictions is usually fine.

ACKNOWLEDGEMENTS

This research has been realized using the support of Technological Agency, Czech Republic, program Centres of Competence, project TE01020020: 'Josef Božek Competence Centre for Automotive Industry'.

This research has been realized using the support of EU Regional Development Fund in OP R&D for Innovations (OP VaVpI) and The Ministry of Education, Youth and Sports, Czech Republic, project CZ.1.05/2.1.00/03.0125: 'Acquisition of Technology for Vehicle Center of Sustainable Mobility'.

This research has been realized using the support of The Ministry of Education, Youth and Sports program NPU I (LO), project LO1311: 'Development of Vehicle Centre of Sustainable Mobility'.

All the help has been gratefully appreciated.

LIST OF NOTATIONS AND ABBREVIATIONS

BTD	Bottom Dead Centre
CCV	Cycle-to-Cycle Variation(s)
CFD	Computational Fluid Dynamics
CI	Compression Ignition
COV	Coefficient of Variation
DI	Direct Injection
ECFM-3Z	Extended Coherent Flamelet Model – 3-zone version
EGR	Exhaust Gas Recirculation
FSD	Flame Surface Density
IMEP	Indicated Mean Effective Pressure
ICE	Internal Combustion Engine
IVC	Intake Valve Closing
KE	Kinetic Energy
LES	Large Eddy Simulation
PDF	Probability Density Function
PFI	Port Fuel Injection
RANS	Reynolds Averaged Navier-Stokes (equation set)
RFKE	Resolved Fluctuation Kinetic Energy
ROHR	Rate of Heat Release
SI	Spark Ignition
SW	Software
TKE	Turbulence Kinetic Energy
TDC	Top Dead Centre

REFERENCES

[1] Moureau, V., Barton, I., Angelberger, C., Poinsot, T., 2004. Towards Large Eddy Simulation in Internal-Combustion Engines: Simulation of a Compressed Tumble Flow, SAE Technical Paper 2004-01-1995, 2004, doi: 10.4271/2004-01-1995.

[2] Vermorel, O., Richard, S., Colin, O., Angelberger, C., Benkenida, A., Veynante, D., 2007. Multi-Cycle LES Simulations of Flow and Combustion in a PFI SI 4-Valve Production Engine, SAE Technical Paper 2007-01-0151, 2011, doi: 10.4271/2007-01-0151.

[3] Pera, C., Angelberger, C., 2011. Large Eddy Simulation of a Motored Single-Cylinder Engine Using System Simulation to Define Boundary Conditions: Methodology and Validation, SAE Int. J. Engines 4(1):948-963, doi: 10.4271/2011-01-0834.

[4] Thobois, L., Rymer, G., Soulères, T., Poinsot, T., 2004. Large-Eddy Simulation in IC Engine Geometries, SAE Technical Paper 2004-01-1854, 2004, doi:10.4271/2004-01-1854.

[5] Vitek, O., Macek, J., Tatschl, R., Pavlovic, Z. et al., 2012. LES Simulation of Direct Injection SI-Engine In-Cylinder Flow, SAE Technical Paper 2012-01-0138, https://doi.org/10.4271/2012-01-0138.

[6] Tatschl, R., Bogensperger, M., Pavlovic, Z., Priesching, P. et al., 2013. LES Simulation of Flame Propagation in a Direct-Injection SI-Engine to Identify the Causes of Cycle-to-Cycle Combustion Variations, SAE Technical Paper 2013-01-1084, https://doi.org/10.4271/2013-01-1084.

[7] Vítek, O., Macek, J., Pavlovic, Z., et al., 2016. Statistical Analysis of Detailed 3-D CFD LES Simulations with Regard to CCV Modeling, Journal of Middle European Construction and Design of Cars, 14(1), pp. 1-16. doi:10.1515/mecdc-2016-0001

[8] R. Issa, 1991. Solution of the Implicitly Discretized Fluid Flow Equations by Operator-splitting, In Journal of Computational Physics, Volume 62, Issue 1, 1986, Pages 40-65, ISSN 0021-9991, https://doi.org/10.1016/0021-9991(86)90099-9.

[9] Lesieur, M., Métais, O., Comte, P., 2005. Large-Eddy Simulations of Turbulence, Cambridge: Cambridge University Press, 2005. doi:10.1017/CBO9780511755507.

[10] Smagorinsky, J., 1963. General Circulation Experiments with the Primitive Equations, Mon. Weather Rev., Vol. 91(3): 99-164

[11] Hiromichi Kobayashi, 2005. The Subgrid-scale Models Based on Coherent Structures for Rotating Homogeneous Turbulence and Turbulent Channel Flow, Physics of Fluids, 17, 045104.

[12] Hiromichi Kobayashi, Hama, F. and Wu, X., 2008. Application of a Local SGS Model Based on Coherent Structures to Complex Geometries, International Journal of Heat and Fluid Flow 29 640-653.

[13] Richard S., Colin O., Vermorel O., Benkenida A., Angelberger C. and Veynante D., 2007. Towards Large Eddy Simulation of Combustion in Spark Ignition Engines, Proceedings of the Combustion Institute, Vol. 31, No. 1, pp. 3059-3066.

[14] Zeldovich, Y. B., Sadovnikov, P. Y. and Frank-Kamenetskii, D. A., 1947. Oxidation of Nitrogen in Combustion, Translation by M. Shelef, Academy of Sciences of USSR, Institute of Chemical Physics, Moscow-Leningrad.

[15] Dukowicz, J.K., 1980. Particle-Fluid Numerical Model for Liquid Sprays, J. Comp. Physics, 35, 229-253.

[16] Vávra, J., Syrovátka, Z., Takáts, M., Barrientos, E., 2016. Scavenged Pre-chamber on a Gas Engine for Light Duty Truck, ASME 2016 Internal Combustion Engine Fall Technical Conference, ICEF 2016, doi: 10.1115/ICEF20169423.

[17] Syrovatka, Z., Takats, M., and Vavra, J., 2007. Analysis of Scavenged Pre-Chamber for Light Duty Truck Gas Engine, SAE Technical Paper 2017-24-0095, 2017, doi:10.4271/2017-24-0095.

[18] Vítek, O., Macek, J., Poetsch, C., Tatschl, R., 2013. Modeling Cycle-to-Cycle Variations in 0-D/1-D Simulation by Means of Combustion Model Parameter Perturbations based on Statistics of Cycle-Resolved Data, SAE Int. J. Engines, 6(2), doi: 10.4271/2013-01-1314.

[19] Heywood, J. B., 1988. Internal Combustion Engine Fundamentals, McGraw-Hill series in mechanical engineering, printed in USA. McGraw-Hill. ISBN 0-07-028637-X.

[20] Peters, N., 2000. Turbulent Combustion, The Press Syndicate of the University of Cambridge, The Pitt Building, Trumpington Street, Cambridge. ISBN 0-521-66082-3.

[21] Vítek, O., Mareš, B., Macek, J., 2014. Application of LES Turbulence Model to Motored 4-Stroke Internal Combustion Engine, Colloquium Fluid Dynamics 2010, October 2013.

[22] AVL AST (2014). FIRE Manual v2014, AVL List GmbH, Graz.

[23] BOOST 2011SP1 [DVD]. AVL List GmbH, 2011.

[24] GT-Power User's Manual, GT-Suite version 7.3. Gamma Technologies Inc., 2012.

DE GRUYTER OPEN

10.1515/mecdc-2018-0004

PHYSICAL 1D MODEL OF A HIGH-PRESSURE RATIO CENTRIFUGAL COMPRESSOR FOR TURBOCHARGERS

JAN MACEK
Czech Technical University in Prague, Center of Vehicles for Sustainable Mobility, Technická 4, 166 07 Praha 6, Czech Republic
Email: jan.macek@fs.cvut.cz

ABSTRACT

The physical model of a centrifugal compressor aims at finding detailed information on values inside the machine, based on standard compressor map knowledge and basic geometry of a compressor. The model describes aerodynamics of flow from compressor inlet to outlet at a central streamline, if mass flow rate and impeller speed is known. The solution of basic conservation laws can yield unknown, cross-section averaged temperatures, pressures and velocities along central streamline for compressible fluid and treats transonic operation, as well. After the description of general methods for solving compressible fluid flow and transformation of radial blade cascades to axial ones, the system of equations is completed with empiric knowledge of compressor blade cascades – forces and losses. Howell theory is used for axial inducer and after conform transformation to radial blade diffuser cascade, as well. Radial vanes of a rotor are transformed fixing the same length of a blade and flow areas and flow separation at inducer outlet is taken into account. Specific procedure is developed for a vaneless diffuser with friction losses. Non-linear equations of gas dynamics have to be solved in numerical and iterative way with help of Newton-Raphson solver. The model treats transonic flow features in both compressor inducer and diffuser. The validation of the model will be published in the second paper focused to this topic.

The model can be used for quasi-steady simulation in a 1D model, especially if compressor map extrapolation is required. The model predictions create virtual sensors for identification of directly unmeasurable quantities inside a compressor. It helps in better understanding in-compressor processes. Moreover, the model offers parameters for unsteady model, based on 1D modules for unsteady flow modelling.

KEYWORDS: CENTRIFUGAL COMPRESSOR, 1D SIMULATION, PHYSICAL MODEL OF COMPRESSOR MAP, TRANSONIC PERFORMANCE, RADIAL DIFFUSER

SHRNUTÍ

Fyzikální model odstředivého kompresoru je zaměřen na odhad stavů proudu uvnitř kompresoru na základě změřené charakteristiky a základních geometrických rozměrů stroje. Model popisuje aerodynamiku proudu na střední proudnici od vstupu do záběrníku po výstup ze spirály pro známý hmotnostní průtok a otáčky rotoru. Řešení základních zákonů zachování určuje neznámé střední teploty, tlaky a rychlosti podél střední proudnice pro stlačitelnou tekutinu a bere v úvahu i transsonické stavy proudu. V článku jsou popsány použité iterační metody řešení proudění stlačitelné tekutiny v radiálních mřížích s využitím jejich konformního zobrazení na axiální mříž. Soustava základních rovnic pak může být doplněna o empirické poznatky o silách a ztrátách v axiálních mřížích, zejména pomocí Howellovy teorie pro záběrník rotoru a po konformní transformaci i pro radiální mříž difusoru. Radiální lopatky oběžného kola jsou transformovány na ekvivalentní difusor se stejnou délkou a poměrem průřezů, i s ohledem na separační bublinu na výstupu ze záběrníku. Nová metoda je vyvinuta pro modelování bezlopatkového difusoru s třecími ztrátami. Nelineární soustava rovnic dynamiky plynů je řešena iteracemi s použitím Newton-Raphsonovy metody. Model bere v úvahu transsonické poměry na vstupu do záběrníku a do bezlopatkového difusoru. Validace modelu bude předmětem dalšího článku.

Model lze použít pro kvazi-stacionární simulace kompresoru v 1D modelech motoru, zejména při nutnosti extrapolovat charakteristiku kompresoru. Model vytváří virtuální senzory pro odhad stavů uvnitř kompresoru, které nejsou přímo měřitelné. Pomáhá v pochopení vlivu dějů v kompresoru na jeho vlastnosti. Model nabízí do budoucna i rozšíření při použití modulů s nestacionárním jednorozměrným průtokem pro modelování jednotlivých částí kompresoru.

KLÍČOVÁ SLOVA: ODSTŘEDIVÝ KOMPRESOR, 1D SIMULACE, FYZIKÁLNÍ MODEL CHARAKTERISTIKY KOMPRESORU, TRANSSONICKÝ REŽIM, RADIÁLNÍ DIFUZOR

1. INTRODUCTION AND MOTIVATION

The high-pressure ratios of turbocharger compressors, needed for the current brake mean effective pressure levels, call for the better description and understanding of processes inside centrifugal compressors. Even using 1D approach only, suitable for repeated optimization simulations, the model can yield interesting results, if it is based on physical description of processes.

The paper aims at the 1D, quasi-steady, central streamline model of a centrifugal compressor with axial-radial flow, suitable for 1D engine models with unsteady conditions during the both transient load and speed of a car engine – general requirements being described already in [12] and [13]. The developed model of a centrifugal compressor describes the aerodynamics of flow from compressor inlet if mass flow rate and impeller speed is known. The basic idea of solution of basic conservation laws has been successfully tested for the case of centripetal radial-axial turbine – [1] and [2]. There are already such models, e.g., [15] or [16]. The current model tries to treat better transonic phenomena and use the available knowledge from axial compressor cascades taking the real asymmetric incidence angle influence into account, better than old NACA shock loss theory [4] for today's shapes of inlet blade profile.

The main goal is a development of the compressor physical model for compressible fluid flow at the reasonable level of simplification for compressor performance description. The developed model will be validated by fitting to known compressor maps aiming at extrapolation of maps and better prediction of surge and choke lines.

The model validation testing will be done against measured maps. Finding fitting (correction) coefficients by optimization methods is realized in a similar way, as it was done for the case of radial centripetal turbine, e.g. [1].

The solution of basic conservation laws can yield unknown temperatures, pressures and velocities along central streamline for compressible fluid and treats transonic operation, as well. After the description of general methods for solving compressible fluid flow and transformation of radial blade cascades to axial ones as done partially in [3], the system of equations is completed with empiric knowledge of compressor blade cascades losses. Howell theory – [4] and [5], originally published in [7] and [8] is used for axial inducer and after transformation fixing the same length of a blade and flow areas to radial blade cascades, as well.

Non-linear equations of gas dynamics have to be solved in numerical and iterative way with help of Newton solver. The treatment of transonic flow features in both compressor inducer and diffuser is described then, based on gas dynamics as described in [14]. The general compressor parameters are finally evaluated from detailed cascade description, making advantage from the modular design of the model.

The model yields information, which could be received from virtual sensors of values inside a compressor. It is suitable for the assessment of collaboration between stages in multi-stage machines and two-stage turbocharging. In the future, the model will be used for the elucidation of compressor design issues and the proposal of ways improving compressor design.

The validation of the model will be published in the second paper focused to this topic.

Moreover, the model offers parameters for unsteady model, based on 1D modules for unsteady flow modelling, as done in [1], [2] or [16].

The paper is structured in the following manner: first, geometry of blades and flow are described, taking the later use of profile cascade theory for lift and drag forces into account. Relations for combination of mass and energy conservation laws are solved for finding procedures to determine total, stagnation and static states for compressible fluid dynamics then. Loss definitions for diffuser and nozzle flows are treated after it in the form of numerical procedures. Generalized results of axial profile blade theory are applied for compressor simulations after it. Specific attention is devoted to a vaneless diffuser with compressible fluid flow. Transonic performance of inducer inlet and vaneless diffuser is analyzed then. Finally, the basic compressor component description and their interaction is described.

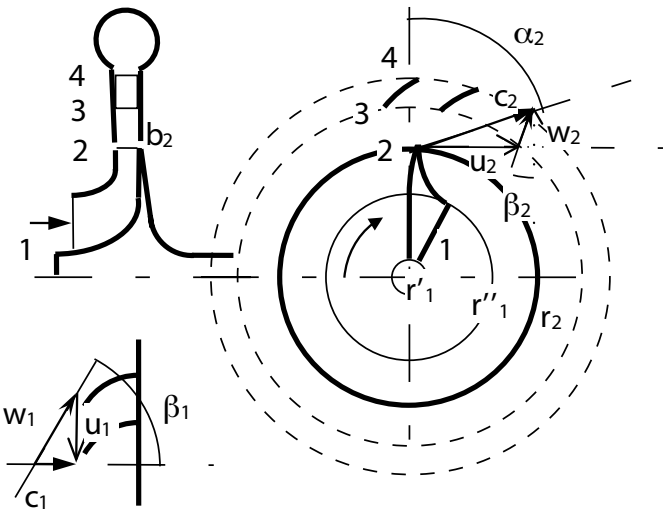

FIGURE 1: A compressor impeller (1-2) and diffuser (2-3 vaneless, 3-4 bladed) with positive sense of flow and blade angles (in reality, outlet from impeller features negative vane angle).

OBRÁZEK 1: Oběžné kolo kompresoru (1-2) a difusor (2-3 bezlopatkový, 3-4 lopatkový) s kladným směrem rychlostí a úhlů lopatek. U skutečných kompresorů je úhel výstupní části lopatek oběžného kola záporný.

2. GEOMETRY OF RADIAL COMPRESSOR FLOW

The compressor performance will be described at fixed mass flow rate and impeller speed with known geometry – at any location defined by the radius r, axial width b, step of blades in cascade s, blade chord c and blade angle measured from radius α_B or β_B for a stator or impeller, respectively. The positive direction of angle is measured in sense of impeller rotation. General scheme of radially-axial centrifugal compressor is plotted in Figure 1.

Defining flow angles by α or β for a stator or impeller, respectively, the velocity triangles and splitting vectors into tangential or axial/radial components yield, e.g.,

$$w_2 \cos\beta_2 = w_{2r} = c_{2r} = c_2 \cos\alpha_2$$
$$\vec{c}_{2t} = u_2 + \vec{w}_{2t} = u_2 + w_{2r} \tan\vec{\beta}_2 \qquad (1)$$

Symbols with arrows respect by their signs the real direction (positive in the direction of rotation), without signs are always positive (absolute values of vectors).

A radial blade cascade may be converted into the axial one using conform (angle conserving) transformation from radial-tangential cylindrical coordinates into Cartesian axial-tangential coordinates, used usually for profile cascade.

The transformation assumes constant density (or density compensated by the appropriate change of axial width b) and angular momentum conservation in a free vortex flow. Then, the both radial and axial components of velocity in polar coordinates are variable, but the product of velocity component and radius is conserved. The transformation is based on the same radial and axial area and rescaling of $d\varphi$ and $d(br)$ by the same constant factor. If channel width b is constant, then the angles of flow are conserved (conform transformation) and, especially, the velocity angle from radial direction is constant.

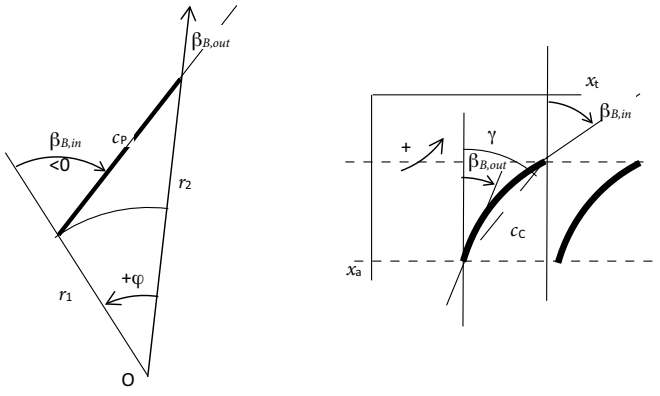

FIGURE 2: Conform transformation of general straight line from polar coordinates.
OBRÁZEK 2: Konformní zobrazení obecně položené přímky z polárních souřadnic.

$$d\phi = \frac{b_{ref} K_2}{br} dx_t \; ; \quad \frac{d(br)}{br} = \frac{b_{ref} K_2}{br} dx_a \qquad (2)$$

$$k_2\left(x_{a,out} - x_{a,in}\right) = k_2 c \cos\gamma = \ln\left(\frac{(br)_{out}}{(br)_{in}}\right)$$
$$\Delta\phi = k_2\left(x_{t,out} - x_{t,in}\right); \quad k_2 = \frac{2\pi}{zs}; \quad z = \frac{2\pi\cos\gamma}{\frac{s}{c}\ln\left(\frac{(br)_{out}}{(br)_{in}}\right)} \qquad (3)$$

For basic directions in axial or tangential straight line in Cartesian coordinates transformation yields for constant blade height radial straight line or the arc of a circle, respectively. General straight lines are transformed into logarithmic spirals. Points of blade surface can be transformed using

$$x_t - x_{t,in} = \frac{c\cos\gamma\left(\phi - \phi_{in}\right)}{\ln\left(\frac{(br)_{out}}{(br)_{in}}\right)}; \quad x_a - x_{a,in} = c\cos\gamma\frac{\ln\frac{r}{r_{in}}}{\ln\left(\frac{(br)_{out}}{(br)_{in}}\right)} \qquad (4)$$

The variability of blade height can be taken into account by this transformation, but the angles of flow are not the same as in Cartesian coordinates more. The influence of centrifugal force from flow curvature and its influence on boundary layer (BL) development cannot be taken fully into account, of course. The same is valid for impeller centrifugal force, if applicable. Although the transformation has to be corrected by calibration coefficients, the qualitative validity of this approach was several times proven for radial turbines, as in [3].

In the case of compressor impeller, the angles from radial direction are small, sometimes even zero (radial vanes), but mostly backswept (Figure 3). Even in the case of radial vanes, the flow inside impeller channels is not equivalent to purely straight diffuser channel. Lift force from flow direction change in an axial cascade is replaced in the case of radial flow by the lift force created by Coriolis inertia force. Instead of centrifugal force due to channel curvature in an axial cascade, Coriolis force acts on the flow, if radial velocity component exists.

Coriolis force causes pressure distribution in tangential direction with increase of pressure in counter-rotation direction (counter-clockwise in Figure 3). This pressure distribution is followed by the flow separation at the suction side of a vane being ahead in the sense of rotation. It is reflected by the outlet velocity profile, called "jet and wake" with flow separation bubble behind the leading vane and with jet part of flow close to the pressure side of the following vane.

The equivalence of the centrifugal force in a curved axial channel and Coriolis force in an impeller channel can be used for the estimate of deviation angle and losses in an impeller. Only one

half of Coriolis acceleration has to be used since the flow features (almost) zero angular speed due to the slip of flow relative to vanes. Using the same flow-bearing velocities for both equivalent cascades in radial (subscript r) and axial direction (a), respectively, the force acting on the element of flow with the mass of Δm is

$$w_r = \frac{\dot{m}}{\left(2\pi r_r - z b_{B,r}\right) b_r \rho} = w_a = \frac{\dot{m}}{\pi\left(r_a''^2 - r_a'^2\right)\rho} = w\cos\beta_{B,a}$$

$$F_{Co} = \Delta m \omega w_r \equiv F_{cent} = \Delta m \frac{w^2}{R} \Rightarrow \frac{\omega}{w_r} = \frac{1}{\cos^2\beta_{B,a}} \frac{y''}{\sqrt{\left(1+y'^2\right)^3}} \quad (5)$$

where y is a axial blade centerline shape, described by function of axial coordinate and derived for finding local curvature. Then, the differential equation for transformed axial blade cascade centerline can be found from its curvature using obvious

$$\frac{1}{\cos^2\beta_{B,a}} = \tan^2\beta_{B,a} + 1 = y'^2 + 1$$
$$y'' = \frac{\omega}{w_r}\sqrt{1+y'^2} \quad (6)$$

which can be integrated for $tan\ \beta_{B,a}$ using Euler's substitution.
The described transformations can help to some extent for the estimation of losses, based on old but yet worthwhile generalizations of axial diffuser blade cascades – e.g., Howell [7], [8] and [5]. Unlike estimation of incidence loss by old shock loss theory, it takes the real behavior of BL into account better. The boundary layer development in an impeller is influenced by relative vortex, moreover (see equation (33)), that is why correction by calibration coefficient is necessary.

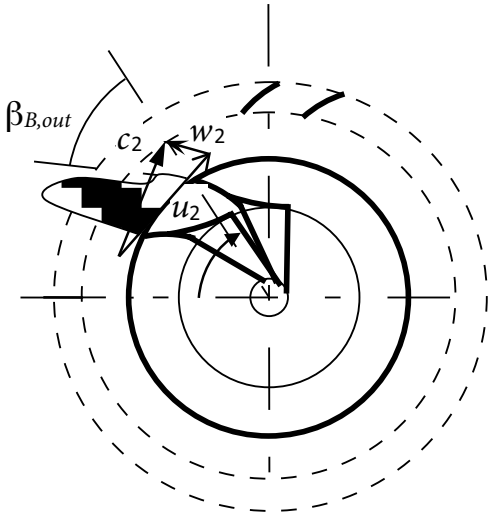

FIGURE 3: Backswept impeller vans and impeller outlet velocity profile (jet and wake).
OBRÁZEK 3: Oběžné kolo s dozadu zahnutými lopatkami. Rychlostní pole na výstupu z kanálu dle teorie proudu na přetlakové straně lopatky a úplavu na podtlakové straně.

3. TOTAL, STAGNATION AND STATIC STATES

Stodola equation for energy conservation yields, using velocities c in steady (absolute) coordinate system or w in relative (rotating) coordinate system with relative or absolute stagnation (0) states and total state (t):

$$dh + d\frac{c^2}{2} = dh_0 = 0$$
$$dh + d\frac{w^2}{2} - d\frac{u^2}{2} = dh_{0,rel} - d\frac{u^2}{2} = dh_t = 0 \quad (7)$$

E.g., for a rotating impeller it yields after integration

$$c_p T_{0,rel,out} = c_p T_{out} + \frac{w_{out}^2}{2} = c_p T_{0,rel,in} + \frac{u_{out}^2 - u_{in}^2}{2} \quad (8)$$

Non-linear equations of gas dynamics have to be solved in numerical and iterative way with help of Newton solver, as follows. If static state and mass flow rate are known, finding total state is without any numerical problem. The velocity of flow can be found from static density for reversed relation. Total temperature is

$$T_t = T + \frac{w^2}{2c_p} - \frac{u^2}{2c_p} \quad (9)$$

Total or stagnation pressure is defined by isentropic change. In the case of stagnation pressure, it yields

$$p_0 = p\left(\frac{T_0}{T}\right)^{\frac{\kappa}{\kappa-1}} \quad (10)$$

The most complicated case often occurs in a compressor description. The system of equations (9) and (10) can be replaced together with mass flow rate equation by

$$T_0 = T + \frac{1}{2c_p}\left(\frac{\dot{m}}{A\rho_0}\right)^2 \left(\frac{T_0}{T}\right)^{\frac{2}{\kappa-1}} \quad (11)$$

and solved using Newton's method for unknown static temperature

$$y = T_0 - T - \frac{1}{2c_p}\left(\frac{\dot{m}}{A\rho_0}\right)^2 \left(\frac{T_0}{T}\right)^{\frac{2}{\kappa-1}} \approx y_i + \left(\frac{dy}{dT}\right)_i \left(T_{i+1} - T\right) should\ be\ 0$$

$$\frac{dy}{dT} = -1 + \frac{1}{c_p(\kappa-1)}\left(\frac{\dot{m}}{A\rho_0}\right)^2 T_0^{\frac{2}{\kappa-1}} T^{-\frac{\kappa+1}{\kappa-1}} = -1 + \frac{1}{\kappa r}\left(\frac{\dot{m}}{A\rho_0}\right)^2 T_0^{\frac{2}{\kappa-1}} T^{-\frac{\kappa+1}{\kappa-1}}$$

$$0 = y_i + \left(\frac{dy}{dT}\right)_i \left(T_{i+1} - T_i\right) \Rightarrow T_{i+1} = T_i - \frac{y_i}{\left(\frac{dy}{dT}\right)_i} \quad (12)$$

Derivative of function in denominator must not be zero, which yields temperature limit. This temperature is just a critical temperature. If iteration result is limited to temperature greater

than this limit (and less than T_0), it yields subsonic solutions. It can be used for supersonic case, as well, if started with temperature less than limit one.

In the case of rotating channel, the similar procedure can be found. If critical state is reached, energy conservation yields between inlet and outlet

$$T^*_{out} = \frac{1}{\kappa r}\left[\kappa r T_{0in}\frac{2}{\kappa+1} + \frac{\kappa+1}{\kappa-1}\left(u^2_{out} - u^2_{in}\right)\right] \tag{13}$$

If the equation (13) is applied to calculation of static temperature from total one, the influence of centrifugal force energy is zero. The relation is valid for any adiabatic case including irreversibility. If supersonic inlet occurs, the result has to be carefully assessed from the point of view of physical stability of such solution. E.g., in the case of inducer inlet, the solution for too high mass flow rate, which would lead to further acceleration of supersonic flow in the following diffuser blade cascade, is not probably real. The inducer is choked at inlet by shock wave perpendicular to flow direction in such a case and the assumed mass flow rate cannot be reached. The maximum mass flow rate has to be calculated in advance for the static temperature from equation (13). In 3D reality, the process of choking is much more complicated and increases incidence loss via the series of oblique shocks in blade channel inlet, but the choking mass flow rate is valid, if the inlet area is corrected to possible boundary layer separation caused by λ-like shocks in boundary layer. The situation is more complicated if transonic flow velocity is caused by high speed of impeller. Further examples follow below.

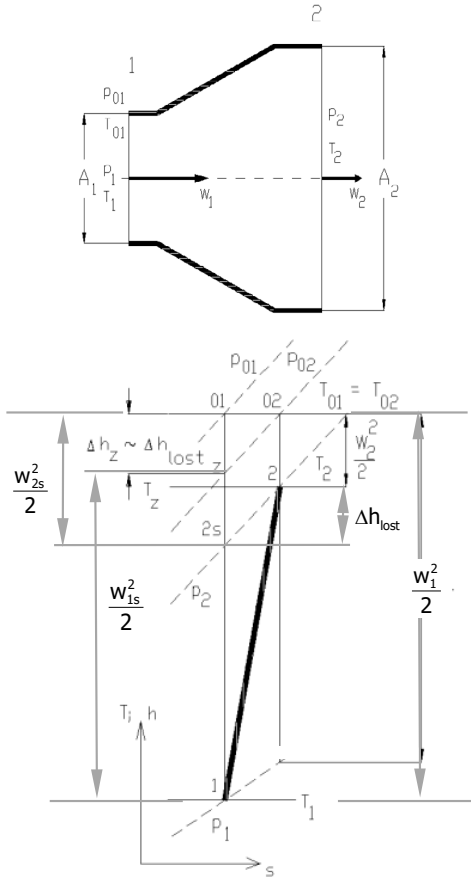

FIGURE 4: Diffuser flow and definition of losses in T-s diagram.
OBRÁZEK 4: Proudění difuzorem a definice ztrát v T-s diagramu.

4. DIFFUSER FLOW AND LOSSES

The isentropic efficiency and loss coefficient of diffuser flow is defined according to Figure 4 by the following relations

$$\eta_{in} = \frac{\frac{w^2_{1s}}{2}}{\frac{w^2_1}{2}} = 1 - \frac{\Delta h_z}{\frac{w^2_1}{2}} = 1 - \zeta_{in} \tag{14}$$

Should resulting temperature or density be determined, the procedure described above has to be changed, taking losses of kinetic energy and potential energy centrifugal force field into account. Then, it yields for compressor flow through a generally rotating diffuser cascade with known state at blade inlet *in* the static state at outlet *out* the basic relation for Newtonian iteration, similar to

$$y = T_{0in} - \frac{u^2_{in} - u^2_{out}}{2c_p} - T_{out} - \\ -\frac{1}{2c_p}\left(\frac{\dot{m}}{A\rho_{0in}}\right)^2\left(\frac{\frac{T_{out}}{T_{0in}}}{\left[\frac{T_{out}}{T_{0in}} - \zeta_{in}\left(1 - \frac{T_{in}}{T_{0in}}\right)\right]^{\frac{\kappa}{\kappa-1}}}\right)^2 \tag{15}$$

The derivative of y can be easily found in analytical way and applied to (12). The temperature has to be greater than critical one according to (13) for subsonic solution.

5. GENERALIZATION OF AXIAL BLADE CASCADE RESULTS

5.1 GEOMETRY OF AXIAL PROFILE CASCADE

The angles of flow are measured from axial direction. The blade angles are β_B, the angles of flow in coordinate system of blade cascade (relative flow coordinates) are β, the angles of flow in steady (absolute) coordinate system are α. The following relations are used for flow turn angle, incidence angle and outlet deviation angle

$$|\varepsilon| = |\beta_{in}| - |\beta_{out}|$$
$$|\iota| = |\beta_{in}| - |\beta_{B,in}| \quad (16)$$
$$|\delta| = |\beta_{B,out}| - |\beta_{out}|$$

Moreover, the airfoils are described by length of chord c, cascade step s, maximum distance of airfoil centerline from chord p angles of tangent to centerline measured from axial direction β_B.

5.2 HOWELL THEORY OF COMPRESSOR BLADE CASCADES

The losses have to be added from profile loss of planar airfoil cascade (surface friction and wake losses), secondary losses caused by induced vortices and blade tip losses.

Profile loss coefficient is calculated from drag coefficient at central streamline, using mean diameter of axial blades (if relevant) and blade step

$$R_{mean} = \sqrt{\frac{R''^2 + R'^2}{2}}; \quad s = \frac{2\pi R_{mean}}{z} \quad (17)$$

Profile cascade features can be found using Howell's approach generalizing angle of flow turn and drag coefficient for profile cascades.

The normalized angle of flow turn $\varepsilon / \varepsilon^*$ can be found from the empirical dependence of normalized angle of incidence $(\iota - \iota^*)/\varepsilon^*$ in Figure 5. Drag coefficient c_x depends on normalized step of cascade. All curves can be substituted by polynomial regressions. In the case of flow turn angle, it is amended additionally by exponential correction to separation of boundary layer

$$\frac{\varepsilon}{\varepsilon^*} = \left(a_0 + \sum_1^6 a_i \left(\frac{\iota - \iota^*}{\varepsilon^*} \right)^i + a_{13} \left(\frac{\iota - \iota^*}{\varepsilon^*} \right)^{13} \right) \left(1 - e^{\left(\frac{\frac{\iota - \iota^*}{\varepsilon^*} - 0.95}{0.4} \right)^7} \right) \quad (18)$$

Reference values can be found from reference deviation angle (Constant's rule, NACA – [4])

$$|\beta_{out}^*| = |\beta_{B,out}| + \delta^*; \quad \delta^* = \frac{0.23\left(\frac{2p}{c}\right)^2 + \frac{|\beta_{B,out}|}{500}}{\frac{1}{|\theta|\sqrt{\frac{s}{c}}} - \frac{1}{500}}; \quad (19)$$

$$|\theta| = |\beta_{B,in}| - |\beta_{B,out}|$$

and Howell's relation

$$\tan|\beta_{in}^*| - \tan|\beta_{out}^*| = \frac{1.55}{1 + 1.5\frac{s}{c}} = S \quad (20)$$

Angles are bound by the following relations

$$\varepsilon^* = |\beta_{in}^*| - |\beta_{out}^*|; \quad |\iota^*| = \varepsilon^* - |\theta| + \delta^* \quad (21)$$

which yields for reference flow turn angle a quadratic equation from (20) and (21) with the solution

$$|\varepsilon^*| = \arctan \frac{-\frac{1}{(\cos\beta_{out}^*)^2} + S\tan|\beta_{out}^*| + \sqrt{\left(\frac{1}{(\cos\beta_{out}^*)^2} - S\tan|\beta_{out}^*|\right)^2 + 8S\tan|\beta_{out}^*|}}{4\tan|\beta_{out}^*|} \quad (22)$$

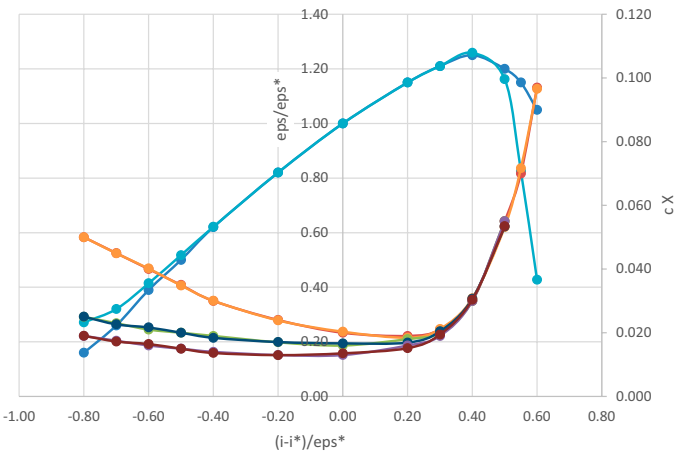

FIGURE 5: Relative angle of flow turn *eps* normalized by reference angle *eps** and profile drag coefficient *c X* for compressor blade cascade – [7]. Drag coefficient for different relative steps s/c 0.5, 1. and 1.5, as mentioned in curve descriptions. Dependences on the difference of angle of incidence ι and its reference value ι^* normalized by reference flow turn angle *eps**. Comparison of published data and regression model.

OBRÁZEK 5: Poměrný úhel natočení proudu *eps* normovaný jmenovitým úhlem *eps** a profilový součinitel odporu *c X* pro kompresorovou profilovou mříž – [7]. Součinitel odporu pro různé poměrné rozteče s/c 0.5, 1. a 1.5. Závislosti na poměrné odchylce úhlu náběhu ι od jmenovitého úhlu ι^*. Srovnání publikovaných dat a regresního modelu.

Reference values are calculated once for the whole compressor map prediction. Radial cascades in a vaned diffuser are transformed to axial ones using (4).
Then using (18)

$$\vec{\iota} = |\beta_{in}| - |\beta_{B,in}|; \quad |\varepsilon| = \varepsilon^* \left(\frac{\varepsilon}{\varepsilon^*} \right) = f\left(\varepsilon^*, \iota^*, \iota\right); \tag{23}$$

$$\vec{\beta}_{out} = |\beta_{in}| - |\varepsilon|$$

and drag coefficient can be found. Incidence angle influence is described in a better way than by NACA shock loss theory referred to in [15].

5.3 FORCES IN A BLADE CASCADE

Tangential T and axial A forces in an axial compressor blade cascade, acting from fluid to airfoils can be found from lift and drag forces using mean angle of flow – [4] – with positive directions defined in Figure 2 and for the case of compressor

$$\vec{T} = \text{sign}\left(\vec{\beta}_m\right) F_y \cos\beta_m + F_x \sin\vec{\beta}_m; |T| = F_y \cos\beta_m + F_x \sin|\beta_m|$$

$$\vec{A} = -F_y \sin|\vec{\beta}_m| + F_x \cos\beta_m; |A| = F_y \sin|\vec{\beta}_m| - F_x \cos\beta_m \tag{24}$$

using

$$\vec{\beta}_m = \arctan\left(\frac{\tan\vec{\beta}_{in} + \tan\vec{\beta}_{out}}{2} \right) \tag{25}$$

and well-known definition with lift and drag coefficients, replacing velocity in infinity by its axial component and mean angle of flow

$$F_y = c_y c \frac{\overline{\rho b}}{2} \frac{w_a^2}{\cos^2\beta_m}; \quad F_x = c_x c \frac{\overline{\rho b}}{2} \frac{w_a^2}{\cos^2\beta_m} \tag{26}$$

Drag force acts on fluid against mean velocity, lift force is perpendicular to it according to the sign of velocity circulation. If results of momentum conservation are combined with energy conservation, tangential and axial forces are determined

$$\vec{T} = \overline{\rho b}\, s w_a^2 \left(\tan\vec{\beta}_{in} - \tan\vec{\beta}_{out} \right); \quad \vec{\beta}_{out} = \vec{\beta}_{in} - \varepsilon \tag{27}$$

$$\vec{A} = -F_Y \sin|\vec{\beta}_m| + F_X \cos\beta_m = \tag{28}$$

$$= \frac{s\,\overline{b\rho}}{2} w_a^2 \left[-\frac{1-\zeta_{in}}{\cos^2\beta_{in}} + \frac{1}{\cos^2\beta_{out}} \right]$$

The procedure is prepared for Howell cascade results, in which flow angle change ε and drag coefficient c_x are generalized from experiments. Combining relations above, it yields for loss coefficient

$$\zeta_{in,p} = 1 - \tan\vec{\beta}_m \cos^2\beta_{in} \left[2\tan\vec{\beta}_{in} - 2\tan\left(\vec{\beta}_{in} - \varepsilon\right) - \right. \tag{29}$$

$$\left. - \frac{c}{s} \frac{c_X}{\cos\alpha_m} \tan\vec{\beta}_m \right] + \frac{c}{s} \frac{c_X \cos^2\beta_{in}}{\cos\beta_m} - \frac{\cos^2\beta_{in}}{\cos^2\beta_{out}}$$

and lift coefficient can be found from

$$c_y = \frac{2\cos\beta_m}{\text{sign}\vec{\beta}_m} \frac{s}{c} \left(\tan\vec{\beta}_{in} - \tan\left(\vec{\beta}_{in} - \varepsilon\right) \right) - c_X \tan|\beta_m| \tag{30}$$

6. APPLICATION OF PROFILE BLADE CASCADE THEORY TO COMPRESSOR COMPONENTS

Outlet angle from an inducer axial blade cascade can be used for estimation of local flow separation at the start of radial impeller part, using empirical chord length of separated bubble with additional calibration coefficient

$$\Delta s = K_{sep} \left(\sin|\vec{\beta}_{out}| - \sin|\vec{\beta}_{B,out}| \right) \tag{31}$$

The part of cascade step blocked by boundary layer separation is used as contraction coefficient in radial velocity component determination

$$w_r = \frac{\dot{m}}{\left[2\pi R - z\left(t_B + \Delta s\right) \right] b\rho} \tag{32}$$

Outlet angle from impeller (often backswept) vanes has to be corrected to relative vortex in intervane channel, namely subtracting tangential relative velocity component – e.g., in [4] – with correction coefficient, which respects the inter-vane channel area reduction due to vane wall thickness

$$\Delta w_t = -K_S \frac{2\pi R_{2out}}{2 z_{2out}} \cos\beta_{B2out} \omega_I = -K_S \frac{\pi u_{2out}}{z_{2out}} \cos\beta_{B2out} \tag{33}$$

Incidence angle has to be calculated according to upstream flow direction, e.g., from velocity triangles,

$$u + \vec{w}_t = \vec{c}_t; \quad w_a = c_a; \quad \tan\vec{\alpha} = \frac{\vec{c}_t}{w_a}; \quad \tan\vec{\beta} = \frac{\vec{w}_t}{w_a} \tag{34}$$

which yields, e.g., for inducer inlet or impeller outlet

$$\vec{\iota}_{1in} = \arctan\frac{\vec{c}_{1t,in} - u_1}{w_a} - \beta_{B1,in}$$

$$\alpha_{2,out} = \arctan\frac{u_2 - K_S \frac{\pi u_{2out}}{z_{2out}} \cos\beta_{B2out} + w_r \tan\vec{\beta}_{B2,out}}{w_r} \tag{35}$$

with flow rate velocities

$$w_a = \frac{\dot{m}}{K_{sep,a}\left[\pi\left(R''^2 - R'^2\right) - zt_B\left(R'' - R'\right)\right]\rho};$$
$$w_r = \frac{\dot{m}}{K_{sep,r}\left(2\pi R - z\left(t_B + \Delta s\right)\right)b\rho} \tag{36}$$

The profile drag coefficient is found from regression described together with equation (18) and recalculated to loss coefficient according to (29).

Secondary losses depend on lift coefficient square, using classic Glauert results. Secondary loss coefficient has to be added to the profile loss one – see [4], [9] and [6] – for blade length b and radial shroud clearance k including tip losses according to [9]

$$\zeta_{in,s} = \left[\frac{0.04}{\frac{b}{c}} + \frac{0.025\frac{k}{b}}{\frac{s}{c}\cos\beta_{out}}\right]\frac{c_Y^2}{\frac{s}{c}}\frac{\cos^2\beta_{in}}{\cos^3\beta_m} \tag{37}$$

If $Re_{c,w\ in}$<200 000 (it may occur at high-pressure compressor stages stages), correction to Re should be done before loss coefficients are summarized – [4]

$$\frac{\zeta_{2p} + \zeta_{2s}}{\left(\zeta_{2p} + \zeta_{2s}\right)_{Re=2.10^5}} = \left(\frac{2.10^5}{Re_{c,w_2}}\right)^{0.2} \tag{38}$$

otherwise no correction is applied. Then

$$\zeta_{in} = \zeta_{in,p} + \zeta_{in,s} + \zeta_{in,l} \tag{39}$$

All estimations have to be corrected by mentioned calibration coefficients.

6.1 IMPELLER INDUCER

The relations for flow turn angle and loss coefficient can be directly applied to quasi-axial inducer blades with correction coefficients taking into account the influence of Stodola vortex and centrifugal force stabilization of BL in radial part of blades.

6.2 BLADED DIFFUSER

Howell theory [7] or [8] can be used after transformation from polar coordinates to Cartesian ones. The procedure is described by Eqs. (4) and (18) – (24).

6.3 VANELESS DIFFUSER

The classic vaneless diffuser theory assumes free vortex (i.e., angular momentum conservation) for tangential velocity component and mass conservation with constant density for radial velocity component. If constant axial width b of vaneless diffuser (as plotted between positions 2 and 3 in Figure 1) is assumed, well-known logarithmic spiral streamline is achieved. Both assumptions are too much idealized, since recent compressors achieve transonic flow at an impeller outlet, the compressibility of fluid and friction loss at side walls of a vaneless diffuser should be taken into account. Velocity components in absolute space of inlet to a vaneless diffuser are

$$c_{2t,in} = u_2 - K_S\frac{\pi u_{2out}}{z_{2out}}\cos\beta_{B2out} + w_{2r}\tan\beta_{B2out}$$
$$c_{2r,in} = \frac{\dot{m}}{K_{sep,r}2\pi R_{2,in}b_{2,in}\rho_{2,out}} \tag{40}$$

Angular momentum conservation yields for radius greater than the inlet radius of a vaneless diffuser, if turbulent friction at side walls is assumed

$$c_t r = \left(c_t + \frac{dc_t}{dr}dr\right)\left(r + dr\right) + \frac{dM_f}{\dot{m}}$$
$$\frac{dM_f}{\dot{m}} \approx \frac{\frac{K_f}{Re_{2b,c}^{0.2}}\frac{2\pi}{2b}\frac{\bar{\rho}\left(c_{2t,in}^2 + c_{2r,in}^2\right)R_2^2}{2}}{\dot{m}}dr \tag{41}$$
$$c_t = \frac{R_2 c_{2t,in}}{r} + \frac{\frac{K_f}{Re_{2b,c}^{0.2}}\frac{\pi}{b}\frac{\bar{\rho}\left(c_{2t,in}^2 + c_{2r,in}^2\right)R_2^2}{2}}{\dot{m}}\left(\frac{R_2}{r} - 1\right)$$

A simplified assumption has been used for friction torque estimate, considering constant channel with b, angular momentum and mean constant density.

Centrifugal force, inertia force from change of radial velocity and pressure equilibrium yield in cylindrical coordinates

$$\frac{dp}{dr} = \frac{c_t^2}{r}\rho + \frac{dc_r}{dr}\frac{dr}{dt} = \rho\frac{c_t^2}{r} - \rho c_r\frac{dc_r}{dr} \tag{42}$$

Mass and energy conservations for adiabatic case conservation yield

$$\frac{dc_r}{dr} = -\frac{\dot{m}}{2\pi}\frac{b\rho + r\rho\frac{db}{dr} + br\frac{d\rho}{dr}}{\left(rb\rho\right)^2};\quad c_p\frac{dT}{dr} = -c_t\frac{dc_t}{dr} - c_r\frac{dc_r}{dr}$$
$$\frac{dc_r}{dr} = -c_r\frac{b\rho + r\rho\frac{db}{dr}}{rb\rho} - \tag{43}$$
$$-c_r\left(\frac{\rho}{p}\frac{c_t^2}{r} - \frac{\rho}{p}c_r\frac{dc_r}{dr} + \frac{1}{c_pT}\left(c_t\frac{dc_t}{dr} + c_r\frac{dc_r}{dr}\right)\right)$$

which can be solved for radial component derivative numerically, if tangential component derivative is expressed by means of

the equation (41). The vaneless diffuser has to be divided into several radial sectors for at least approximate integration of those differential equations. Narrow circular strips should be used for higher Mach numbers. If Mach number less than 0,5, the sensitivity to density change is small.

Resulting radial velocity, pressure, density and tangential velocity at the outlet radius of a vaneless diffuser can be found without major issues, if the inlet flow is subsonic.

7. TRANSONIC PERFORMANCE

The above deduced procedure can be applied for all blade cascades in a compressor if Mach number is less than approximately 0.7. It is fulfilled for impeller except for inducer inlet, especially at high speeds, as mention in comments to the equation (13).

Even before inducer inlet choking is reached, the local relative velocity Mach number, namely the blade tip Mach number, can exceed transonic limit. Combining velocity triangles, continuity equation

$$w_a = \frac{\dot{m}}{K_{sep,a}\left[\pi\left(R''^2 - R'^2\right) - zt_B\left(R'' - R'\right)\right]\rho_{1in}} = \\ = \frac{\dot{m}}{k\pi R''^2 \rho_{1in}} = w_{1in}\cos\beta_{1in} \qquad (44)$$

$$k = \frac{\left(R''^2 - R'^2\right) - zt_B\left(R'' - R'\right)}{K_{sep,a}R''^2}$$

and energy conservation with definition of stagnation state and Mach number, the following relation can be found for the blade tip Mach number

$$\dot{m} = \frac{k\pi R''^2 \kappa p_{01in} a_{01in}}{u_1''^2} \frac{M_1''^3 \sin^2\beta_{1in}\cos\beta_{1in}}{\left[1 + \frac{\kappa-1}{2}M_1''^2\cos^2\beta_{1in}\right]^{\frac{1}{\kappa-1}+\frac{3}{2}}} \qquad (45)$$

This equation can be applied for mean radius and angle of inducer flow to find the approximate limit of inducer choking, as well. According to measurements, the flow separation coefficient should be corrected. The choking limit may be set by a diffuser, as well, as described below. As a difference to inducer choking, the diffuser choking depends more on compressor speed.

In the dependence of mass flow rates for Mach number greater than 1, the loss coefficient of inducer axial blades should be reduced before critical mass flow rate for the whole blade height is reached – [5].

In the case of a vaneless diffuser, the subsonic assumption might not be the case of current high-pressure compressors. The step-by-step integration of density history from equation (43) can be simultaneously used with assessment of transonic flow issues downstream of an impeller.

Inlet flow to a vaneless diffuser is mostly supersonic in high-pressure compressors today. It is caused by the high blade speed of an impeller. The vaneless part is very important to decrease flow velocity in absolute space before the flow enters bladed diffuser, otherwise intensive shock waves with possible BL separation can occur. If shock wave occurs in the vaneless diffuser, it is an oblique shock of angle σ' measured from direction of absolute flow velocity (90° would mean a transversal shock wave). Due to rotational symmetry, the shock wave line must have circular shape and the angle measured from radial direction is $90°- \sigma'$. There are three possible cases for transonic flow then:

- Angle α of flow velocity from radial direction is greater than $90°- \sigma'$ (angle of flow deviation due to oblique shock is $\theta = 0$ in Figure 6 – [14] and [17])

$$\theta = \sigma - \arctan\left[\tan\sigma\frac{2 + (\kappa-1)M_r'^2\sin^2\sigma}{(\kappa+1)M_r'^2\sin^2\sigma}\right] \qquad (46)$$

  The normal component of velocity to the possible shock line is subsonic then and no oblique shock may occur. Integration for subsonic radial velocity can be done together with flow deceleration due to tangential component reduction according to angular momentum conservation – equations (41), (42) and (43); this case is often present in today's compressor designs.
- Angle α of flow velocity from radial direction less than $90°- \sigma'$ but greater than $90°- \sigma'$ *for maximum deviation angle* θ (Figure 6). Oblique shock with supersonic radial velocity component occurs for radial Mach number

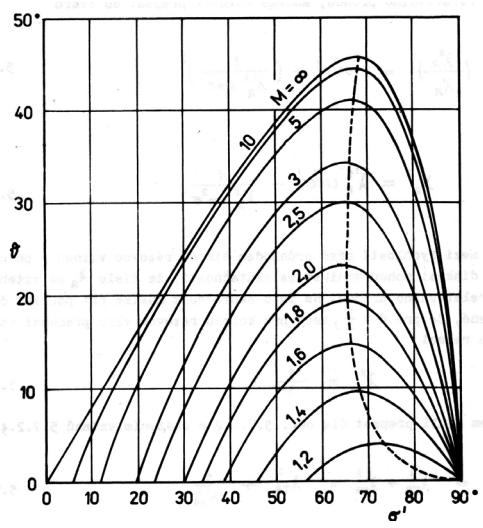

FIGURE 6: Oblique shock: flow deviation angle Θ and shock front angle σ′ measured from velocity direction in front of shock for different initial Mach numbers (from [17]).

OBRÁZEK 6: Šikmá rázová vlna: úhel odklonu proudu Θ a úhle rázové vlny σ′ měřený od směru rychlosti před rázem pro různá počáteční Machova čísla (převzato ze [17]).

$$M_r = \frac{c_r}{a} = \frac{c_r}{\sqrt{\kappa r T}} \tag{47}$$

$$c'_r c''_r = a_r^{*2} = \frac{2}{\kappa+1} a_{0r}^2 = \frac{2\kappa r}{\kappa+1}\left(T + \frac{c_r'^2}{2c_p}\right) \tag{48}$$

$$\frac{\rho''}{\rho'} = \frac{\frac{\kappa+1}{\kappa-1}}{1+\frac{1}{M_r^2}\frac{2}{\kappa-1}}; \quad \frac{p''}{p'} = \frac{2\kappa}{\kappa+1} M_r^2 - \frac{\kappa-1}{\kappa+1} \tag{49}$$

After the shock, subsonic flow equations (41), (42) and (43) can be used.

- Angle α of flow velocity from radial direction is less than *90°- σ' for maximum of θ,* which is approx. 20° (Figure 6). The branches of curves between maximum of flow deviation and lateral shock are unstable. The shock wave tends to be lateral to flow direction, which is impossible due to rotational symmetry in the case of vaneless diffuser. Mass flow rate has to be reduced to achieve the Mach number just for maximum of deviation angle. Choking at a diffuser occurs in this case, which is impeller speed dependent unlike the choking at an inducer according to equation (45) applied to the mean radius of a blade.

8. COMPRESSOR PERFORMANCE

The overall picture of processes inside a compressor is plotted in h-s diagram in Figure 7, using energy conservation for rotating channel, definition of total and stagnation states and velocity triangles.

The simulation procedure is based on known mass flow rate and speed of an impeller. Static states are determined form conservation of total states (Figure 7), mass conservation yielding velocities and loss coefficients, determining entropy increases.

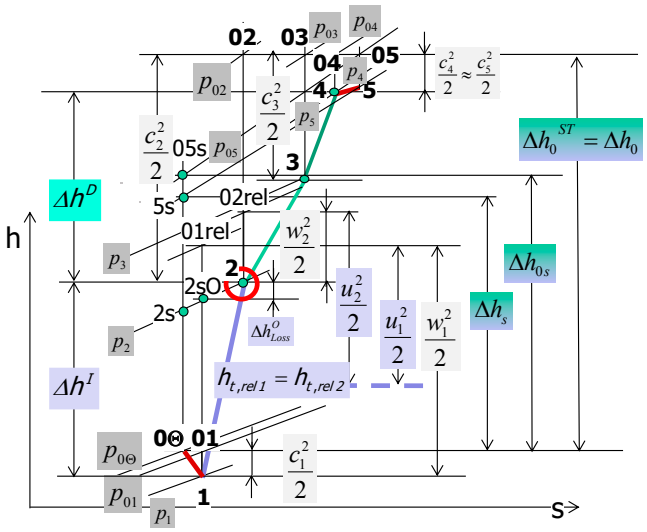

FIGURE 7: h-s diagram of a compressor.
OBRÁZEK 7: h-s diagram kompresoru.

The pressure losses in yet not described parts (an inlet casing or outlet scroll) may be estimated using empirical loss coefficient for friction loss at walls and local losses with approximately constant velocity and density

$$\Delta h_{lost} = \zeta_{out} \frac{w_{out}^2}{2} = \frac{\Delta p_{0,loss}}{\rho_{in}} \tag{50}$$

$$T_{0,in} = T_{0,out}$$

which yields input for the following part of a compressor.

Velocity triangles and decomposition of velocities into axial/radial and tangential components are described by equations similar to (34) for impeller inlet and outlet. Starting with known inlet total state, the static states are determined going from inlet by equations sets (12) and (15).

Flow angles are calculated from Howell theory according to (23) with correction to relative vortex in an impeller – equation (29). Flow area and radial velocity is corrected to local BL separation – equation (31). Loss coefficients are found according to regression similar to (18) after recalculation form drag coefficient to profile loss coefficient (29) adding all partial losses to it in (39).

If inlet and outlet velocities at an impeller are known, the power can be calculated from Eulerian theorem and checked by Stodola for the adiabatic case – see Figure 7

$$P_{C,\text{int}} = \dot{m}\left(c_{t2}u_2 - c_{t1}u_1\right) = \dot{m}c_{pl}\left(h_{02} - h_{0\Theta}\right) \tag{51}$$

Windage loss of an impeller can be estimated from windage power

$$P_{wind} = 0.000735\beta\rho_2 D_2 u_2^3 \dot{m} \tag{52}$$

for β=6 ... 8. Windage power is subtracted from the internal power. Reduced mass flow rate, reduced speed and isentropic efficiency are calculated according to standard definitions.

9. CONCLUSION – PROSPECTS AND FURTHER WORK

The presented physical model of a centrifugal compressor is suitable for compressor simulation in 1D codes if calibrated according to measured compressor maps. On one hand, it uses the basic generalization of experiments valid for axial blade cascades, although amended by certain adoption of radial cascades features, which has to be corrected by available experiments. On the other hand, it treats the transonic flow in the compressors of high-pressure ratio, which yields an opportunity to extrapolate the maps with certain reliability. It is important for choke limit especially. The extrapolation or prediction of surge limits, especially under influence of engine pulsating inlet flow, has not been tested yet. The dynamic surge limit is still certainly a big issue. The procedures for transonic flow prediction are stable and controllable from the

numerical point of view, which ensures reliable behavior during calibration done by optimization.

In any case, the further development and validation of the model is inevitable. The results will be published soon in some of the next MECCA items.

The still remaining items of the further development will cover

- compressor inlet duct loss including the optional use of pre-swirl blades
- leakages at shroud and hub sides influencing back-flow to inducer blades and windage loss at hub side of an impeller
- inducer flow inlet angle corrected to the backflow through a shroud clearance adding angular momentum to inlet flow
- internal recirculation channel (IRC) for surge limit modification
- influence of relative Stodola vortex to secondary vortices in inducer blades (amplification of asymmetry of counter-rotating secondary vortex couple)
- scroll friction and flow separation losses
- the impact of an outlet diffuser located downstream of a scroll
- heat transfer in a compressor casing.

ACKNOWLEDGMENTS

This research has been realized using the support of Technological Agency, Czech Republic, program Centre of Competence, project #TE01020020 Josef Božek Competence Centre for Automotive Industry and The Ministry of Education, Youth and Sports program NPU I (LO), project # LO1311 Development of Vehicle Centre of Sustainable Mobility. This support is gratefully acknowledged.

REFERENCES

[1] Macek, J., Zak, Z., and Vitek, O., Physical Model of a Twin-scroll Turbine with Unsteady Flow, SAE Technical Paper 2015-01-1718, 2015, doi:10.4271/2015-01-1718.

[2] Macek J., Vítek O., Burič J. and Doleček V.: Comparison of Lumped and Unsteady 1-D Models for Simulation of a Radial Turbine. SAE Int. J. Engines Vol.2(1) 173-188, 2009, ISSN 1946-396. SAE Paper 2009-01-0303

[3] Sherstjuk, A. N., Zaryankin, A.E., "Radial-axial Turbines of Small Power" (in Russian), Mashinostroenie, Moscow 1976

[4] Dixon S. L. Fluid Mechanics, Thermodynamics of Turbomachinery, Pergamon Press, Oxford 1975

[5] Kousal. M., "Stationary Gas Turbines" (in Czech), SNTL Prague 1965

[6] Vavra, M. H., Aero-Thermodynamics and Flow in Turbomachines, J. Wiley&Sons, New York 1960

[7] Howell, A. R., The Present Basis of Axial Flow Compressor design: Part 1 – Cascade Theory and Performance, ARC R&M 2095, 1942

[8] Howell, A.R., Fluid Dynamics of Axial Compressors, Proc. I. Mech. E, 153 (1945), #12, pp. 441-452

[9] Dunham, J., Came, P.: Improvements to the Ainley-Mathieson Method of Turbine Performance Prediction. Trans. ASME, Series A, Vol. 92, 1970

[10] Canova M et al., A Scalable Modelling Approach for the Simulation and Design Optimization of Automotive Turbochargers, SAE Technical Paper 2015-01-1288

[11] Vítek O, Macek J and Polášek M, New Approach to Turbocharger Optimization using 1-D Simulation Tools, SAE Paper 2006-01-0438, 2006

[12] Watson N and Janota MS (1982) Turbocharging the Internal Combustion Engine. MacMillan Publishers, London 1982, ISBN 0 333 24290 4

[13] Zinner K., Aufladung von Verbrennungsmotoren, Springer 1975

[14] Shapiro, A. H., The Dynamics and Thermodynamics of Compressible Fluid Flow, The Ronald Press Comp., New York 1953.

[15] Nakhjiri, M., Pelz, P., Matyschok, B., Däubler, L. et al., Physical Modeling of Automotive Turbocharger Compressor: Analytical Approach and Validation, SAE Technical Paper 2011-01-2214, 2011, https://doi.org/10.4271/2011-01-2214.

[16] Bozza, F., De Bellis, V., Marelli, S., and Capobianco, M., 1D Simulation and Experimental Analysis of a Turbocharger Compressor for Automotive Engines under Unsteady Flow Conditions, SAE Int. J. Engines 4(1):1365-1384, 2011, https://doi.org/10.4271/2011-01-1147.

[17] Jerie, J., "Theory of Aircraft Engines" (in Czech), CTU in Prague, 1985

SYMBOLS AND SUBSCRIPTS

A	flow area [m^2]; axial force component [N]
a	sound velocity [m.s^{-1}]; axial Cartesian coordinate; regression coefficient
b	blade length perpendicular to axial or radial direction [m]
c	chord length [m]; specific thermal capacity [J.K^{-1}.kg^{-1}]; absolute velocity [m.s^{-1}]
c_x	drag coefficient [1]
c_y	lift coefficient [1]
h	specific enthalpy [J.kg^{-1}]
K	tuning coefficient [1]
k	tuning coefficient [1; radial shroud clearance [m]
M	Mach number [1]
m	mass, mass flow rate (dotted)[kg, kg.s^{-1}]

n	speed [min^{-1}]
P	power [W]
p	pressure [Pa]; position of maximum distance between airfoil centerline and chord [m]
R	radius [m]
Re	Reynolds number [1]
r	radius [m]; specific gas constant [$J.K^{-1}.kg^{-1}$]
s	cascade step [m]
T	temperature [K]; tangential force component [N]
t	tangential Cartesian coordinate [m]; blade profile thickness [m]
u	circumferential blade speed [$m.s^{-1}$]
w	relative velocity [$m.s^{-1}$]
x	Cartesian coordinate [m]
y	iteration variable
z	number of blades [1]
α	angle of absolute velocity of flow (from radial or axial direction in the sense of speed)[deg]
β	angle of relative velocity of flow (from radial or axial direction) [deg]
β_B	angle of tangent to blade centerline
γ	angle of airfoil chord from axial or radial direction[deg]
δ	flow deviation outlet angle [deg]
ε	flow turn angle [deg]
η	isentropic efficiency [1]
ι	flow incidence angle [deg]
λ	coefficient of secondary losses [1]
φ	polar or cylindrical coordinate angle [deg]
κ	c_p/c_v ratio, isentropic exponent [1]
π	pressure ratio >1 [1]
ρ	density [$kg.m^3$]
σ	angle of oblique shock wave measured from flow velocity direction[deg]
θ	profile centerline turn angle [deg]; flow deviation angle in oblique shock
ζ	loss coefficient [1]
ω	angular velocity [$rad.s^{-1}$]

SUBSCRIPTS

a	axial
B	blade
C	compressor; Cartesian
I	impeller
m	mean
max	maximum
min	minimum
P	polar
p	at constant pressure; profile loss
r	radial
red	reduced
ref	reference
reg	regression
rel	relative state
s	isentropic; flow separation; secondary (induced) loss
sep	flow separation
T	turbine
TC	turbocharger
t	total state; tangential
v	at constant volume
X	drag
Y	lift
0	stagnation state
in	inlet
out	outlet
z	loss
$1, 2, 3..$	position in a compressor
‘	blade root (hub)
“	blade tip (shroud)
*	reference, nominal; critical state of flow
$\bar{}$	averaged
$\vec{}$	vector (if value is used, it has to feature appropriate sign acc. to axis direction)

ACRONYMS

BL	boundary layer
$bmep$	brake mean effective pressure
CR	centripetal radial
ICE	internal combustion engine
$IMEP$	indicated mean effective pressure
IRC	internal recirculation channel (anti-surge measure for centrifugal compressors)
MFR	mass flow rate
RPM	revolutions per minute
WOT	wide-open throttle curve

GUIDELINES FOR AUTHORS

A. LANGUAGE

01) Language of paper – American English
02) Abstract, captions and keywords will be bilingual English and Czech, optionally English and Slovak. Authors from the Czech and Slovak Republic should prepare abstract, keywords and captions in English and native language. The abstract and captions for other authors will be translated by the publisher to Czech language.

B. LENGTH

Title should not exceed 10 words
Subtitle should not exceed 15 words
Abstract should not exceed 200 words
Paper without limit

C. ORDER OF CONTENTS

01) Title
02) Author(s) name: per author company/institute, address, and e-mail (on new line)
03) Abstract
04) Keywords
05) Body of the paper. The paper should be divided into logical numbered sections.
06) Preferred structure:
    – Introduction: Background – Motivation – Goals
    – Used methods
    – Results
    – Analysis of results and evaluation
    – Conclusion: Result Utilization – Prospects
07) Acknowledgements
08) List of notations and abbreviations (in alphabetical order)
09) References
10) Appendices: Long derivation of equations, description and parameters of experimental equipment or methods, etc.

To facilitate the blind reviewing process, the authors are asked provide on a separate first page the items 1) and 2) and to start the main part of the article with 1) Title; and then 3) Abstract, and so on.

D. GRAPHICAL ARRANGEMENT

Title: Times New Roman 17b, Bold
Body of paper, abstract, equation numbering: Times New Roman 11b. Titles of sections Times New Roman 12b Bold. Symbols of physical quantities used in text: italic. SI units, wherever possible. Combined units should be written with dot (example: N.m, $m.s^{-2}$, …).
Authors should avoid the usage of footnotes.
Captions: Times New Roman 10b, in bold – number and caption, normal – text of legend. See examples:

Figure 1: This is a figure.
Table 1: This is a table.

All illustrations should be numbered sequentially with arabic numbers.
Equations: Times New Roman italic. Variable 12b, Index 7b, Small index 5b, Symbol 18b, Small symbol 12b. Mathematical operators and constants (Ex.: sin, e, π, …) Times New Roman 12b normal.
All equations should be numbered sequentially with arabic numbers. List of notations either under every equation, or at the end of paper – see paragraph D (according to number and content of equations). Long derivation as appendix on the end of paper.
References: References referred in text in square brackets in format of text (Ex: [1])
Format of references, examples:

[1] Author A., Author B. and Author C. (2002). This is journal article, In: Journal for Interesting Papers, Vol. 10, No. 3, p. 130–145. ISSN
[2] Author A., Author B. and Author C. (eds.). Our Book on Car Technology, MIT Press, Massachusetts, 2002, p. 23-145. ISBN
[3] Author A., Author B. and Author C. (2002). My paper in a conference, In: Editor A., Editor B. and Editor C. (eds.). Proceedings Of Our Meeting in a Far Away Exotic Place, MIT Press, Massachusetts, p. 78-89. ISBN

E. ILLUSTRATIONS

The Journal is full-color.
The authors are responsible for delivering high-quality graphic material. In the case of illustrations sent via mail, the orientation of illustrations should be indicated, as well as their number in the article. The illustrations sent electronically, should be sent in the correct orientation and in a resolution at least 300 dpi, in common graphical formats.

F. SUBMISSION OF MANUSCRIPTS

Text should be in all cases prepared in electronical form. Paper can be sent via mail (the contents of mail should be illustrations and diskette 3,5" or CD with text), or via e-mail on the address mentioned below.
Text should be sent in format MS Word 2000 or older (format doc, or rtf). Do not merge illustrations in the text to avoid excessive file size. All illustrations should be sent in separate files. No illustrations will be returned unless specifically requested.
Contact address for submission of paper:
ČVUT, FS, MECCA
Gabriela Achtenová
Technická 4, 166 07 Praha 6, Czech Republic
Tel.: +420 2 24 35 24 99, Fax: +420 2 24 35 25 00
E-mail: gabriela.achtenova@fs.cvut.cz

G. COPYRIGHT

The papers submitted to journal MECCA have not been previously published or submitted elsewhere. The copyright of accepted papers becomes the property of Czech Technical University, and usage of any part of papers without permission of Czech Technical University will be not allowed. Authors who wish to reproduce already published illustrations should asked the permission by the copyright holder. Authors are asked to sign copyright agreement.

H. PUBLICATION

All articles will be blind reviewed. The first author, if no other contact person is marked, will be informed about the decision as soon as possible.
Authors will get 3 copies of the journal in which the article is published.

MASTER OF AUTOMOTIVE ENGINEERING

ENTRANCE LEVEL: Technical bachelor (mechanical, transport, or electro engineering)

CTU
Prague
Czech republic

(E)

ITB
Bandung
Indonesia

(E), (I)

ENSTA
Brest
France

(F)

TUCH
Chemnitz
Germany

(G)

3rd SEMESTER

Entrance exam IFP

ENSTA
- Design of Vehicles
- Modelisation and Computation

(F)

HAN
Vehicle Dynamics and Intelligent Transport Systems

(E)

CTU
Advanced Powertrains

(E)

TUCH
Alternative Powertrains

(G)

IFP
Paris
France

(F)+(E)

4th SEMESTER devoted to final thesis and 5 months internship in an industrial or academic environment anywhere in the world

MASTER DEGREE IN AUTOMOTIVE ENGINEERING
Master degree from 2 countries with respect to chosen specialisation in 3rd semester

(F) – in French, (E) – in English, (I) – in Indonesian, (G) – in German

CTU
Czech Technical University in Prague
Czech Republic
Gabriela Achtenová
gabriela.achtenova@fs.cvut.cz
Tel.: +420 224 352 499

ITB
Institut Teknologi Bandung
Indonesia
Andi Isra Mahyuddin
aim@ftmd.itb.ac.id

ENSTA
ENSTA Bretagne
France
Yann Marco
yann.marco@ensta-bretagne.fr
Tel.: +33 298 348 844

TUCH
Technische Universität Chemnitz
Germany
Diana Lohse
diana.lohse@mb.tu-chemnitz.de
Tel.: +49 371 531 337 94

HAN
Hogeschool van Arnhem en Nijmegen
The Netherlands
Kea Bouwman
kea.bouwman@han.nl
Tel.: + 31 26 384 93 14

DEADLINE FOR: NON EU STUDENTS 1ST MAY 2018, EU STUDENTS 30TH JUNE 2018
For application form, detailed programme, studying conditions, tuition fees and all other informations, please see: www.emae.eu

CZECH TECHNICAL UNIVERSITY IN PRAGUE
ITB
ifp SCHOOL
ENSTA Bretagne
TECHNISCHE UNIVERSITÄT CHEMNITZ
Hogeschool van Arnhem en Nijmegen HAN University